INFORMATION TO USERS

This manuscript has been reproduced from the microfilm master. UMI films the text directly from the original or copy submitted. Thus, some thesis and dissertation copies are in typewriter face, while others may be from any type of computer printer.

The quality of this reproduction is dependent upon the quality of the copy submitted. Broken or indistinct print, colored or poor quality illustrations and photographs, print bleedthrough, substandard margins, and improper alignment can adversely affect reproduction.

In the unlikely event that the author did not send UMI a complete manuscript and there are missing pages, these will be noted. Also, if unauthorized copyright material had to be removed, a note will indicate the deletion.

Oversize materials (e.g., maps, drawings, charts) are reproduced by sectioning the original, beginning at the upper left-hand corner and continuing from left to right in equal sections with small overlaps. Each original is also photographed in one exposure and is included in reduced form at the back of the book.

Photographs included in the original manuscript have been reproduced xerographically in this copy. Higher quality 6" x 9" black and white photographic prints are available for any photographs or illustrations appearing in this copy for an additional charge. Contact UMI directly to order.

UMI

A Bell & Howell Information Company
300 North Zeeb Road, Ann Arbor MI 48106-1346 USA
313/761-4700 800/521-0600

UNIVERSITY OF OKLAHOMA

GRADUATE COLLEGE

LARGE-EDDY SIMULATION OF STRATOCUMULUS-TOPPED BOUNDARY LAYER WITH AN EXPLICIT AND A NEW BULK MICROPHYSICS SCHEME

A Dissertation

SUBMITTED TO THE GRADUATE FACULTY

In partial fulfillment of the requirements for the

degree of

Doctor of Philosophy

By

MARAT KHAIROUTDINOV

Norman, Oklahoma

1997

LARGE-EDDY SIMULATION OF STRATOCUMULUS-TOPPED BOUNDARY LAYER WITH AN EXPLICIT AND A NEW BULK MICROPHYSICS SCHEME

A Dissertation APPROVED FOR THE

SCHOOL OF METEOROLOGY

BY

Yefim Kogan

Brian Fiedler

Jon Straka

Dick Doviak

Leonid Dickey

Acknowledgments

I would like to acknowledge Dr. V. I. Khvorostyanov who was my supervisor during my last years as a student at the Moscow Institute of Physics and Technology and during my work as a Research Associate at the Central Aerological Observatory in Moscow, and whom I owe my interest in the field of numerical modeling of clouds.

I wish to offer my sincerest and heartfelt thanks to Dr. Yefim Kogan, my research advisor, for giving me this unique opportunity to pursue the doctoral degree at the University of Oklahoma, for scientific guidance, encouragement, financial support and patience through all these years. By inviting me from Russia after the dusk of the Soviet Empire, he saved me from a frightening prospective of making my living at Moscow Stock Exchange as most of my old schoolmates now do.

I am grateful to my academic advisor and my committee chair, Dr. Brian Fiedler, for fruitful scientific discussions and collaboration, and recent financial support. I would like to mention his beautiful EZM ("easy model"), whose clarity inspired me to code the first version of the LES dynamical framework.

My special thanks and appreciation go to my honorary advisor Dr. Douglas Lilly, member of my committee and former chair, for his guidance and continuous interest in the progress of my research. The afternoon coffee-breaks sponsored by him when being a Director of CAPS is among those pleasant things that I enjoyed so much during my years at OU graduate school.

I would like to acknowledge Dr. Jerry Straka for serving on my committee and for his interest in my research as well as useful discussions that led to improvement of this dissertation. I would also like to thank Prof. Leonid Dickey from the Department of Mathematics for agreeing to serve as an outside member of my committee.

My special thanks go to Prof. Peter Lamb, the CIMMS Director, for providing the opportunity to work as a Graduate Research Assistant for CIMMS, as well as to the CIMMS staff for the clerical assistance. I would like to acknowledge the School of

Meteorology for paying my tuition waiver. I thank the computer system administrator Tom Condo, whose prompt replies to my desperate e-mails are greatly appreciated.

My sincere thanks go to Dr. Chin-Hoh Moeng, for providing the LES code which served as a dynamical framework in the previous version of the CIMMS LES model and was used for testing the new version of the model; Dr. Chris Bretherton, for providing his code for radiation calculations; Dr. Piotr Smolarkiewicz for fruitful discussions and providing the three-dimensional monotonic positive definite advection code; Drs. Doug Johnson, Phil Austin, and Peter Duynkerke for providing the ASTEX A209 flight data; Dr. Claude Duchon for providing the code for the Lanczos filter.

I would also like to acknowledge the support by the NOAA OGP Grants NA37RJ0203, NA36GP0334, and by the ONR Grants N00014-96-1-0687, N00014-96-1-1112.

Finally, I thank my wife, Natalia Zagorouiko, whose love, support and understanding I appreciate so much. I owe a great deal of time and attention to my son, Dennis, whom I promise to make it up in the nearest future.

Table of Contents

List of Figures

List of Tables

Abstract

A new LES dynamical framework coupled with an explicit microphysical module has been developed. It is verified against analytical solution (linear mountain wave test) and against predictions from the other LES models. The results of the tests of the microphysical module convincingly show that the drop spectrum resolution in our model is adequate to accurately predict the cloud microphysics parameters.

The realism of the model is evaluated by a direct comparison of the model predictions with the aircraft observations of the STBL. The first case study is based on the UKMRF flight 526 measurements collected over the North Sea on 22 July 1982; the second case study corresponds to the ASTEX flight A209 flown on 12-13 June 1992. The model is able to reproduce reasonably well most of the observed boundary layer parameters, including turbulent fluxes and variances of various fields, intensity and vertical distribution of the turbulent kinetic energy, upward and downward radiation fluxes, and the cloud drop spectra.

I designed a new bulk microphysical parameterization using the explicit model as a benchmark for comparison. The liquid water is divided into two categories - non-precipitable cloud water and drizzle, similar to traditional Kessler-type parameterizations. The water content and drop concentration are predicted for each category. The source/sink terms such as autoconversion of cloud water into drizzle are deduced directly from the drop size spectra predicted by the explicit microphysical model. The predictions of the LES model using the new bulk microphysics are compared with the predictions using explicit microphysics for two cases: non-drizzling and heavy-drizzling STBL. The results show that the new bulk microphysical model satisfactory reproduces many characteristics of the STBL as simulated by explicit microphysical model.

A case of stratocumulus-to-cumulus transition triggered by the depletion of CCN is simulated. It is shown that the response of the STBL to the increase in drizzle

due to CCN depletion is the reduction of its cloud fractional cover and change of the character of circulation toward the cumulus convection. The boundary layer after the Sc-to-Cu transition consists of two layers: the well-mixed cloud free surface layer driven by surface heat fluxes and shear, and the conditionally unstable upper layer capped by the inversion with embedded cumulus clouds connected to the moisture and CCN supply in the surface layer.

Chapter 1

Introduction

1.1 Physics of the Stratocumulus-Topped Boundary Layers

At any given time stratus and stratocumulus clouds cover about 25% of the World Ocean (e.g., Charlson et al. 1987). They have relatively little impact on the outgoing thermal radiation as the cloud-top and surface temperatures are close to each other. On the other hand, they reflect much more sunlight than the underlying ocean, and, thus, increase the local planetary albedo by 30-50%. This effect is illustrated by Fig. 1.1, where two satellite images - in visible and infrared parts of the spectrum are shown. While the low-level clouds, both stratocumulus and shallow cumulus, have the same brightness as the visible spectrum range as the high altitude clouds, they have very low contrast compared to the underlying ocean in the infrared range of spectrum.

The important role the marine boundary layer clouds play in the Earth's global radiative balance and, therefore, climate is now well recognized. For example, a few percent increase of stratocumulus cloud cover or a comparable growth of their albedo would compensate the anticipated greenhouse warming due to doubling of the carbon dioxide in the atmosphere, while a similar decrease would double the warming (e.g. Randall et al. 1984, Ramanathan et al., 1989). Clearly, even a relatively small bias in representation of the stratocumulus clouds in the global circulation models (GCMs) could result in serious errors in the simulated global energy balance.

Figure 1.2 presents a schematic cartoon of the fundamental processes that drive the stratocumulus-topped boundary layer (STBL) dynamics. The stratocumulus

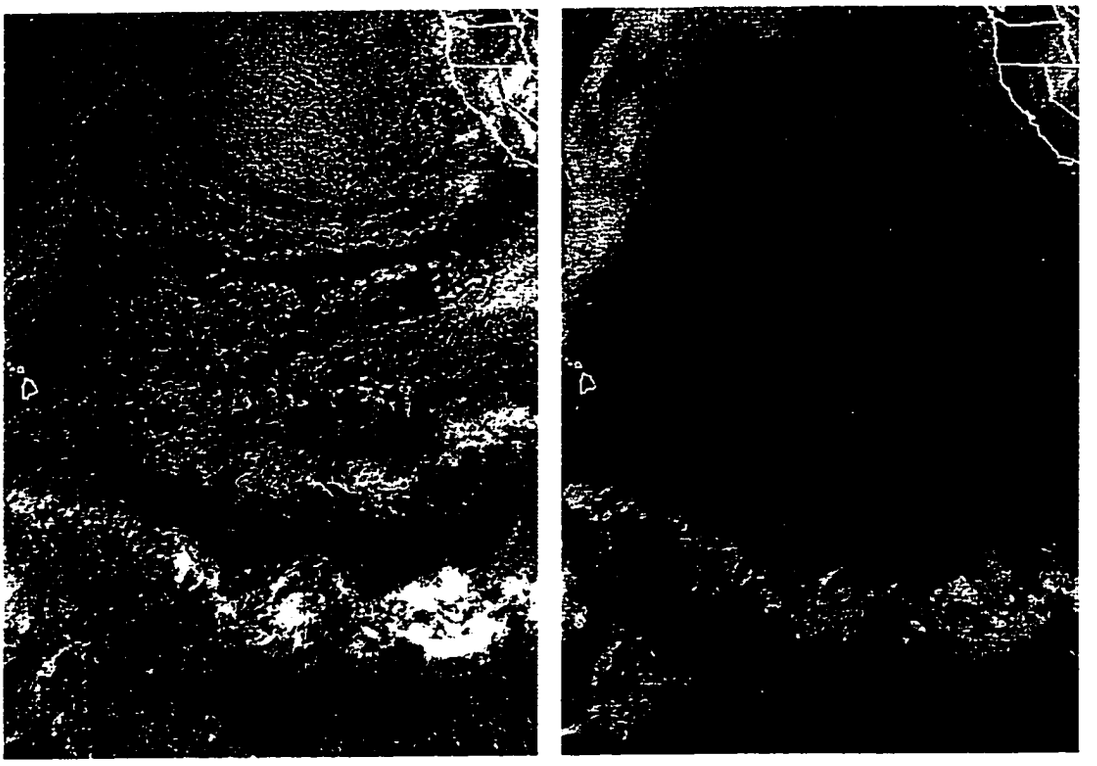

Figure 1.1 October 10, 1997 GOES -9 Satellite visible (left) vs. infrared (right) images of the Eastern Pacific.

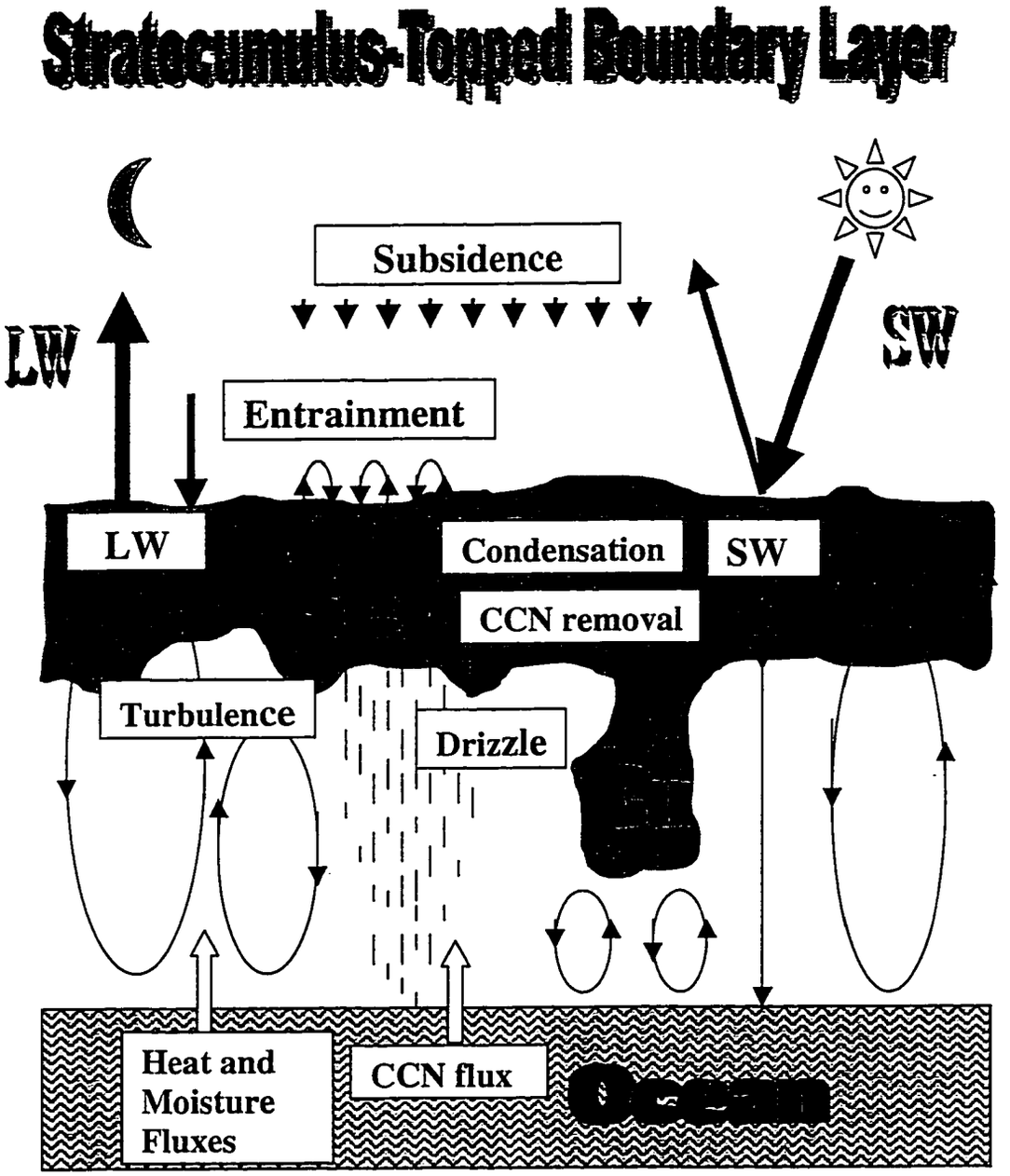

Figure 1.2 Diagram of the important processes in the marine stratocumulus-topped boundary layer.

cloud layers predominantly form over relatively cold waters formed by upwelling in the eastern parts of the oceans. Favored by the synoptic-scale subsidence, the interface between the air cooled by the ocean and the warm and relatively dry air of the free atmosphere is created in the form of a strong inversion. The mixing of the boundary layer by convection due to surface heat fluxes and its moistening due to evaporation from the ocean surface can create vapor saturation conditions close to the boundary layer top and consequently a cloud layer forms.

Since cloud water is a very efficient absorber of long wave (LW) radiation, the net LW radiation flux is close to zero within the cloud. At the same time, the cloud top emits upward as a blackbody, while receiving much less of the downward LW radiation from the cooler atmosphere above. As a result, the net radiation flux above the cloud top is positive and relatively large. The resultant divergence of the net LW radiation fluxes cools the cloud top region, so that air parcels become negatively buoyant and sink downward the surface. The cloud top radiative cooling and surface heat fluxes are two dominant sources of turbulence in the convective STBL.

During the day, the solar radiation also becomes important. Since absorption in the visible spectrum range is not as strong as in the LW range, warming due to the short wave (SW) radiation reduces the cloud top radiative cooling and corresponding buoyancy generation of TKE. This makes it more difficult for turbulence to maintain the well-mixed STBL. If the surface fluxes are relatively weak, which is often the case in marine STBL, the cloud layer, exposed to the SW heating, warms faster than the underlying layer. This leads to stabilization of the subcloud layer and consequent reduction of the turbulent fluxes from the surface to the cloud layer.

Stabilization of the subcloud layer can also be caused by drizzle due to evaporative cooling in the subcloud layer and latent warming in the cloud layer. The reduction of the moisture supply to the cloud leads to moisture accumulation near the surface, triggering eventually the development of cumulus clouds below the main

stratocumulus deck. These cumuli penetrate the Sc layer, bringing up moisture and effectively ventilating the surface layer.

Among other processes that are important for the STBL dynamics are cloud top entrainment and cycling of the cloud condensation nuclei (CCN). The effects of the former are more or less understood, although much remains to be done in representing this process in meso-scale and large-scale models. The latter is less understood, although the effects of CCN on regulating the cloud albedo and drizzle production rate have been a subject of intensive research for a few decades.

Since the classic paper by Lilly (1968), significant progress has been made in understanding the general nature of processes driving the stratocumulus-topped boundary layer dynamics. The main issues being addressed over the past decades have included, among others, cloud top radiative cooling (e.g., Nicholls and Leighton 1986, Moeng 1986), cloud top entrainment instability (e.g. Lilly 1968, Randall 1980, Moeng et al. 1995), mesoscale cellular convection (e.g. Rothermel and Agee 1980, Fiedler 1993, Fiedler and Khairoutdinov 1994), turbulence characteristics (e.g. Deardorff 1980, Moeng 1986), stratocumulus-to-trade-cumulus transition (e.g. Bretherton 1992, Krueger et al. 1995).

In addition to early comprehensive aircraft-based observations of macro- and microphysical structure of marine stratocumulus (e.g., Brost et al. 1982, Nicholls (1984), Nicholls and Leighton 1986), a series of field programs such as First ISCCP (International Satellite Cloud Climatology Project) Regional Experiment (FIRE) (Albrecht et al. 1988), and Atlantic Stratocumulus Transition Experiment (ASTEX) (Albrecht et al. 1995) was aimed at studying the processes in stratocumulus over the eastern North Pacific and the eastern North Atlantic. These field experiments have provided, perhaps for the first time, integrated observations of boundary layer dynamics, microphysics and radiation parameters. Comprehensive data accumulated over the past decade or so have inspired numerous studies of the processes and

interactions in the STBL using models of varying degrees of complexity and various physical processes.

In order to accurately simulate the turbulent dynamics of the STBL, the large eddy simulation (LES) models have been developed for more than two decades. The need to couple the accurate representation of the STBL turbulent dynamics with a physically sound representation of microphysics has led to development of LES models with explicit microphysics. The complexity and computational burden of these models explain why only a few have been developed so far. One of them is the CIMMS LES developed at the University of Oklahoma (Kogan et al. 1994, 1995), and another is the Colorado State University LES (Feingold et al. 1984, Stevens 1996). This type of LES model enables one to study the complex interactions among various STBL processes and provides a tool for development of more accurate parameterizations for the LES and larger scale models.

1.2 Drizzle and its effect on Stratocumulus

Although there have been observational (e.g. Brost et al. 1982, Nicholls 1984, Paluch and Lenschow 1991) and modeling (e.g. Chen and Cotton 1987, Nicholls 1987, Albrecht 1989, Baker 1993, Ackerman et al. 1995, Austin et al. 1995, Feingold et al., 1996) studies, precipitating stratocumulus have received significantly less attention than nonprecipitating clouds.

In the nonprecipitating STBL, the main effect of cloud on dynamics is through the latent heat release of condensation and cloud top radiative cooling. Drizzle can affect the dynamics and microphysics of STBL by the vertical redistribution of moisture and heat. Brost et al. (1982) showed that in the cloud layer drizzle depletes the liquid water available for evaporation. In the subcloud layer, the evaporation of drizzle

cools and moistens the layer resulting in its stabilization. Stabilization of the subcloud layer may lead to the decoupling of the cloud from the subcloud layer.

As shown by Nicholls (1984), decoupling of the subcloud layer causes moisture accumulation there due to both surface moisture flux and drizzle flux convergence. This decreases the lifting condensation level (LCL) as shown by Wang and Albrecht (1992), who analyzed the data collected during FIRE and showed that the difference between the LCL and the cloud top seems to be larger in the presence of drizzle. Paluch and Lenschow (1991) determined from FIRE data that on scales larger than 10 km the perturbations of moisture are negatively correlated with those of temperature in the subcloud layer because of the drizzle evaporation.

Nicholls (1984) found from aircraft observations that drizzle can be comparable in magnitude with or even larger than the other water substance fluxes, therefore depleting the cloud water content. As a result, the buoyancy flux may be reduced, and so may the turbulent kinetic energy. This implies that the cloud top cooling and entrainment flux must be reduced as well. Curry (1986) has also found that the drizzle flux was larger in many cases than the turbulent total water flux in the Arctic Stratus Experiment in June 1980 over the Beaufort Sea. Chen and Cotton (1987) found from their high-order turbulence closure model that drizzle can substantially deplete the cloud water content, reducing the cloud top radiative cooling and, therefore, turbulent kinetic energy.

Wang and Albrecht (1992) studying aircraft data from FIRE concluded that the effect of drizzle is usually localized, so that drizzle patches enhance the horizontal inhomogeneity of the STBL. They argued that the turbulence leg performed by an aircraft may not be long enough to calculate the ensemble mean turbulence statistics (e.g., Lenschow and Stankov 1986). Paluch and Lenschow (1991) have also showed from aircraft data the horizontal inhomogeneity in the temperature and moisture fields on the scales more than 10 km due to the drizzle evaporative cooling effect. Concerning

coverage of the surface by drizzle, Brost et al. (1982) found from the analysis of aircraft data that drizzle fell on only about 5% of the surface. Paluch and Lenschow (1991) observed this parameter as large as 30%.

Aircraft observations have also shown that the typical observed drizzle rate is of the order of 1 mm day^{-1} within the cloud layer (e.g. Brost et al. 1982, Nicholls and Leighton 1986), although the data collected during ASTEX revealed that in 15% of cases the drizzle rates can be significantly higher (Gerber, 1996). Analysis of the ASTEX data made by Gerber (1996) showed that there is a sharp increase in drizzle water content once the cloud top drop effective radius exceeds about 10-12 μm.

There have been a number of modeling studies based on simplified 1-D models with a goal to relate the drizzle production to such macroscale parameters as liquid water path (LWP) and average drop concentration (e.g., Nicholls 1987, Albrecht 1993, Baker 1993, Baker and Charlson 1990, Pincus and Baker 1994, Austin et al. 1995). Nicholls (1987), for example, found that the drizzle amount varies as the fifth power of the LWP, although Baker (1993) showed a weaker dependence. Baker and Charlson (1990) found that drizzle amount for a given LWP seems to increase as $N^{-1/3}$, where N is the drop concentration. Austin et al. (1995), however, discussed several ASTEX cases when the cloud layers differing by 60% in liquid water path and a factor of two in drop concentration produced similar drizzle rates.

From a cloud physics perspective, it is clear that the amount of drizzle is closely related to the CCN number concentration and size distribution (Twomey, 1977). Enhanced CCN concentration in the stratocumulus environment should lead to increased cloud drop concentrations and, therefore, given the same amount of liquid water content, to decreased drop sizes and smaller drizzle rates (Albrecht 1989). At the same time drizzle can be a very important factor in removing the CCN and, thus, setting their mean concentration in marine STBL environment (Baker and Charlson, 1990), so that CCN concentrations are higher in clear than in cloudy marine areas (e.g. Austin et

al. 1995). Another possible mechanism that can play an important role in triggering the drizzle is the presence of giant CCN (Beard and Ochs, 1993). Ackerman et al. (1993) have offered a mechanism for the collapse of the STBL as the result of dissipation of stratocumulus cloud layer due to depletion of CCN by drizzle.

Mason (1952) proposed that the turbulent motion in stratiform clouds should enhance the drizzle production by increasing their dwell-time in the cloud layer. To see how turbulence intensity affects drizzle production, Nicholls (1987) developed a stochastic model of drizzle in which random trajectories of coalescing drops were calculated. The vertical velocities were assumed to be distributed in a Gaussian type distribution function with the vertical velocity variance as a parameter. The analytical version of the Nicholls' model was further developed by Baker (1993) and Austin et al (1995) with several added features like parameterization of the autoconversion rates. These rather simplified models predicted that the precipitation rate increases with increase in the turbulence intensity. Feingold et al (1996) using a much more sophisticated 2-D eddy-resolving model with explicit microphysics have similarly concluded that stratocumulus cloud layers with more vigorous turbulent circulation allow for repeated coalescence cycles, thus, increasing the drizzle rates.

One of the most comprehensive studies of the effects of the drizzle on the STBL was done recently by Stevens (1996), who found from an LES model with explicit microphysics that a possible response of the STBL to strong drizzle is not decoupling of the cloud layer from the surface as a result of stabilization of the subcloud layer by drizzle. Rather, a strong coupling of the STBL occurs from cumulus-like circulation in the presence of internal stratification. My LES results in Chapter 6 strongly support this finding.

In summary, from one perspective, STBL dynamics has a strong effect on cloud microphysics. For example, the local cloud drop concentration is closely related to the magnitude of the supersaturation peak in the local updraft and to the local CCN count.

For a given liquid water content, which mostly depends on the vertical thermodynamical structure of the STBL, variations in the drop concentration imply variations in the mean drop size, and therefore, variations in the efficiency of drizzle production. In turn, the cloud microphysics can also have a strong effect on the STBL dynamics. For example, the vertical redistribution of heat and moisture by drizzle can significantly modify the dynamics and evolution of the STBL. The radiative properties of cloud layers can strongly depend on the drop size, especially for the absorption of solar radiation (e.g. Slingo, 1989). The most vivid illustration of the latter effect is the so-called ship condensation trail phenomenon (Radke et al. 1988).

1.3 Formulation of microphysics in cloud models

The strong effect of drizzle on the whole STBL structure implies that in order to successfully study the dynamics and microphysics of the STBL, one should simulate the drizzle as realistically as possible. No attempt is made here to review this broad subject. The main focus will be on the methods that are being or could be potentially applied in the LES framework to the problem of the drizzling STBL. Since this study is dealing with the marine stratocumulus over the relatively warm waters in middle latitudes, the treatment of ice processes is not discussed here. A more thorough review of the subject, including the ice microphysics, can be found in book by Cotton and Anthes (1989).

a. General considerations

The drop population in clouds is characterized by a large variety of sizes, from just a-few-micron drops, growing by the direct water vapor deposition, to a-few-

millimeter raindrops, growing mostly by accretion of smaller drops. The cloud drop population can be characterized by a drop size distribution function (DSD), which describes how many drops can be found in a given size range averaged over some time-space volume. Once the drop size distribution function is known, corresponding moments such as the drop concentration, liquid water content, mean radius, etc. can be directly calculated from the DSD.

The process of new drop nucleation, or CCN activation, is very complicated, and generally depends on such aerosol characteristics as mass, chemical composition, fraction of the soluble part of a particle to insoluble, etc (see, e.g., Pruppacher and Klett, 1997). In general, the CCN can be distributed by the critical supersaturation needed for their activation. The maximum value of supersaturation in a local updraft near the cloud base determines the cloud drop concentration. The latter, together with the liquid water content determines the characteristic cloud drop sizes in clouds. The coalescence of cloud drops is usually described by the so-called *quasi-stochastic coalescence integrals* (e.g., see Berry 1968), which predicts the gain and loss of mass of drops in a given size interval due to collisions with other drops. In addition, for large rain drops the process of breakup becomes important. Since the drop collision efficiency is very small for the smallest droplets and becomes larger for larger droplets, the rate of precipitable water generation is inversely related to CCN count (Squires 1958). Thus, in general, the adequate representation of CCN spectra is also needed for accurate representation of the cloud microphysics.

b. Explicit microphysics

A modeling approach when the DSD is explicitly predicted is referred to as the explicit microphysical formulation, or explicit microphysics. In this approach the cloud

drops are distributed among many (from several tens to about a hundred) size categories or bins. The drops in each individual bin are subject to such microphysical processes as condensation, gravitational sedimentation, and coalescence.

Complexity and diversity of the methods used in explicit microphysics would not allow me to describe them in more detail in this dissertation, which focuses on developing a new bulk microphysics scheme for LES models. I will only mention that 2D and 3D cloud models with explicit microphysics of various degree of the process refinment were developed by Arnason and Greenfield (1972), Clark (1973), Soong (1974), Hall (1980), and Kogan (1991) among others. To my knowledge, there are presently only two LES models of marine stratocumulus that employ explicit microphysics - the CIMMS LES (Kogan et al 1994, 1995) and the CSU LES model (Feingold et al. 1994).

The explicit microphysical approach, despite its complexity and computational expense, is based on current knowledge of the cloud physics and, in principle, allows one to simulate the cloud processes in great detail. However, in many practical applications, a simplified and much less computationally expensive formulation of cloud microphysics is desirable. In addition, the explicit microphysics cannot be generally used in meso-scale and larger scale models, because of the lack of spatial resolution of the small-scale velocity field, and, therefore, inability to predict the supersaturation field.

c. Bulk Microphysics

The alternative approach is to predict several DSD moments, such as liquid water content and cloud drop concentration. This approach is generally referred to as bulk microphysical parameterization, or bulk microphysics. Being relatively simple and

computationally efficient, bulk microphysics became a commonly used technique in cloud-scale, meso-scale, and even some GCM models (e.g. Fowler et al. 1996).

Currently, there is a variety of approaches to the parameterization of cloud microphysics. Some of the approaches, especially those that include the ice processes, are very complicated (e.g., see Cotton and Anthes 1989). In general, the variety can be reduced to two basic types of bulk microphysics: the Kessler-type and the Clark-type parameterizations.

Kessler started the most popular approach to the bulk microphysics in mid-60s. In this approach the liquid water is subdivided into two categories: non-precipitable cloud water and precipitable rain/drizzle water. This partitioning is supported by the fact that the growth rate of the former is determined by the direct deposition of the water vapor, while the growth of the latter is dominated by the accretion of the cloud water. The boundary between the cloud and precipitable water is not easy to define. For example, Berry and Reinhardt (1974a) showed that the threshold between cloud water and rain water droplets is at about 50 μm. In stratocumulus clouds, where precipitation is mostly in the form of drizzle, the threshold can be at 20-30 μm, as will be shown in Chapter 5.

The cloud water can be diagnosed from the thermodynamic parameters, like temperature and total water content, assuming that all the excess of the water vapor above the saturated mixing ratio instantly converts into the cloud water. Initialization of the rain/drizzle water is much more difficult to define, since the initial rain/drizzle embryo form as a result of spontaneous coalescence of smaller droplets, which is often referred to as *autoconversion*. By its nature, the autoconversion depends on the properties of the cloud drop spectrum, like spectrum broadness, mean drop size, etc. Therefore, this is the most difficult and uncertain part of any bulk microphysics, since the drop size spectrum information is not directly avilable.

The first and still, probably, the most popular formula for the autoconversion

rate was proposed by Kessler (1969), who hypothesized, based on empirical evidence, that the rate of autoconversion of cloud water q_c into rain water q_r is simply a linear function of the cloud water:

$$\left(\frac{\partial q_r}{\partial t}\right)_{auto} = K(q_c - q_{c0})H(q_c - q_{c0}) \qquad (1.1)$$

where q_{c0} is a threshold value for the cloud water for the autoconversion to occur, $H(x)$ is the Heaviside step function, and K is a constant in the order of 10^{-3} s^{-1}. Being simple, the approach (1.1) does not, however, differentiate between different air masses, for example, between the tropical marine and continental air masses. In addition, it is not clear how to select the time constant K, which is usually adjusted to reproduce the observed rain amount. Another concern is the value for the threshold water content q_{c0}. In the original formulation it is chosen to be 1 g/kg, which may be reasonable for the deep cumulus convection, but too large for the stratocumulus.

A refined formulation was offered by Berry (1968) based on the numerical solutions of the stochastic coagulation equation:

$$\left(\frac{\partial q_r}{\partial t}\right)_{auto} = \frac{q_c^3}{60N_c(2 + 0.0266/\sigma_r)} \qquad (1.2)$$

where σ_r is a drop spectrum relative dispersion and N_c is the drop concentration. Cotton (1972) analyzed (1.2) using his own coagulation routine based on Berry's method and concluded that (1.2) produces autoconversion rates larger than Kessler's original formulation. He also concluded, that Berry's methodology of calculating the autoconversion rate simulates the total mass transport (autoconversion plus accretion) rather than autoconversion only.

Berry and Reinhardt (1974a,b) used the Berry's methodology assuming that both cloud and rain water can be described by the log-normal distributions. As the result,

they proposed that the autoconversion rate can be expressed as

$$\left(\frac{\partial q_r}{\partial t}\right)_{auto} = A q_c^2 \tag{1.3}$$

where A is a rather complicated function of the cloud drop spectrum standard deviation and the cloud drop concentration.

A step toward the original simplicity of the Kessler's formulation was made by Manton and Cotton (1977) (see also Tripolli and Cotton 1980, Chen and Cotton 1987), where the autoconversion rate was expressed as a function of cloud water content and the cloud drop concentration as follows

$$\left(\frac{\partial q_r}{\partial t}\right)_{auto} = A q_c^{4/3} q_c H(q_c - q_{c0}) \tag{1.4}$$

Here the coefficient A is defined as

$$A = \frac{0.104\, g\, \rho_w E}{\mu\, N_c^{1/3}} \left(\frac{\rho_a}{\rho_w}\right)^{4/3} \tag{1.5}$$

where ρ_a and ρ_w are densities of air and water, respectively; E = 0.55 the mean drop collection efficiency, μ air viscosity; the threshold value q_0 is calculated as a water content of N_c drops with size equal to 10 μm. Qualitatively, the approach (1.4)-(1.5) is much more satisfying than the Kessler's formulation (1.1). The autoconversion rate is a stronger function of the cloud water and inversely proportional to the cloud drop concentration, providing a way to differentiate between different types of air masses. We can rewrite (1.4)-(1.5) in a rather different form defining the mean volume radius of the DSD as

$$r_{vc} = \left(\frac{3\, q_c\, \rho_a}{4\, \pi\, \rho_w\, N_c}\right)^{1/3} \tag{1.6}$$

The drops would have this size in a mono-disperse spectrum for a given value of cloud water and drop concentration. The equation for the fall speed of droplets smaller than

40 μm is given by the Stokes law

$$u = k_1 r^2 = \frac{2g}{9\mu}\rho_w r^2 \tag{1.7}$$

Then, the expressions (1.4)-(1.5) can be rewritten as

$$\left(\frac{\partial q_r}{\partial t}\right)_{auto} = \pi k_1 \overline{E} r_{vc}^4 N_c q_c H(r_v - r_{v0}) \tag{1.8}$$

Thus, according to (1.8), the autoconversion rate is a strong function of the volume radius consistent with the observational findings mentioned in previous section. Liou and Ou (1989) proposed a similar expression, although they used the mean forth-moment radius instead of the mean volume radius. The difference is apparent only for very broad cloud spectra, and small for the usually observed range of drop spectrum dispersion in stratocumulus. One problem with the original formulation was noticed by Baker (1993), who showed that (1.8) overestimates significantly the autoconversion rate in the warm trade cumuli. In order to correct the problem, she proposed that (1.8) should be multiplied by a factor which varies between 0.01 and 0.1. The same is probably true for the marine stratocumulus.

The autoconversion rate provides the way for the rain/drizzle initiation in a cloud model. The further growth of the precipitable water amount occurs by the accretion of the cloud water. The rate of accretion is usually derived using the fact that the rain drops are much larger than the cloud drops and therefore the accretion rate is proportional to the cloud water in the volume of a cylinder swept by a falling raindrop in the unit time. Then, in the assumption of continuous growth, the rate of change of rain/drizzle drop mass with radius R falling through the cloud region with the cloud water content q_c, assuming the collection efficiency between rain/drizzle drop and cloud drop is some constant $\overline{E}$, is given by

$$\frac{d}{dt}M(R)=\pi\bar{E}R^2V(R)\rho_o q_c \tag{1.9}$$

where $V(R)$ is the terminal velocity of the rain/drizzle drop of radius R. The rate of change of the total rain/drizzle water content due to accretion is expressed as

$$\left(\frac{\partial q_r}{\partial t}\right)_{accr}=\int_0^{\infty}N(R)\frac{dM(R)}{dt}dR \tag{1.10}$$

where $N(R)$ is the DSD for the rain/drizzle drops. The most popular approach to evaluating (1.11) follows Kessler's, who assumed the rain/drizzle drops to be distributed according to the to Marshall and Palmer (1948) distribution

$$N(R)=N_0\,exp(-\lambda R) \tag{1.11}$$

where N_0 and λ are some constants. Substituting (1.11) into (1.10) and assuming that the terminal velocity of the rain/drizzle drops can generally be expressed as

$$V(R)=kR^{\alpha} \tag{1.12}$$

where k and α are some constants, the accretion rate can be derived as

$$\left(\frac{\partial q_r}{\partial t}\right)_{accr}=\pi\bar{E}N_0k\frac{\Gamma(\alpha+3)}{\lambda^{\alpha+3}}\rho_0 q_c \tag{1.13}$$

For the raindrops, Marshall and Palmer found that N_0 could be taken as a constant equal to 0.08 cm^{-4}. It is typically assumed that the terminal velocity of the raindrops is proportional to the square root of their radius. It then can be easily derived that the accretion rate for rain is given by

$$\left(\frac{\partial q_r}{\partial t}\right)_{accr}=A\bar{E}q_c q_r^{0.875} \tag{1.16}$$

where A is a constant. The original Kessler parameterization essentially assumes that the so-called *intercept parameter* N_0 is a constant. Manton and Cotton (1977)

proposed, based on observational and modeling studies, that the slope of (1.11), defined as $d(\log N(R))/dR = \lambda$, is constant rather than N_0. The immediate consequence of this assumption is that q_r is linearly proportional to the rain/drizzle concentration N_r. Therefore, from (1.13), the expression for the accretion rate becomes

$$\left(\frac{\partial q_r}{\partial t}\right)_{accr} = A_1 \overline{E} q_c q_r \qquad (1.17)$$

Thus, the accretion rate is linearly proportional to the rain/drizzle water content. It is interesting to note that when the drizzle is a concern then the terminal velocity can be approximated as a linear function of the drizzle drop radius. In this case, both approaches - constant intercept parameter and constant slope - predict the linear dependency of the accretion rate on the drizzle amount, although with different values of constants A.

The other processes that need to be parameterized are the rain/drizzle evaporation and gravitational fall-out (sedimentation). The details of the parameterization of these processes are reviewed, for example, by Cotton and Anthes (1989) and will not be given here. The rain/drizzle condensation within cloud is generally ignored. This is a good approximation, because the rate of raindrop growth due to accretion of cloud water is much higher than by condensation. Outside the cloud, though, the evaporation of rain/drizzle water must be taken into account, which is usually calculated assuming the Marshal-Palmer distribution.

In addition to the classic Kessler-type approaches to the bulk microphysics, there is a class of methods that attempt to mimic the explicit microphysics by *a-priori* prescribing the shape of the DSD by a series of appropriate analytical functions. I call this method a Clark-type approach, since it has been started by Clark (1976) and continued by Clark and Hall (1983), where the cloud spectrum was approximated by a series of gamma- or log-normal distributions. The idea is to use a truncated series of

these functions to represent the evolution of the cloud spectrum due to condensation and coalescence. In this case there is no artificial division into cloud and drizzle water, and therefore, no need for the autoconversion. Several prognostic equations are solved for the parameters describing the basis functions. The coagulation, for example, is handled by a direct integration of the stochastic coagulation equation similar to the explicit microphysics with the difference that the results of calculation can be calculated once for the whole space of the prognostic parameters and stored as look-up tables.

The Clark method is very promising and significantly more efficient than the explicit approach, and potentially it might replace the explicit microphysics in many applications without compromising the accuracy of calculations. However, in my opinion, it is much more complicated compared to the Kessler-type approaches, and probably takes no less effort to be developed than the explicit approach, unless the ready-to-use subroutines are provided.

1.4 Study motivation and objectives

The LES approach has become now one of the leading methods driving our understanding of the STBL processes. While all LES models adequately simulate the turbulent dynamics of the convective STBL, most of them lack a satisfactory representation of cloud microphysics. Until recently, for almost two decades, the common tendency in LES community has been to completely ignore the microphysics and to use a simple saturation adjustment schemes to handle the condensation (so called "all-or-nothing" approach). Many LES models (especially those that were transformed over from the meso-scale models), in general, have the capabilities to produce precipitation. However, most of them were developed to apply to Cu convection.

As noted by Cotton and Anthes (1989, p. 94), the autoconversion rates given by

different expressions (some are presented in the previous section) can vary several orders of magnitude for a given liquid water content. Parameterization of the autoconversion rate is a particularly challenging problem in the stratocumulus studies, since due to relatively small liquid water contents (typically not exceeding 1 g kg^{-1}) compared to the Cu clouds, the conversion of cloud water to drizzle is marginal. In addition, since the autoconversion rates in Sc clouds can be comparable in magnitude to the accretion rates (same reference above), the accurate treatment of the drizzle initiation process can be of the greater importance than in Cu clouds.

Thus, there is a clear necessity to develop a bulk microphysical formulation to be specifically applied in STBL models. The assessment for accuracy of the bulk formulation could be based on how well it predicts the key *macro* and *micro* parameters, such as liquid water content, drop concentration, drizzle rate and some others, derived from the explicit microphysical model. The latter can be considered as the most physically based approach to the cloud modeling in general, because it directly applies the fundamental knowledge of cloud physics established from both laboratory measurements and field observations.

However, the advancement in the microphysical formulation by predicting drop distribution function and the added level of complexity of the CIMMS LES model necessitates a vigorous program to verify its overall performance. One of the ways to gain confidence in a model is to directly compare its output with the data derived from aircraft measurements of the STBL.

In summary, the main objectives of this study are:

- Refine the CIMMS LES model with explicit formulation of microphysics and verify its predictions against observations from comprehensive data sets including turbulent, microphysical, and radiative measurements in the stratocumulus-topped boundary layers.
- Develop a bulk microphysical parameterization able to accurately simulate the

principle *macro-* and *micro*physical characteristics of STBL using the explicit microphysical model as a benchmark for comparison.

In addition, in order to illustrate that the cloud microphysics can significantly affect the boundary layer dynamics, I will report the results of a simulation of the stratocumulus-to-cumulus transition triggered by depletion of CCN by drizzle.

The dissertation is organized as the following. In Chapter 2, the CIMMS LES model is described. The results of the tests of the model's numerics are given in Chapter 3. Comparison of the model's predictions with the aircraft observations is discussed in Chapter 4. The new bulk microphysical parameterization is developed in Chapter 5. The Sc-to-Cu transition as the result of rapid CCN depletion by drizzle is described in Chapter 6. The work will be summarized in Chapter 7.

Chapter 2

The CIMMS LES Model

One of the problems with the previous version of the CIMMS LES (Kogan et al. 1995) was the absence of a unified numerical formulation for the dynamical and microphysical variables. Computation of the dynamical tendencies for all thermodynamical variables was based on spectral code by Moeng (1984), while the dynamical tendencies for microphysical variables were evaluated using the finite-difference methods. The spectral method allows accurate calculation of the momentum equations; however, the lack of positive definiteness makes it unfit for calculation of scalar advection. Therefore, in the previous version of the model, the spectral method for the momentum equations was combined with the Smolarkiewicz positive-definite finite-difference scheme for calculation of the dynamical tendencies for the microphysical variables. As constraints imposed by the continuity equation were satisfied using the spectral formulation, the velocity field becomes divergent in the finite-difference representation, resulting in rather large errors in advection of the microphysical fields. The errors decreased in simulations with fine grid resolutions; however, for coarse or medium resolution simulations the errors were still appreciable. The problem was solved by developing a new dynamical framework with finite-difference representation of the velocity field divergence and employing the same finite-difference representation for all model variables - thermodynamical and microphysical.

The second modification was the development of a completely new variational optimization method for the drop spectrum remapping in the semi-Lagrangian condensation/evaporation calculations (Liu et al. 1997). Compared to previously used

Kovetz and Olund (1969) method, the variational method significantly minimizes the artificial drop spectrum broadening, and, consequently, allows one to model the drizzle initiation processes more accurately.

2.1 Dynamical Framework

Following the LES methodology (e.g., see Mason 1994), all governing equations in an LES model are spatially filtered using an explicit filter (see, e.g., Moeng 1984), or an implicit filter by averaging over an individual numerical grid cell, as used in our model. The averaged equations will then have additional terms associated with the transport by unresolved-by-the-grid or subgrid-scale (SGS) eddies, which have to be parameterized in terms of the resolved fields. In an LES model, the resolution of a grid is chosen such that contribution to the turbulent kinetic energy and fluxes from the SGS eddies is relatively small, except for the flow near boundaries, where the SGS contribution can dominate. In addition, the grid resolution should be within the inertial sub-range of turbulence, so that the main role of the SGS parameterization is to dissipate the resolved-scale turbulent kinetic energy.

The governing equations for the resolved velocity field are the grid-averaged Navier-Stokes and continuity equations for incompressible fluid in the Boussinesq approximation:

$$\frac{\partial \overline{u}_i}{\partial t} = -\frac{\partial}{\partial x_j}\left(\overline{u}_i \overline{u}_j + \delta_{ij}\theta_0 \overline{\pi}' + \tau_{ij}\right) + \delta_{i3} g \frac{\overline{\theta}_v'}{\theta_0} + \varepsilon_{ij3} f\left(\overline{u}_j - u_{gj}\right) \quad (2.1)$$

$$\frac{\partial \overline{u}_i}{\partial x_i} = 0 \quad (2.2)$$

Here $\overline{u}_i$ (i = 1, 2, 3) are the resolved-scale wind components u, v, and w, respectively,

π the Exner function of pressure, τ_{ij} the sub-grid Reynolds stresses, θ_v the virtual potential temperature; θ_0 the reference potential temperature, f the Coriolis parameter, and u_{gj} the geostrophic wind. Bars over individual variables represent the resolved-by-grid quantities, while primes denote the perturbations from their horizontal mean values.

The thermodynamic state is described in terms of the liquid water potential temperature θ_l and the total water content q_T, which are conserved in moist adiabatic processes. The θ_l is defined following Moeng (1986): $\theta_l = h_l / c_P$, where h_l is the virtual liquid water static energy. The conservation equations for θ_l and q_T are given in the form:

$$\frac{\partial \overline{\theta}_l}{\partial t} = -\frac{\partial}{\partial x_i}\left(\overline{\theta}_l \overline{u}_i + \tau_{i\theta}\right) - \frac{1}{\rho c_p}\frac{\partial F}{\partial z} + \frac{L}{c_p}\frac{\partial P}{\partial z} - w_s \frac{\partial \overline{\theta}_l}{\partial z} \qquad (2.3)$$

$$\frac{\partial \overline{q}_T}{\partial t} = -\frac{\partial}{\partial x_i}\left(\overline{q}_T \overline{u}_i + \tau_{iq}\right) - \frac{\partial P}{\partial z} - w_s \frac{\partial \overline{q}_T}{\partial z} \qquad (2.4)$$

Here P is the total precipitation flux, Q the net radiation flux, $\tau_{i\theta}$ and τ_{iq} the sub-grid fluxes of θ_l and q_T, respectively, w_s the large-scale subsidence rate.

The Reynolds stresses and subgrid scalar fluxes are assumed to be proportional to the local gradients of the resolved-scale quantities by the direct analogy with the physical diffusion:

$$\tau_{ij} = -K_m\left(\frac{\partial u_i}{\partial x_j} + \frac{\partial u_j}{\partial x_i}\right) \qquad \tau_{\varphi j} = -K_m \frac{\partial \varphi}{\partial x_j}, \qquad (2.5)$$

Here φ is any scalar variable, Km and Kh are the "eddy viscosity" and "eddy

diffusivity" coefficients, respectively. In order to find these coefficients, the 1.5 order SGS closure based on the prognostic equation for the SGS turbulent kinetic energy (TKE) $e = 0.5(\overline{u_i u_i} - \overline{u_i}\,\overline{u_i})$ proposed by Lilly (1967) and further developed and applied for the LES by Deardorff (1980):

$$\frac{\partial e}{\partial t} = -\frac{\partial}{\partial x_j}\left(\overline{e u_j} - 2K_m \frac{\partial e}{\partial x_j}\right) + \frac{K_m}{2}\left(\frac{\partial u_i}{\partial x_j} + \frac{\partial u_j}{\partial x_i}\right)^2 - K_h N^2 - \frac{C_\varepsilon e^{3/2}}{l} \quad (2.6)$$

$$T \qquad S \qquad B \qquad D$$

where l is the SGS length scale, N is the moist Brunt-Väisälä frequency, and C_ε is some nondimensional constant. Physically, the equation (2.6) means that the SGS TKE can change due to the advective and diffusive transport (T), production by the shear of the resolved flow (S), SGS buoyancy production/consumption in the case of local unstable/stable stratification (B), and viscous dissipation (D).

The SGS length scale l depends on the stratification and is calculated following D80 as

$$l = \begin{cases} \Delta & if \;\; N \le 0 \\ max\left[0.1\Delta, min(\Delta, 0.76\sqrt{e/N})\right] & if \;\; N > 0 \end{cases}, \quad (2.7)$$

where $\Delta = (\Delta x\, \Delta y\, \Delta z)^{1/3}$ is the characteristic grid size. Finally, the coefficients K_m and K_h are defined as

$$K_m = C_k l e^{1/2}, \qquad K_h = (1 + 2l/\Delta) K_m \quad (2.8)$$

The coefficients C_k and C_ε are empirical, although can be estimated from the isotropic turbulence theory for inertial subrange (Lilly, 1967). In the current version of the CIMMS LES $C_k = 0.1$ and $C_\varepsilon = (0.19 + 0.51\, l/\Delta)$ are taken similar to Deardorff (1980).

2.2 Microphysics

The explicit microphysical framework in the model was originally designed by Kogan (1991) for a cumulus cloud model. Two drop size distribution functions or size spectra are predicted: one for the cloud drops and the other for the cloud condensation nuclei (CCN). The drop size spectrum is represented by 29 bins logarithmically spaced in the range from 1 to 645 μm, which is sufficient to study drizzling STBL. The total number of CCN categories is chosen to resolve the CCN size spectrum in the size range from 0.0076 to 7.6 μm and varies, depending on the specific problem, from 8 to 19 bins. The CCN spectra after drop evaporation are restored to the initial shape, although the total number of CCN is allowed to decrease due to washout by drizzle. This approach guarantees the conservation of the total particle number during drop evaporation, and is adequate for the relatively short (up to several hours) simulations considered in this study. For longer integration times, the cloud may substantially transform the initial CCN spectra, both by decreasing the total CCN number and its activity. Unfortunately, very little is known about the CCN processing by clouds, and physical parameterization of the CCN regeneration for long-time simulations of the STBL yet needs to be developed.

2.3 Radiation

The longwave and shortwave radiation fluxes, as well as associated heating and cooling rates, are calculated following the approach by Wyant et al. (1997). The solar radiation is treated using the three-band approximation with the absorption coefficient for the cloud drops evaluated through the drop effective radius. The longwave radiation is treated by the one-band approximation with the non-exponential

absorption by the water vapor and exponential absorption by the liquid water. The calculation of the cloud water absorption coefficient k_C is modified in our model by the direct integration over the cloud drop spectra following Roach (1976) and Roach and Slingo (1979):

$$k_c = \frac{1.66}{q_L}\int_0^\infty n(r)Q(r)\pi r^2 dr \tag{2.9}$$

Here $n(r)$ is the drop size distribution function, r is a drop radius, and $Q(r)$ is the drop absorption efficiency factor approximated by

$$Q(r) = 1.18[1 - exp(-0.28r)] \tag{2.10}$$

where r is given in μm.

In the case of explicit microphysical model n(r) is known, and the absorption coefficient can be obtained directly from (2.9). In the bulk microphysical version of the model, it is assumed that cloud drop spectra are described by the Gamma-distribution:

$$n(r) = \frac{N_d \beta^{\gamma+1}}{\Gamma(\gamma+1)} r^\gamma exp(-\beta r), \tag{2.11}$$

where N_d is cloud drop concentration, r drop radius, $\Gamma(x)$ gamma-function, γ a parameter of the distribution related to the spectrum width, and β can be expressed as

$$\beta^3 = \frac{4\pi\rho_w N_d}{3q_L}(\gamma+3)(\gamma+2)(\gamma+1) \tag{2.12}$$

where ρ_w is the liquid water density. Substituting (2.10-2.12) into (2.9) yields the following expression for the cloud droplet absorption coefficient:

$$k_c = \frac{1.245\,a}{\rho_w r_{eff}}\left[1 - \left(1 + \frac{br_{eff}}{(\gamma+3)}\right)^{-(\gamma+3)}\right] \tag{2.13}$$

where the effective radius r_{eff} is given by

$$r_{eff} = \frac{\gamma + 3}{\beta} \tag{2.14}$$

The parameters of the Gamma-distribution are calculated from the bulk microphysical model as described in Chapter 5.

2.4 Boundary Conditions

The top and bottom boundaries are rigid-lid (w=0), which implies that all resolved-scale vertical fluxes vanish there, so that the vertical transport of momentum and scalar quantities is solely done by the SGS motion. This vertical transport at the surface is parameterized assuming that the surface layer, or the layer of constant fluxes, extends from the surface up to height of the first grid level h, where scalars and horizontal velocity components are computed. Provided with the mean wind $\langle U \rangle = \langle \sqrt{\overline{u}^2 + \overline{v}^2} \rangle$, mean virtual potential temperature $\langle \theta_v \rangle$ and moisture $\langle q_v \rangle$ at the height h (angular brackets denote the horizontal averaging), and given the surface virtual potential temperature θ_{vs} and moisture q_{vs}, the local surface fluxes of heat, moisture and momentum can be defined as following:

$$-\overline{w'\theta_v'} = C_h \{\langle U \rangle (\theta_v - \theta_{vs}) + (U - \langle U \rangle)(\langle \theta_v \rangle - \theta_{vs})\} \tag{2.15}$$

$$-\overline{w'q_v'} = C_h \{\langle U \rangle (q_v - q_{vs}) + (U - \langle U \rangle)(\langle q_v \rangle - q_{vs})\} \tag{2.16}$$

$$-\overline{w'u'} = C_m \{\langle U \rangle u + (U - \langle U \rangle)\langle u \rangle\} \tag{2.17}$$

In expressions (2.15)-(2.17) the local fluctuation of the wind speed is taken into account similar to the approach described in Moeng (1984). Note, the drag coefficients are the same for all grid points. If the expressions (2.15)-(2.16) are horizontally averaged, then the conventional bulk aerodynamic formula for momentum and scalar fluxes can be obtained. The unknown drag coefficients for momentum C_m and heat C_h are found

applying the Monin-Obukhov surface layer similarity theory. The algorithm follows the one proposed by Kazakov and Lazariev (1978).

Let us define the bulk Richardson number as $R = gh(\langle\theta_v\rangle - \theta_{vs})/\theta_o \langle U\rangle^2$. From the similarity theory

$$\langle U\rangle = \frac{u_*}{\kappa}\psi_m(\zeta_h, \zeta_0); \quad \langle\theta_v\rangle - \theta_{vs} = \frac{\theta_*}{\kappa}\psi_h(\zeta_h, \zeta_0), \tag{2.18}$$

where u_* is the friction velocity scale; θ_* is a temperature scalede fined as a ratio of the heat flux to u_*; $\kappa = 0.4$; $\zeta_h = h/L_m$; $\zeta_0 = z_o/L_m$; z_0 is a roughness length; $L_m = u_*^2\theta_0/(\kappa g\theta_*)$ is the Monin-Obukhov length; Ψ_m and Ψ_h are the bulk universal similarity functions for momentum and heat, respectively:

$$\psi_i(\zeta_h, \zeta_o) = \int_{\zeta_o}^{\zeta_h} \zeta\phi_i(\zeta)d\zeta \qquad i = m, h \tag{2.19}$$

where $\phi(\zeta)$ are the universal similarity functions. Using expressions (2.18), the bulk Richardson number can be rewritten as

$$R = \zeta_h \frac{\psi_h(\zeta_h, \zeta_o)}{\psi_m^2(\zeta_h, \zeta_o)}. \tag{2.20}$$

Since R is already known, and $\zeta_0 = \zeta_h z_0/h$, the equation (2.20) can be solved for ζ_h. Once ζ_h is known, the values of the bulk universal functions can be calculated. Finally, the drag coefficients for momentum C_m and scalars C_h are calculated as

$$C_m = \frac{\kappa^2}{\psi_m^2}; \quad C_h = \frac{\kappa^2}{\psi_m\psi_h}. \tag{2.21}$$

The bulk universal functions in the current version of the model were chosen according to Businger et al. (1971). To close the parameterization, the roughness length z_0 is either specified or, for water surfaces, calculated according to Charnock (1955)

formula: $z_0 = 0.035\, u_*^2 / g$. Two versions of the surface flux parameterization are implemented in the model. In the first version, the temperature of the surface is specified. The surface moisture is then assumed equal to the saturation-mixing ratio when maritime conditions are considered. In the second version, the horizontally averaged virtual potential temperature flux rather than surface temperature is specified. In this case an iterative procedure is used as following. Starting with the first guess for θ_{vs} (its value from the previous time step, for instance), the mean flux is calculated as described above. If the specified value is not reached, the θ_{vs} is corrected by a simple algorithm. The procedure is repeated until the mean flux is within some error margin from the specified value. The obtained surface temperature and drag coefficients are then used to calculate the local fluxes.

At the upper boundary, the vertical gradient of the scalars is maintained constant in accord with their initial values, while SGS momentum flux is set to zero. To minimize the effect of reflecting the vertically propagating gravity waves from the top of the domain, an absorbing layer with Rayleigh-type damping is introduced at the upper part of the domain. The lateral boundaries are periodical.

2.5 Numerics

The finite difference representation is based on the staggered Arakawa C-type grid, which defines the velocity components at the sides and the pressure and all other scalar quantities at the center of an individual grid cell. The advection of momentum is computed using the advection scheme in flux form, with an option to select the order of spatial accuracy from the second to fifth. The advection scheme is centered for the even and upwind-biased for the odd orders of accuracy and analogous to ones given by

Tremback at al. (1987), but without the extra terms needed for the accuracy in time (in fact, the same order approximation in time as in the space) when a simple one-step forward scheme in time is used. Instead, the time integration in our model is performed using the third-order Adams-Bashforth (AB) scheme with a variable time step. We keep the option to select the order of the spatial accuracy to control aliasing at the smallest resolved scales needed for some model applications. In the LES simulations, the even-order centered schemes are preferred to avoid the numerical dissipation in addition to the physical dissipation provided by the SGS parameterization.

One of the features of the model is that the advection of all scalar variables (microphysical and thermodynamical) is treated consistently using one scheme - a fully three-dimensional positive definite advection scheme with monotonic corrector of Smolarkiewicz and Grabowski (1990). The SGS diffusion operator is approximated by the second-order centered differences. In order to diagnose the pressure perturbations, the corresponding Poisson equation is solved employing the Fast Fourier Transformation technique in both horizontal directions and the fast tri-diagonal matrix solver in the vertical direction. The algorithm is rather efficient and takes about 6% of CPU needed for the dynamical framework calculations.

The numerical techniques used for explicit formulation of microphysics are described in Kogan (1991). The drop spectrum evolution due to condensation/ evaporation step is computed using the semi-Lagrangian approach. The resultant spectrum should then be remapped back into the Eulerian grid in the drop size space. As was mentioned before, the current version of the model employs the new variational optimization method of Liu et al (1997). The method conserves four moments of the drop size distribution function and significantly minimizes the artificial numerical diffusion of the drop spectra without sacrificing the computational efficiency of the code. The stochastic coalescence equation is solved by the Berry and Reinhardt (1974b) method.

Chapter 3

Tests of the Model

3.1 Dynamical framework

a. Mountain-wave test

In order to test the new LES dynamical framework, several simulations were performed to test the overall accuracy. Among them is a simulation of a two-dimensional linear hydrostatic mountain wave flow, which has an analytical solution. The conditions of the test are similar to those used by Durran and Klemp (1983). The atmosphere is isothermal at 250 K. The air density is constant with height. The perturbations are induced by 20 ms^{-1} flow over the bell-shape 1-m high "mountain" with 10 km half-width. In the simulation, the mountain was introduced by specifying the vertical velocity at the lowest grid level equal to the analytical solution. In the absence of viscosity, this condition is self-sufficient. The computational domain is 320 x 18 km^2 and contains 320 points in the horizontal and 180 points in the vertical. The SGS parameterization is turned off. The absorbing layer occupies the upper third portion of the domain. Since the model uses periodical boundary conditions in the horizontal, the perturbations downstream from the mountain appear upstream, which may alter the solution. To minimize that effect, the Rayleigh absorbing is also applied near the outflow boundary, so that the inflow is undisturbed.

The vertical velocity field after 3000 time iterations for the central portion of the domain is shown in Fig. 3.1a with the corresponding analytical solution in Fig. 3.1b.

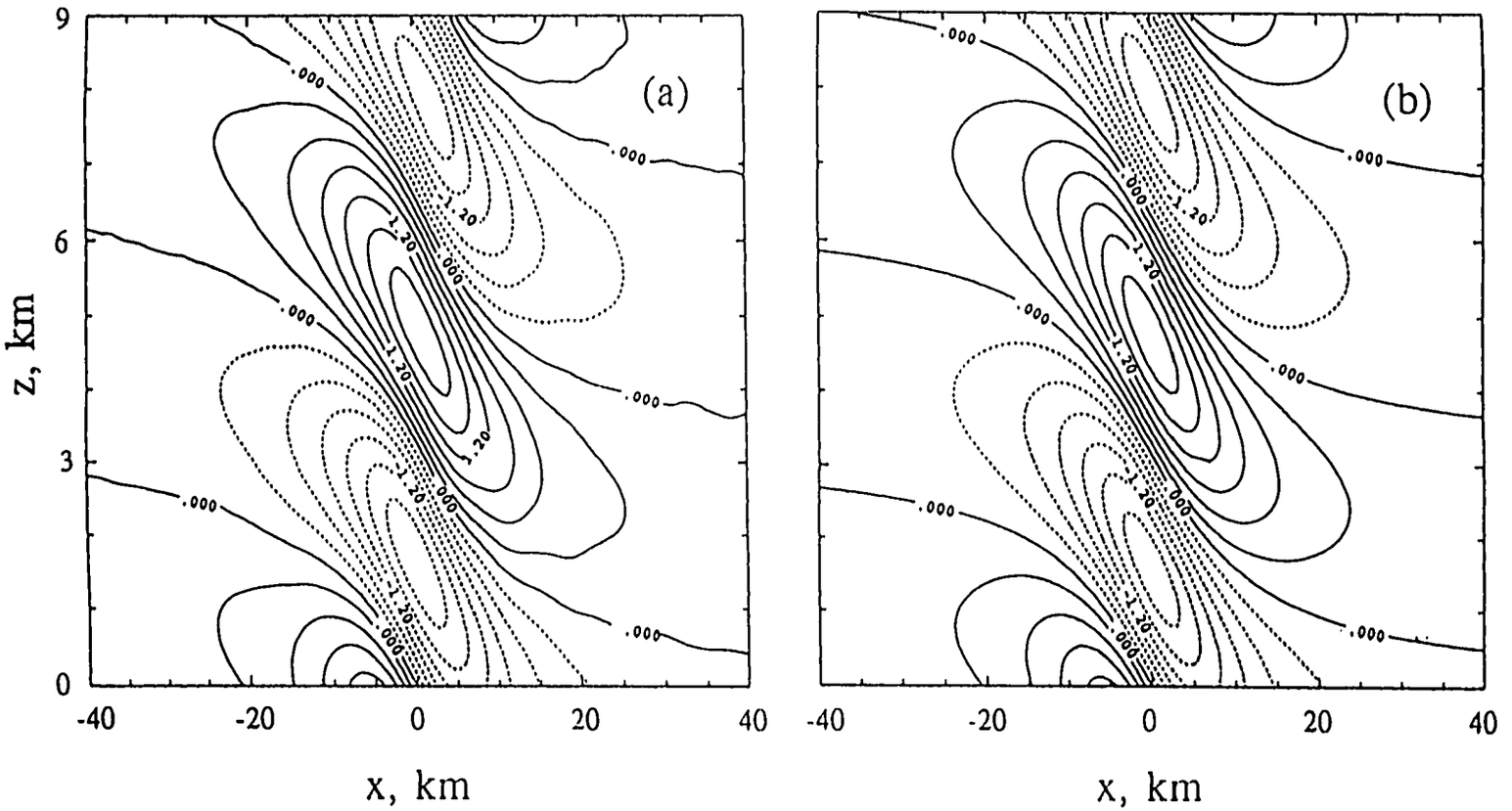

Figure 3.1 Isolines of the vertical velocity for the (a) simulated and (b) analytical solutions in the mountain-wave test.

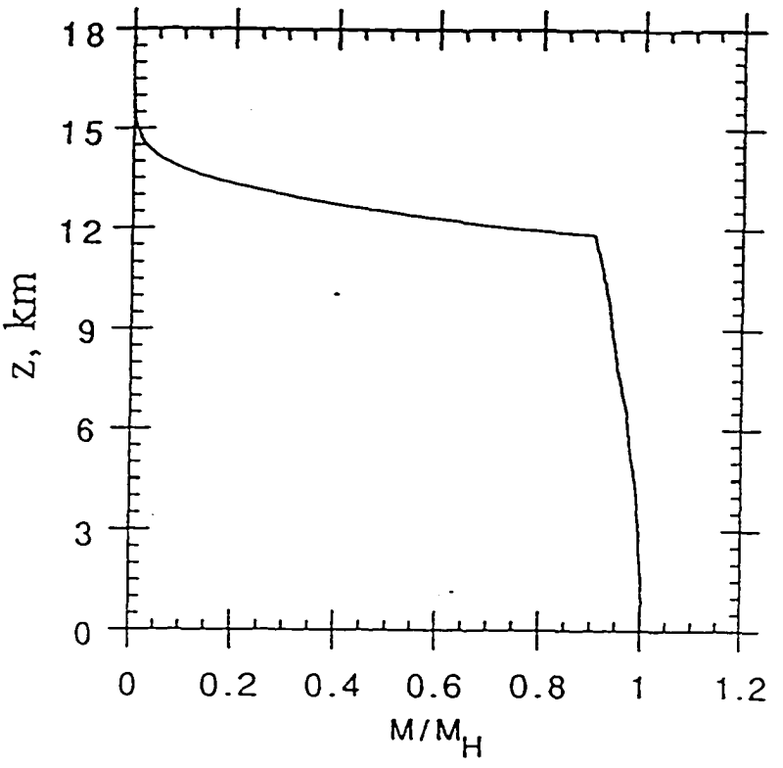

Fig. 3.2 Vertical profile of the simulated vertical momentum flux M nondimensionalized by its analytically derived value M_H for the mountain-wave test. A sharp decrease of the flux above the 12 km level is caused by the Rayleigh absorption layer introduced in the model to avoid the wave reflection from the top boundary.

A very good agreement between the numerical and analytical solutions is evident. A slight noise seen in the numerical solution is due to the outflow absorption being not completely efficient, so the inflow is slightly perturbed. An important measure of the computational error is the vertical flux of the horizontal momentum, which in this case should be constant with height. The vertical profile of the flux normalized by its analytically derived value, given in Durran and Klemp (1983), is shown in Fig. 3.2. Again, one can see a good agreement below the absorbing layer. The slight decrease in the momentum flux down to 90% of the analytical value is mostly attributed to the unavoidable small numerical diffusion associated with the Smorarkiewicz and Grabowski scheme used for the temperature transport.

b. Comparison with other LES models

As additional test of the overall performance of the LES model, I have compared its output with that from four other LES models (Nieuwstadt et al. 1991, further referred to as N91). The test case is a dry, convective boundary layer without capping inversion and mean wind. The potential temperature is initially well mixed up to 1350 m and is linearly increasing with a lapse rate 3 K/km above. The turbulent motion is driven by a constant temperature flux Q_s = 0.06 Kms^{-1}. The simulation time is chosen such that the final boundary layer height is about z_{i0}=1600 m, and a convective velocity scale, defined as $w_* = (gQ_s z_{i0} / \theta_0)^{1/3}$, is 1.46 ms^{-1}. The horizontal dimensions of the domain are 6400 X 6400 m with 40 X 40 grid points as in N91. The vertical dimension is 3000 m with 50 points. The simulation time is 11 t_*, where $t_* = z_{i0} / w_*$ is the eddy-turnover time. The variables chosen for intercomparison are averaged in time during the last eddy-turnover time. Different

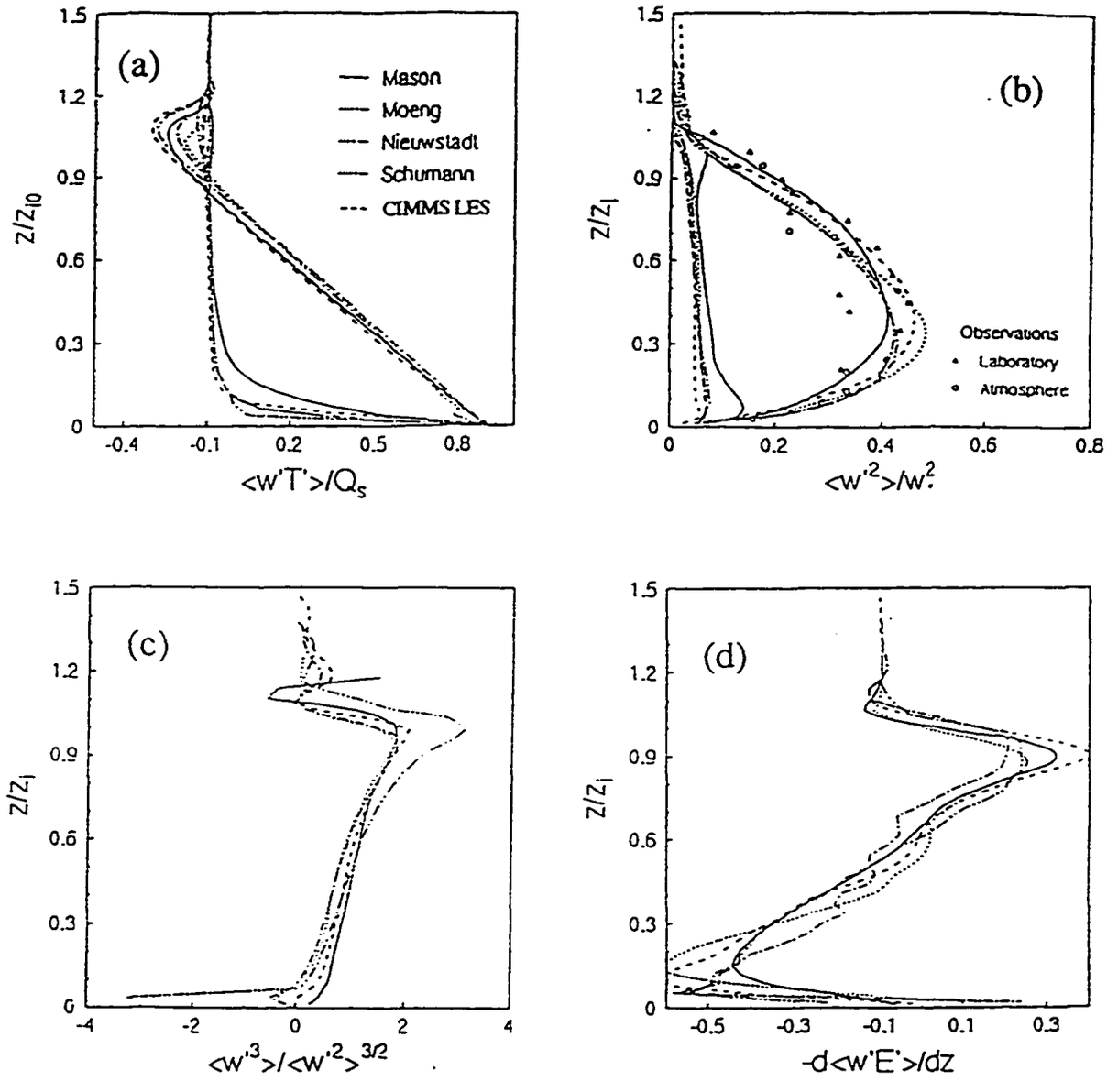

Figure 3.3 Comparison of the CIMMS LES model output with four LES models (Nieuwstadt et al. 1991) for the cloud-free convective boundary layer case: (a) non-dimensional buoyancy flux, (b) vertical velocity variance, (c) vertical velocity skewness, and (d) the vertical divergence of the TKE flux. The curves corresponding to the CIMMS LES are plotted on top of the figures taken from Nieuwstadt et al. (1991).

models in N91 used different number of time steps to calculate averages - from 4 to 40. I have used 30 time steps in our simulation.

Table 1. The actual mixed layer height z_i, convective velocity scale w*, entrainment flux - $(w'\theta')_i$, surface θs and mixed layer mean θ_m potential temperatures obtained by the CIMMS LES as compared with four different model results reported in Nieuwstadt et al. (1991).

Parameter	Mason	Moeng	Nieuwstadt	Schumann	CIMMS LES
z_i/z_{i0}	1.0563	1.0312	1.0688	1.0900	1.0875
w^*/w^*_0	1.018	1.010	1.022	1.029	1.028
$(w'\theta')_i/Q_s$	0.147	0.106	0.118	0.188	0.198
θs (K)	302.17	301.53	302.54	302.50	302.34
θ_m (K)	300.55	300.57	300.58	300.57	300.56

Table 1 and Fig. 3.3 summarize the simulation results for all five models. The actual boundary layer height, calculated as a height of the minimum temperature flux or entrainment flux and normalized by z_{i0}, is in good agreement with those reported in N91, and so is the actual vertical velocity scale w^*. From Table 1 one can also see, that all models vary considerably in the prediction of the entrainment flux. Our model predicts the entrainment flux which is 5% larger than the one predicted by the Schumann's model. In N91, it is agreed that such a discrepancy is due to the differences in the numerical techniques, since most of the entrainment flux is resolved. Another predicted parameter is the surface temperature, which varies about 1 K among the models, possibly due to different similarity functions used. The models also produced approximately constant potential temperature throughout the boundary layer, the mean values of which are nearly the same for all models. The temperature flux shown in Fig. 3.3a is nearly linear in the vertical and is largely resolved, except near the surface.

Other important characteristic of the boundary layer is the vertical velocity variance, shown in Figs. 3.3b. The agreement between our model and the other models is very good and within the scatter of the experimental data. The agreement in prediction of the third moment of the vertical velocity is also good, as demonstrated

by the vertical velocity skewness (Fig. 3.3c) defined as a non-dimensional ratio of the third moment to the variance. Note that only the resolved-scale vertical velocity skewness is shown.

The other quantities used for comparison also agree well with those reported in N91. Fig. 3.3d shows, for example, the vertical flux convergence of the resolved turbulent kinetic energy, which is within the same range as the other models' data.

Finally I note that the CIMMS LES model simulations have been presented at a number of LES intercomparison workshops held as a part of the Global Energy and Water Cycle Experiment Cloud System Study (GCSS) Program. The predictions of our model fall into the same range as most of other participating LES models. The results of intercomparison are described by Moeng et al. (1996) and Bretherton et al. (1998).

3.2 Microphysical framework

a. Drop Spectrum Resolution and Method of Remapping

The cloud drop spectra in the CIMMS LES model are described by 29 bins with drop mass doubling every bin. The original and quite accurate formulation of the Berry and Reinhardt (1974b) method was applied to what may be called a "zero-dimensional" model, where drop size distribution was evolving in a closed air parcel due to drop coagulation process alone. The simple zero- and one-dimensional models alow one to use a higher drop resolution, with drop mass doubling every second or every third bin. Such resolution, however, is computationally prohibitive in a 3-D LES model. The aim of the sensitivity test described below is to evaluate the errors introduced in our model by comparing the results obtained with 29 bins with the double resolution using 57 bins in the same drop size range.

In addition, I tested the sensitivity of the results to the drop spectrum remapping

methods used in the condensation algorithm. The first method is the variational optimization (VO) scheme, employed in the current version of the models, while the second method is the Kovetz and Olund (1969) (KO) scheme. The latter, although preserving the total drop concentration and liquid water content, is known to be computationally diffusive (see, e.g. Ochs 1978).

The thermodynamic sounding for the sensitivity test was similar to the one used in the third GCSS (GEWEX Cloud Systems Studies) LES model intercomparison workshop held in Clermont-Ferrand in August 1996. The sounding was based on the ASTEX A209 flight measurements as described by Duynkerke et al (1995). The CCN concentration was specified so that the resulting cloud drop concentration would be sufficiently low (a few tens in a cubic centimeter) to allow for substantial drizzle rates during the course of each simulation. Heavy drizzle may be particularly sensitive to the differences in the drop spectra resulting from the differences in numerical methods and spectrum resolution.

Figure 3.4 shows the results of the sensitivity tests for parameters characterizing STBL thermodynamical state, turbulence fluxes, and microphysics structure. Each profile was obtained by averaging over the last hour of a 6-hour long simulation. The results clearly show that the simulations are quite sensitive to the method of spectrum remapping and rather insensitive to doubling of the spectrum resolution. We may, thus, conclude that the spectrum resolution based on 29 drop categories is quite adequate to model the drizzle processes in stratocumulus cloud layers. The KO method increases the surface drizzle rate by a factor of 5 (from 0.5 to 2.5 mm day^{-1}) compared to the VO method. This is explained by the fact that the KO method causes a large numerical spectrum broadening as evidenced by the relative spectrum dispersion profiles in Fig. 3.4g. The difference in drizzle rates eventually resulted in substantial differences in the STBL profiles, such as liquid water content, potential temperature, total water content, and the boundary layer height (Fig. 3.4).

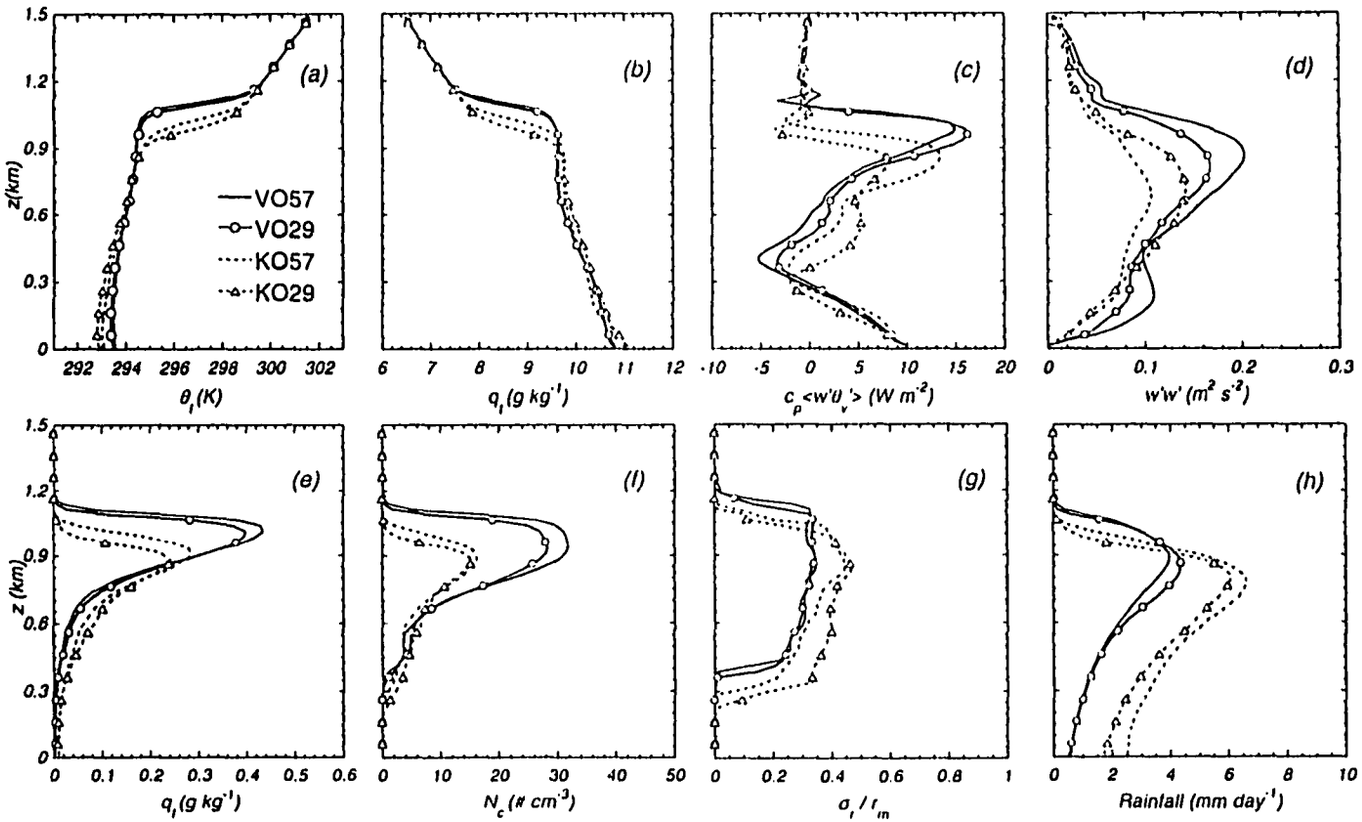

Figure 3.4 Vertical profiles of (a) virtual liquid water potential temperature, (b) total water content, (c) buoyancy flux, (d) vertical velocity variance, (e) liquid water content, (f) drop concentration, (g) relative drop spectrum dispersion, and (h) precipitation flux averaged over one hour interval after the 6th hour of simulation time. Different curves represent simulations with variational optimisation (VO) and conventional Kovetz and Olund (KO) methods of drop spectrum remapping after condensation calculation for 29 and 57 spectrum bins in the range from 1 to 645 μm.

b. Test of Coagulation Procedure

Recent studies suggest (e.g., see Montoya et al. 1995) that the Berry and Reinhardt (1974b) algorithm (referred further as BR74) used in our model for integration of the stochastic coalescence equation can result, under certain conditions, in significant errors in the liquid water content (LWC). It has to be noted, however, that the tests evaluating the errors of the BR74 algorithm are usually made using a closed parcel model which follows the evolution of the Gamma-distribution type spectrum due to drop collisions. As sedimentation and mixing is not allowed in this framework, the cloud drop mean radius grows unlimited with time and so does the error in LWC, especially when the spectrum shifts towards the right end of the size range. Obviously, in nature and in a more realistic dynamical model, the mean drop radius throughout the cloud stays within a certain size range affected by processes of mixing, sedimentation, evaporation, etc.

The test presented below was aimed at evaluation of the LWC error in our model. First, I calculate the LWC error as a function of the so-called "predominant" radius, introduced by BR74 and defined as $r_g = \left(\overline{r^6} / \overline{r^3}\right)^{1/3}$, where the bar represents the spectrum mean value. The r_g^3 may be equivalently defined as the radar reflectivity normalized by the LWC and represents a good measure of the large-drop tail of drop spectrum. As the latter evolves due to drop collisions, r_g grows and so do the errors in the LWC.

I assess the errors introduced by the BR74 coagulation procedure by applying it to the drop size spectra specified initially as a Gamma-distribution with LWC varied from 0.5 to 1.0 g/kg with an increment of 0.1 g/kg and drop concentration varied from 30 to 150 cm^{-3} with an increment of 10 cm^{-3}. The selected parameter range is characteristic for drizzling marine stratocumulus.

Figure 3.5a gives an example of the time evolution of one of the test spectra. As one can see, after a certain time, which depends mainly on the initial drop spectrum parameters, the drizzle mode rapidly increases and the spectrum shifts towards the maximum resolved drop size. For example, Fig. 3.5b demonstrates the time evolution of r_g for three cases, which differ by the initial liquid water content and drop concentration. From the plot of the cumulative error in the liquid water content (Fig. 3.5c), one can see that the coagulation procedure is very accurate in preserving the total water in all considered cases for values of r_g less than about 250 μm. It should be noted that the error begins to accumulate *before* the largest drops in the spectrum grow to the size of the largest resolved bin, so the problem cannot be corrected simply by increasing the drop size range. The main source of the error is evidently the use of the logarithmic scale for the drop size coordinate and the shift of the drop spectrum towards the lower size resolution near the right end of the spectrum range.

The most encouraging result, however, is that for drop spectra with r_g less than about 250 μm, the BR74 method results in almost negligible errors in LWC. Our analysis of the spectra produced in the simulations of the marine stratocumulus clouds shows that the typical values of r_g, even in cases of heavy drizzle, are unlikely to exceed the 250 μm threshold. This is clear from Fig. 3.5d that shows the probability to find a spectrum with r_g larger than a given value among 3400 spectra from a heavy drizzle simulation with the drizzle rate at the surface exceeding on average 2 mm day^{-1}. One can see that 99.9% of the spectra have r_g less than 250 μm and 90% of the spectra have r_g smaller than 100 μm. We may thus conclude that the BR74 method provides an accurate solution for the coagulation process in the case of the marine stratocumulus cloud layers.

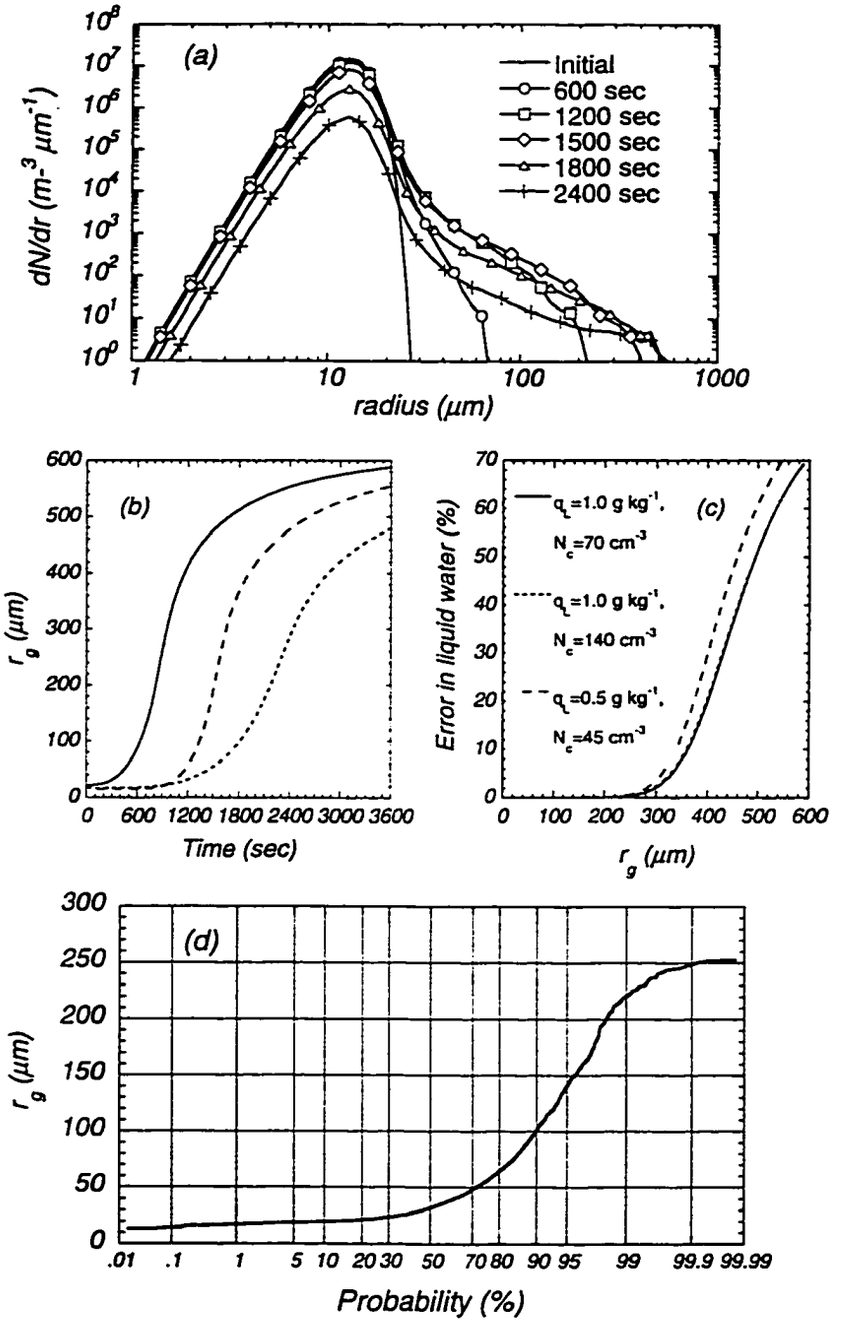

Figure 3.5 Test of the coagulation procedure: (a) example of the drop spectrum evolution; (b) time evolution of the predominant drop radius (see text for definition); (c) - the error in the liquid water content as a function of the predominant radius; (d) probability to find a spectrum with predominant radius exceeding a given value among the 3400 spectra from the heavy drizzle simulation. The initial spectra are specified as Gamma-distributions with the liquid water content and drop concentrations given in plot (c).

3.3 Summary and conclusion

In addition to the tests designed to assess the accuracy of a new LES dynamical framework, I have conducted various tests of the explicit microphysical module, two of which are discussed in this paper. In the standard model configuration, only 29 categories or bins cover the drop size range from 1 to 645 μm on the logarithmic scale. Two related problems were anticipated. First, the solutions obtained using the standard-drop-size-grid resolution would not converge to the solutions obtained with the doubled grid resolution. Second, the particular algorithm used for integration the stochastic coalescence integrals would lose the accuracy, especially when the drizzle mode of the drop size spectra are well developed.

We presented the results of the tests designed to address these problems. The results convince that the simulations are almost insensitive to a simple doubling of the drop size spectrum resolution in our model, implying that the standard number of drop size categories suffice to adequately resolve the cloud drop spectra in the model. I have also demonstrated that the results are very sensitive to the drop spectrum remapping technique used in semi-Lagrangian condensation calculations. A very accurate variational optimization method conserving four spectrum moments (Liu et al. 1997) supersedes the simple, but excessively diffusive, Kovetz and Olund (1969) algorithm.

The test of the drop coagulation procedure revealed that the method becomes inaccurate when the mass of the drizzle is dominated by the drops larger than about 250 μm. However, it was demonstrated that this limitation is rarely exceeded in typical simulations of the STBL even in the heavy drizzle cases. This is explained by the notion that for the typical liquid water paths observed in marine stratocumuli (less than a few hundred grams per squared meter) the drizzle drops fall out the relatively shallow cloud layer before having a chance to grow larger than several hundred microns. The turbulent

nature of the flow in the STBL can promote larger drizzle drop sizes. However, due to rather moderate values of the updraft velocities, which rarely exceed a few meters per second, as well as due to the updraft unsteadiness, the contribution of these larger drops to the total drizzle mass would not dominate.

Chapter 4

Comparison with Aircraft Observations

A typical LES model domain represents the horizontal scales in the order of a few kilometers. A typical aircraft measurement record represents the scales at least an order of magnitude larger. This disagreement imposes a major difficulty when one attempts to compare the LES model output with aircraft observations. In order to make a meaningful comparison, the observed STBL must at least be 1) driven mostly by the small-scale turbulence resolved by LES model; 2) close to horizontally homogeneous along the aircraft path.

The first condition is usually met in the convective STBL driven by the surface heat flux and the cloud top radiative cooling. The size of the convective thermals does not typically exceed several hundred meters, which is well resolved by LES models with several tens grid points in each domain direction and resolution 50 m. The second condition is the most difficult to meet, since the STBL characteristics can vary substantially over the scales of even several kilometers as the result of meso-scale cellular convection, for example (e.g., Rothermel and Agee 1980).

In order to minimize the effect of meso-scale variability on the mean STBL profiles, the aircraft data should be filtered, so that only the scales resolved by the LES model remain (e.g., Mann and Lenschow 1994). It is implied that the measurements are made within the STBL with similar characteristics along aircraft path. If, for example, one part of an aircraft leg is flown within a solid stratocumulus deck, and the other part is flown within a field of scattered cumuli, than, obviously, the analysis becomes too complicated. In addition, it is also important for the measurement period to be limited by a few hours, so that the effect of the synoptic-scale and diurnal variations on data is

reduced.

It is important to distinguish between the parameters that represent the predictive power of a model and the parameters that are external to the LES simulation and should be simply matched. In the simulations presented below, the following parameters have been considered external:

- the mean thermodynamic profiles of the liquid water potential temperature and total water mixing ratio, these are determined by the processes evolving on the temporal and spatial scales larger than the ones considered in an LES model;
- mean cloud base and top heights;
- downward radiation fluxes at the top of the model domain;
- surface heat and moisture fluxes;
- large-scale subsidence rate;
- mean drop concentration in the cloud.

In general, the specification of the cloud mean concentration is not required in the model, as it can be predicted based on the observed CCN spectrum. If the latter is known, then the CCN-cloud drop link can be studied in addition to the interactions between cloud turbulence, microphysics and radiation. However, both data sets used in the present study, unfortunately, did not include CCN measurements. We, therefore, used the CCN spectra shapes obtained from the ASTEX observations (e.g., Martin et al 1994). Although taken under similar conditions, the employed CCN spectra were not from the same data set and, therefore, cannot be used to verify the CCN-cloud drop link.

In this study, the CCN spectrum is scaled to match the observed *mean* cloud drop concentration. The local drop concentrations, however, varies in space in response to dynamical and radiative forcing. The vertical profile of drop concentration as well as the drop size spectrum itself at various locations are compared with observations.

4.1 Simulation of the North Sea STBL

Our first simulation is based on the analysis by Nicholls (1984) (further referred as N84) and Nicholls and Leighton (1986) (further referred as NL86) of the data collected over the North Sea during the UKMRF flight 526 on 22 July 1982. The same case has been studied by Ackerman et al. (1995) using a 1-D cloud model.

The observed boundary layer was rather well mixed with the geostrophic wind of 8.5 ms^{-1} and was topped by a stratocumulus cloud layer 300-400 m thick with intermittent drizzle. Since the measurements were collected around the local noon, the solar heating was an important factor in driving the boundary layer dynamics.

a. Initialization

The initial profiles of the *virtual* liquid water potential temperature and the total water mixing ratio were specified as

$$(\theta_l, q_T) = \begin{cases} (288.0, 8.2) & z < 762 \text{ m} \\ (288.0, 8.2) + (0.32, -0.088)(z - 762) & 762 \text{ m} < z < 787 \text{ m} \\ (296.0, 6.0) + (0.006, 0.0)(z - 787) & 787 \text{ m} < z \end{cases}$$

and the initial wind profile $(u, v) = (0., -8.5)$ m s^{-1} at all levels. The mean surface buoyancy flux rather than temperature was specified equal to 10 W m^{-2}. This value was obtained by extrapolating the virtual potential temperature flux profile, shown in N84, down to the surface. The surface moisture flux was calculated rather than specified.

The sea surface albedo was set to 0.05. The downward longwave and shortwave radiation fluxes at the top of the domain were fixed at the observed 276 W m^{-2} and 860 W m^{-2}, respectively. The test simulations showed that under such a condition the stratocumulus cloud layer would lose more than a half of its liquid water path in just 3

hours. (In reality the zenith angle changes rather significantly over 3 hour period, so the cloud layer depletion would not be so dramatic). In order to compensate for this effect, the cloud layer was initially thicker than the one in the observations. The goal was to match the mean temperature and the total moisture at the end of a simulation close to the measurements.

The simulations ran for 3 hours with 3-sec dynamical time step in a 40x40x50 grid-point domain with the resolution 75 m in horizontal and 25 m in vertical directions. Nucleation and condensation were computed with 0.1-sec time step. The mean vertical profiles from the model were averaged over the last 40 minutes of simulation. The data collected during the flight 526 falls into two subsets: the first, denoted by triangles in the following figures, represents measurements made during the slow descending sounding leg taken at 1100 GMT, while the second, denoted by circles, represents the horizontal run averages.

b. Mean profiles

Figure 4.1 shows that the mean temperature and total water profiles were matched rather satisfactory. The boundary layer developed a transitional weakly stable layer between 200 and 400 meters (Fig. 4.1a) as the result of solar heating of the cloud overlying cloud . This is in agreement with the analysis presented in N84, where it is found that a better agreement with the observed fluxes in the cloud layer is found when the mixed layer extends from 350 m to the cloud top rather than from the surface.

Formation of the weakly stable subcloud layer due to the solar heating suppresses the turbulent transport of moisture flux. This assists the moisture build-up near the surface (Fig. 4.1b), thus, decreasing the height of the lifting condensation level. As a result, the presence of the scud cumuli in the subcloud layer is a common feature of the

simulation with the cloud bases close to the observed 200 m, as evidenced by the profiles of the mean drop concentration (Fig. 4.1e). The latter is almost constant with height above the 600 as in observations, and gradually increases with height below, which is contrary to observations. However, the discrepancy might be due to horizontal variability of the STBL along the aircraft path. As we will see in the next simulation of the ASTEX A209 flight, the aerosol characteristics and therefore drop concentration can change rather dramatically on a scale of even several kilometers.

The magnitude of the precipitation rate agrees rather well with the measurements (Fig. 4.1f), although is slightly overpredicted/underpredicted in/below the cloud layer. However, it is not known how large the difference really is, since according to Turton and Nicholls (1987), the uncertainty in the drizzle flux measurements could be as large as 40%. One can also see that the contribution of the small cloud drops to the total precipitation rate dominates at the cloud top. The opposite is true at the cloud base, where the drizzle rate (drops larger than 25 μm) has a maximum.

The comparison between the simulated and observed longwave (LW) and shortwave (SW) radiation fluxes is shown in Figs. 4.1g and 4.1h, respectively. Note that due to the equipment fault, the upward longwave fluxes below the cloud layer were not measured. One can see that both the LW and SW fluxes are, in general, in good agreement with the measurements. The net gain of solar radiation by the cloud, reported in NL86, based on measured shortwave fluxes is 75 ± 39 W m^{-2}, which is in close agreement with 72 W m^{-2} gain obtained in our simulation. The observed net loss by the cloud due to the thermal radiation could not be estimated, because of the reported missing data. The NL86 estimate is 78 W m^{-2}, which is exactly in accord with the model. Thus, the observed net gain of radiation in the cloud region is -2 W m^{-2} in NL86 versus -6 W m^{-2} gain in the simulation. The agreement is very good; however, its significance should not be overestimated given the fact that the measurement uncertainty reported in N84 was as large as 20 W m^{-2}.

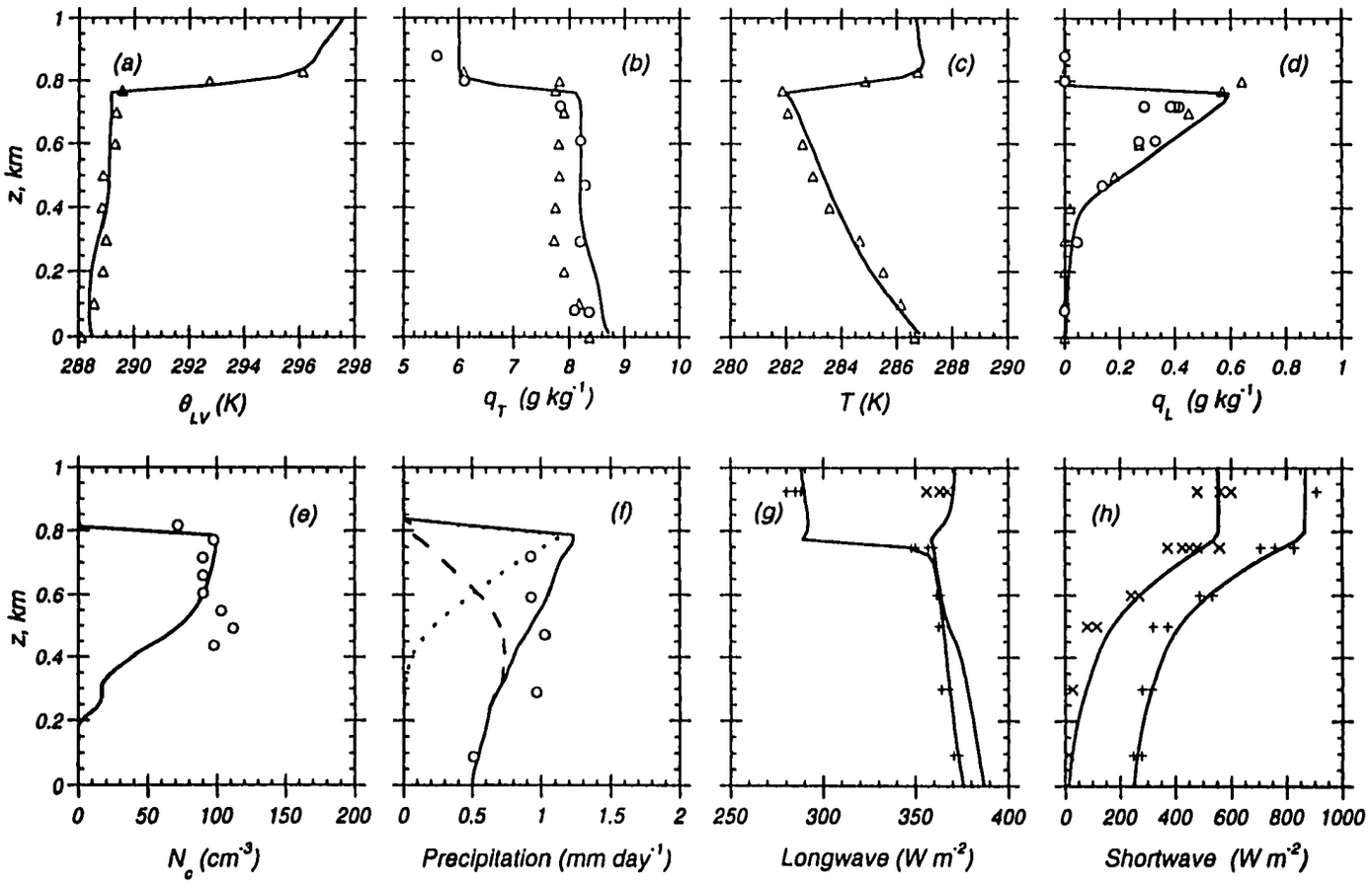

Figure4.1 Simulated (solid lines) versus observed during the UKMRF flight 526 (symbols) profiles of (a) virtual liquid water potential temperature, (b) total water content, (c) temperature, (d) liquid water content, (e) cloud drop concentration, (f) precipitation rate, (g) longwave and (h) shortwave upwelling (x) and downwelling (+) radiation fluxes. Observational data from Nicholls (1984) denote the horizontal leg averages (circles) and the 1100 GMT sounding (triangles). Dotted line in (f) represents the contribution of drops smaller then 25 μm, and the dashed line - contribution of larger drops.

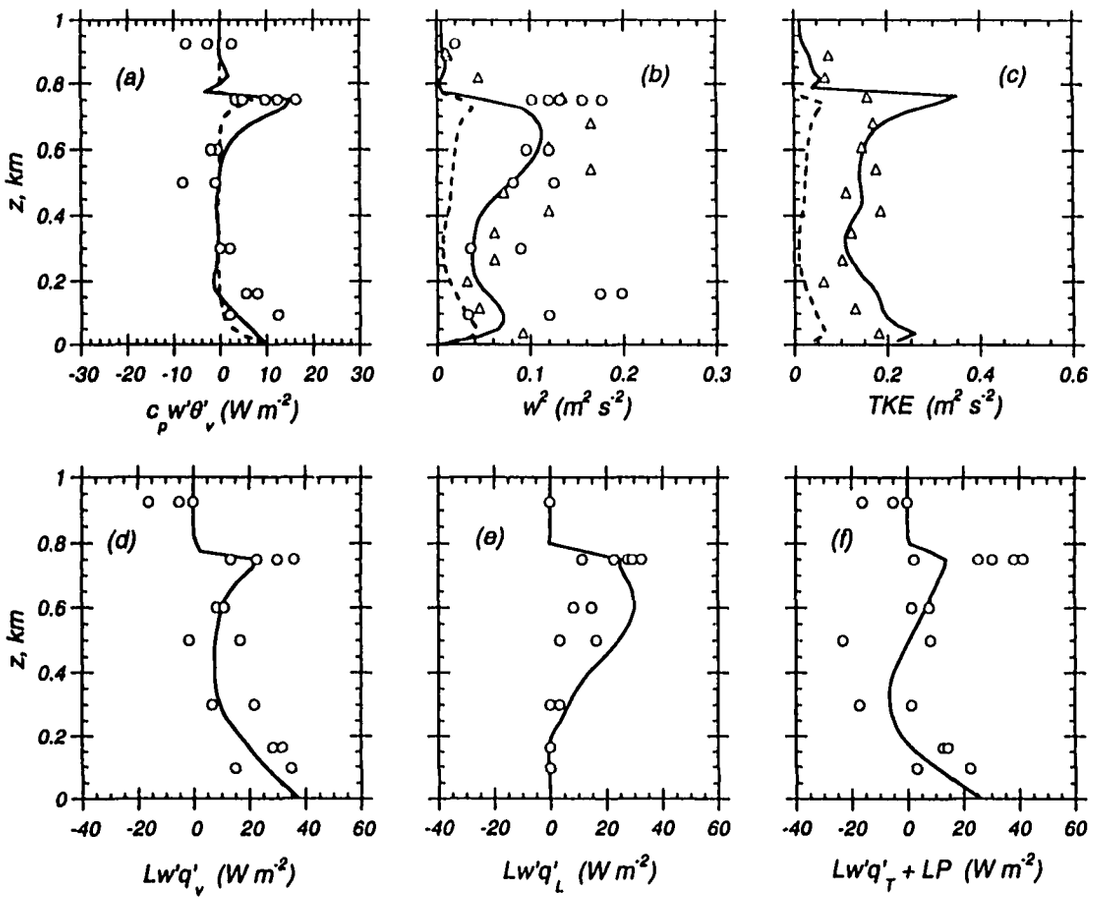

Figure 4.2 Simulated (solid lines) versus observed during the UKMRF flight 526 (symbols) profiles of (a) buoyancy flux, (b) vertical velocity variance, (c) turbulent kinetic energy, (d) moisture flux, (e) liquid water flux, and (f) sum of the turbulent total water flux and the precipitation flux. The observations are from Nicholls (1984). The dashed lines in (a)-(c) denote the SGS contribution to the model results.

c. Turbulence

The vertical flux of the virtual potential temperature or the buoyancy flux agrees rather well with N84 (Fig. 4.2a). Due to strong solar heating of the cloud and formation of the weakly stable subcloud layer, the buoyancy flux is suppressed in the lower half of the cloud. In the upper half, however, the buoyancy is still generated by strong longwave cooling concentrated in a shallow layer at the cloud top. Since the buoyancy flux is a main source of turbulence in the convective STBL, its suppression results in a rather low turbulence intensity, as evidenced by the vertical profiles of the vertical velocity variance (Fig. 4.2b) and the turbulent kinetic energy (Fig. 4.2c). One can see that, in general, the agreement between the measurements and the simulation is satisfactory. Even though the model tends to underestimate the vertical velocity variance in the cloud layer, qualitatively it follows the observations. Two distinct maxima near the surface and in the upper half of the cloud present another indication of the STBL decoupled structure.

The fluxes of the water substances are shown in Fig. 4.2d-4.2f. They generally agree well with the measurements, with the exception of the cloud top, where the fluxes are underestimated. In the subcloud region, the negative slope of the moisture turbulent flux (Fig. 4.2d) and the total water flux (Fig. 4.2f), which is a sum of the turbulent and precipitation fluxes, results in the moisture accumulation. In the cloud layer, on the other hand, the corresponding slope is positive indicating the total water depletion due to the cloud top entrainment and removal by drizzle. Note that the total water flux becomes negative in the subcloud layer indicating that the amount of moisture penetrating from the surface region to the Sc, mostly in the scud cumuli, is smaller than the amount of water leaving the Sc layer in the from of drizzle.

d. Drop Size Spectra

The simulated mean drop size spectra at four different levels are shown in Figure 4.3. In general, one can see that the model reasonably well reproduces both the position and magnitude of maximum of the drop spectrum. The agreement is the best in the lower part of the cloud (480 m). At the cloud top (730 m), the most apparent discrepancy is underproduction of number of drops smaller than 6 μm. The possible explanation for the "flat" spectrum near the cloud top is insufficient resolution in our simulation to adequately resolve the small-scale entrainment and mixing near the cloud top. Current models also assume that the entrained air in an individual grid cell mixes with the surrounding cloudy air almost instantaneously by the SGS diffusion. In reality, it may take quite significant time to mix a cell volume of 75x75x25 m^3. As a result, the cloud near its top may contain localized packets of entrained air (Moeng et al. 1995). The mixing occurring near the edges of the dry air packets causes the drops to evaporate, which is seen in aircraft records as increased concentration of the smallest drops. The fact that the model better reproduces the observed concentration of the smallest drops in the lower half of the cloud, where the entrained parcels are more likely to be already mixed out, indirectly supports the offered explanation. Although a similar discrepancy is found in the simulation of the ASTEX A209 flight presented below, the generality of the "flat" spectra is not clear, as in many cases the cloud drop spectra near the cloud top are quite narrow (Gerber, personal communication, 1996).

It has to be noted that underestimation of the smallest drop concentration at the cloud top by the model would not seriously affect such cloud parameters, as the drop effective radius, which is the ratio of the spectrum third and the second moments, or the liquid water content, which is proportional to the third moment. The relative contribution of drops with radius smaller than 6 μm to the second and to the third moment is several orders of magnitude smaller than the contribution from drops with

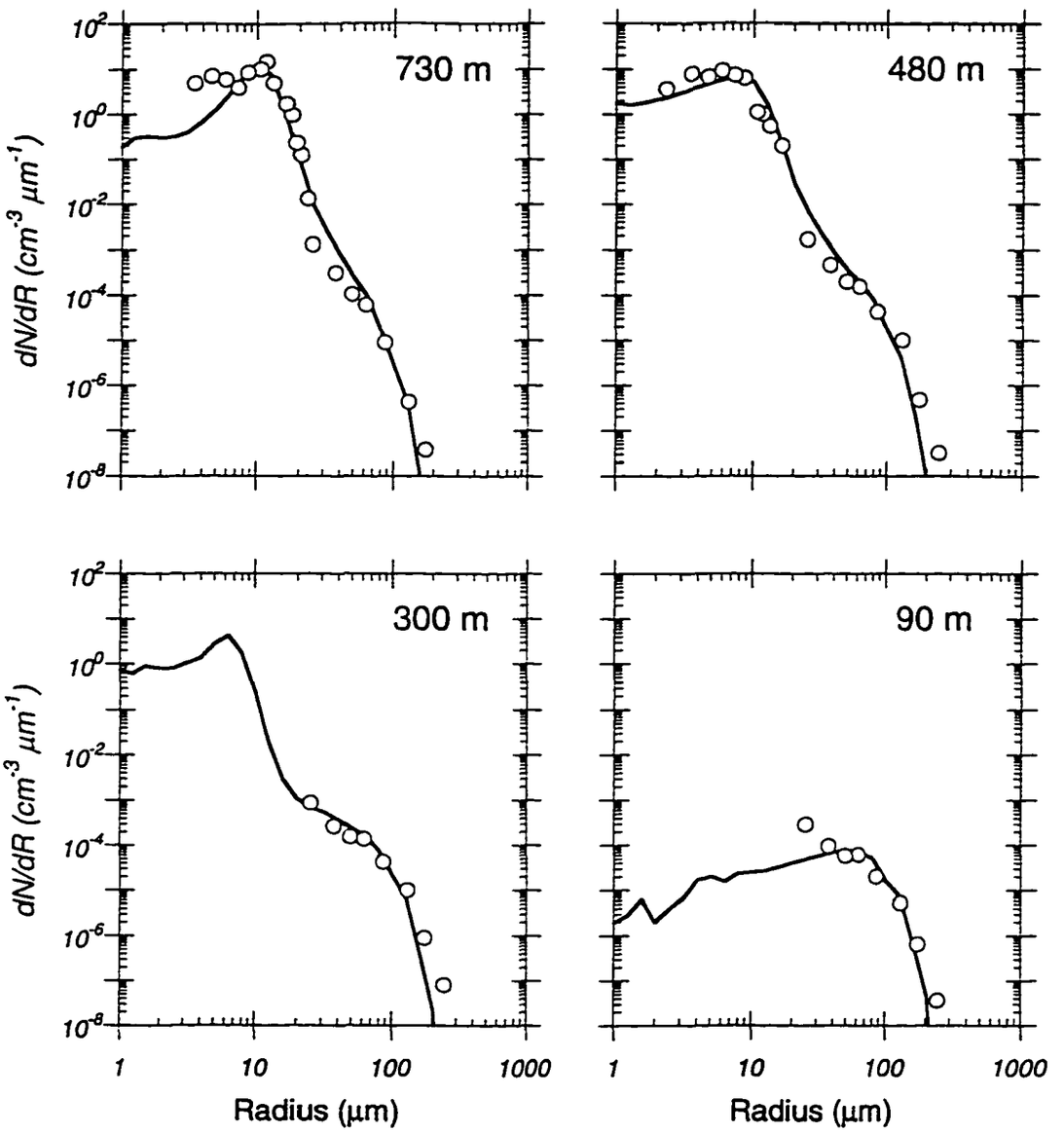

Figure 4.3 Horizontally averaged drop size spectra at four different levels of simulated STBL. Circles represent the data from Nicholls (1984).

sizes around 10 μm, which also contribute most to the total drop concentration at the cloud top. Underestimation of the concentration of drops smaller than 6 μm does not affect the drizzle initiation and evolution in the model due to the very low values of the drop collision efficiencies in this size range as shown in section 5.2.

The number of drops with radii between 20 and 50 μm is higher in the model, which may be a result of instrument error, as the Optical Array Probe (OAP) systematically undercounted drops in this size range (N84). The drizzle part of the spectra is rather well reproduced in the cloud layer, the subcloud region and near the surface (300 and 90 m). The drops smaller than 25 μm in radius, present in significant concentrations at the 300 m level are sampled in the *scud* cumuli below the main stratocumulus cloud deck.

4.2 Simulation of the East-Central Atlantic STBL

The A209 flight measurements were collected from 23:03 to 05:55 UTC on 12-13 June 1992 by the U.K. Meteorological Research Flight (UKMRF) C-130 aircraft during the ASTEX Lagrangian I Experiment (Bretherton and Pincus, 1995). The comprehensive analysis of turbulent, thermodynamical and microphysical characteristics of this flight is presented by Duynkerke et al. (1995) (further referred as DZJ95). The observed STBL was well mixed with the stratocumulus base at 250-300 m and the capping inversion at 700-800 m. The temperature jump across the inversion was about 2-3 K with the corresponding total water jump about -1 g kg^{-1}. The observed mean liquid water content at the cloud top was 0.6 g kg^{-1}.

Figure 4.4 depicts the horizontal and time-height aircraft path diagrams during the A209 flight. The aircraft made three stacks of horizontal 60-km legs flown crosswind below, within and above a thick stratocumulus cloud deck. Each stack was preceded and

followed by a sounding. Because of the night flight limitations, the lowest legs were flown at only about 160 m above the surface. The highest legs were flown at about 100 m above the cloud top. The aircraft was drifting along the mean wind, so that the measurements were taken approximately within the same air mass.

Our analysis of the data revealed a well-pronounced variability in aerosol characteristics, and, consequently, in cloud microphysics along the aircraft legs, as shown in Figure 4.5. Here the FSSP (Forward Scattering Spectrometer Probe) drop concentration near the top of the Sc layer and the PCASP (Passive Cavity Aerosol Spectrometer Probe) aerosol concentration at 160 m above the ocean surface are plotted. One can see that along each leg the aircraft has been crossing a region of a locally cleaner air-mass about 20 km wide along the legs as evidenced by the decreased aerosol and, consequently, cloud drop concentrations. Because the aircraft was following the mean wind in the STBL, this locally cleaner air-mass was present in all horizontal leg data (see Fig. 4.4a).

Our focus will be on a more polluted air mass, with the mean drop concentration about 150 cm^{-3}. Therefore, the FSSP measurements taken inside the clean air mass were excluded from the data analysis in this study to make a consistent comparison with the model predictions. The strong variability in aerosol and microphysical characteristics along the flight legs had a rather insignificant effect on the STBL turbulent and thermodynamical characteristics, including the liquid water content, making conditional sampling of these data unnecessary.

The analysis of all four A209 soundings revealed that the dew point temperature just around the cloud base, where the water vapor is close to saturation, seems to be systematically underestimated by about 1 K. For a given temperature and pressure range, this discrepancy corresponds to about 0.6 - 0.8 g kg^{-1} error in the water vapor mixing ratio. In order to correct the problem, I assumed that the error is indeed systematic and added 1 K to all dew point measurements outside the cloud. Inside the

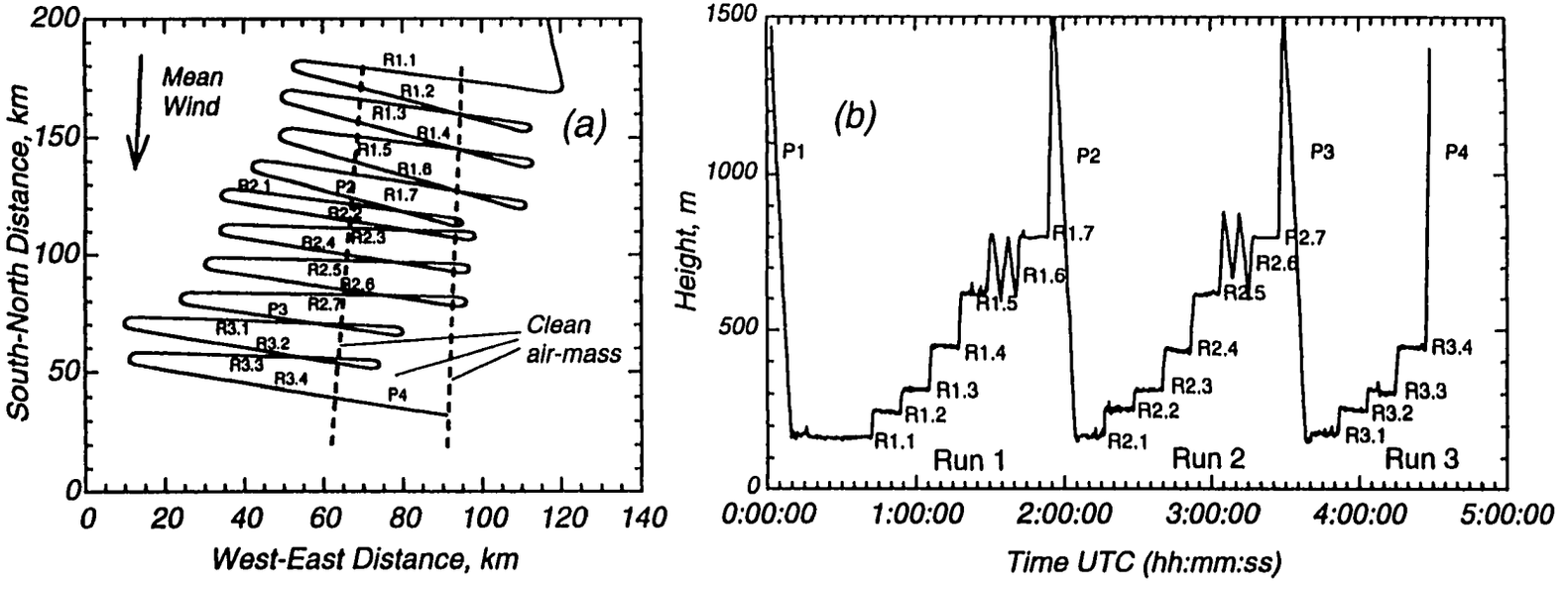

Figure 4.4 (a) Horizontal and (b) time-height aircraft path during the ASTEX A209 flight. The boundaries of the locally cleaner air-mass are shown by the dashed lines.

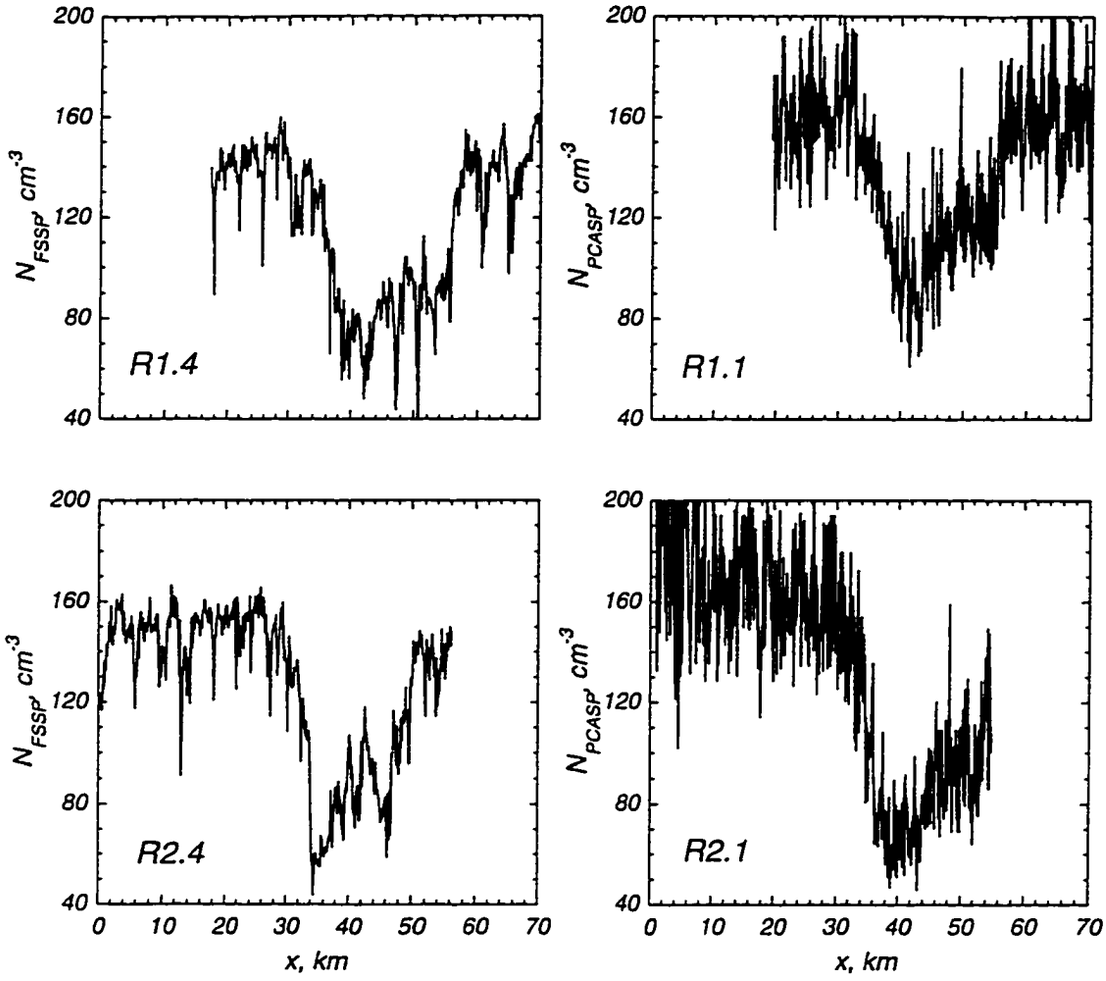

Figure 4.5 Measurements of FSSP drop concentration at 450 m within the Sc cloud (left panels) and PCASP aerosol concentration at 160 m above the surface (right panels) from the ASTEX flight A209.

cloud, the absolute temperature was used for the moisture content retrieval instead of the dew point temperature, since, as it is known, the latter is not reliably measured in the presence of the liquid water.

a. Initialization

The initial soundings were designed such that the simulated vertical profiles of the temperature, total water content, and cloud base height averaged over the last simulation hour matched as close as possible the observations. The initial profiles of liquid water potential temperature and the total moisture were following

$$(\theta_l, q_T) = \begin{cases} (288.0,\ 10.8) & z < 612.5\text{m} \\ (288.0,\ 10.8) + (0.2,\ -0.044)\,(z - 612.5) & 612.5\text{m} < z < 637.5\text{m} \\ (293.0,\ 9.7) + (0.006,\ -0.0028)\,(z - 637.5) & 637.5\text{m} < z \end{cases}$$

and the initial wind profile $(u, v) = (0., -10)$ m s^{-1} at all levels. The background pressure was calculated assuming the hydrostatic balance with surface value 1030 mb. Since the lowest flight level was 160 m, the surface sensible, latent and momentum fluxes used as the boundary conditions were rather difficult to retrieve. The values for the fluxes were set to 10 W m^{-2}, 25 W m^{-2}, and 0.09 m^2 s^{-2}, respectively, similar to values used in the third GCSS LES Intercomparison Workshop based on the corresponding profiles in DJZ96.

The downward longwave radiation flux at the top of the model domain was fixed at the observed 302 W m^{-2} as it depends mostly on the distribution of thermodynamical parameters aloft rather than on the fields within the domain. The SST needed for calculation of the surface upward longwave radiation flux was estimated from the Monin-Obukhov similarity theory given the value of the surface heat flux. The large-scale subsidence divergence was fixed at 5×10^{-6}s^{-1} in accord with the large-scale vertical

velocity profiles given in DZJ95. Similar to the case specifications for the 3rd GCSS LES Intercomparison Workshop, the spectrum of CCN, composed of ammonium bisulfate, was approximated by the log-normal distribution with the median radius of 0.1 μm, standard deviation of 1.5 μm, and the total concentration of 180 cm^{-3}.

The numerical domain size was 3 x 3 x 1.25 km with the resolution $(\Delta x, \Delta y, \Delta z)$ = (75m, 75m, 25m). The convection was initialized by applying the random temperature perturbations with the amplitude 0.1 K 100 m below the inversion. The simulation ran for 3 hours with the time step 3 sec. The results represent the time-averages over the last simulation hour.

As it was mentioned above, the aircraft flew three stacks of horizontal legs during the flight. Thus, the flight data points fall into three categories each represented by a symbol. The filled circles represent the Run 1 (see Fig. 4.4), the open circles - Run 2, and finally the triangles correspond to the Run 3. The boundary layer height was growing during the observation period; therefore, only the first stack was used as a benchmark for matching the boundary layer height. However, as it will be seen further, the internal boundary layer parameters did not change dramatically during the 4-hour observation period, so all the legs were useful for comparison. In figures, where it was possible, each data point is accompanied by the "error bar" representing the standard deviation.

b. Mean profiles

Figure 4.6 shows that the simulated profiles and the measurements agree very well, although the predicted liquid water profile is slightly higher than one in the observations. The discrepancy may be attributed to the fact that the liquid water was estimated from

the drop size spectra measured by the FSSP, which tends to systematically underestimate the cloud water content (e.g., Gerber, 1996). Both the simulation and observations agree that the liquid water is below the moist-adiabatic values due to the entrainment of warmer and dryer air at the cloud top.

The standard deviation below the inversion is relatively small for all shown profiles suggesting that the boundary layer was rather horizontally uniform along the flight legs (except the microphysics, see above). A large variance in the inversion runs is due to the aircraft skimming the cloud top (see legs R1.6, 2.6 in Fig. 4.4b). The analysis suggests that most of the shown variance (except the drop concentration) is associated with the meso-scale variability of the boundary layer rather the with the small-scale convection, as further shown.

The agreement of the mean cloud drop concentration N_c (Fig. 4.6e) with the observations is excellent. One can see that N_c rather rapidly increases with height up to the middle of the cloud, and then stays nearly constant. The observed standard deviation of N_c along the legs is in the range 20-30 cm^{-3} (except the inversion legs). Similar values are predicted by the model suggesting that most of the variance is due to the small-scale convection rather than the meso-scale variability. It is interesting that the observations of N_c are very consistent for different aircraft runs indicating that the cloud microphysical properties were rather robust during the observation period.

The profiles of the upward and downward longwave radiation are also in excellent agreement with the observations. One can see that due to very large absorption of the longwave radiation by the liquid water, the upper half of the cloud, where most of liquid water is concentrated, behaves like a blackbody, so that both upward and downward fluxes are in almost perfect balance. The cloud top radiates upward more radiation than it absorbs by about 60-70 Wm^{-2} implying a strong radiative cooling. The lower half of the cloud is slightly cooler than the underlying surface; therefore, it absorbs more energy

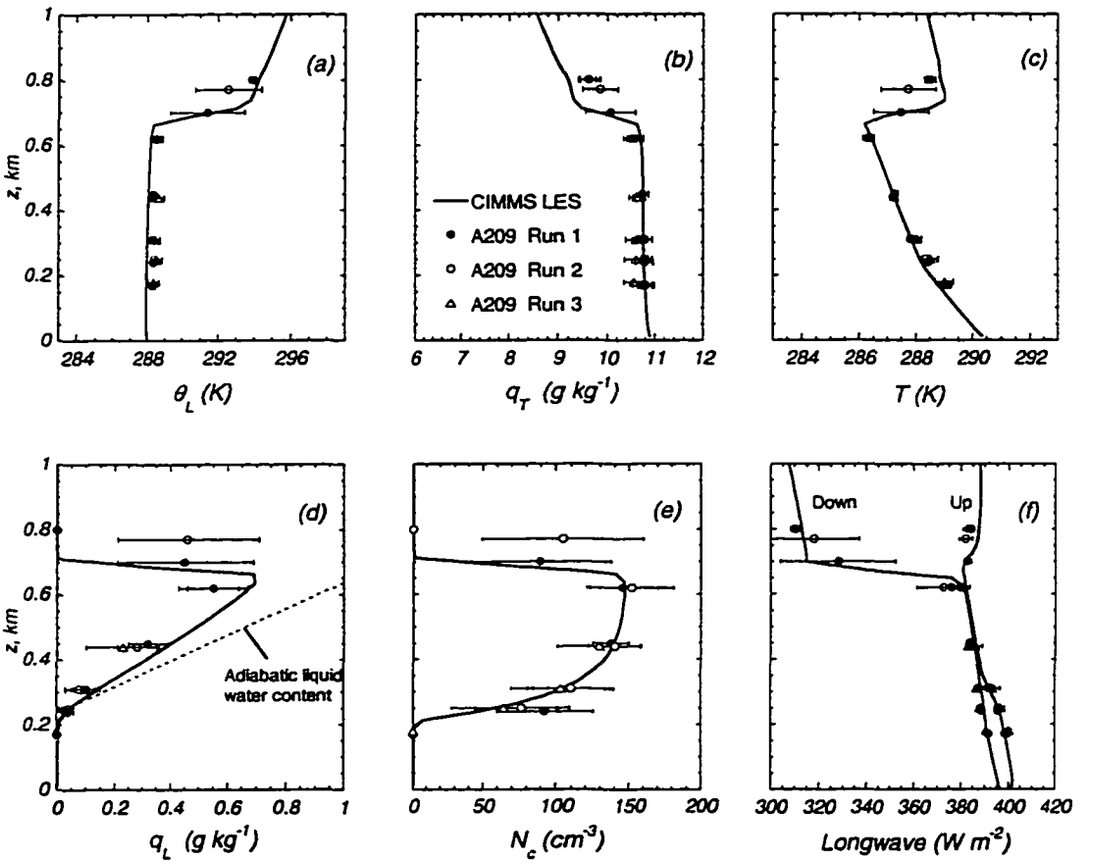

Figure 4.6 Simulated (solid lines) versus observed during the ASTEX flight A209 (symbols) profiles of (a) liquid water potential temperature, (b) total water mixing ratio, (c) absolute temperature, (d) liquid water content, (e) drop concentration, and (f) longwave radiation fluxes. The standard deviation of the observed values is indicated by bars.

than it emits implying the net warming, which, however, is much smaller than the cloud top cooling. Both effects - cooling at the top and warming at the bottom - maintain the convective instability of the cloud layer and are the main source of convective energy in marine stratocumuli.

c. Turbulence

The observed quantities in Fig. 4.6 were calculated from the raw aircraft data, and, therefore, represent the fluctuations in all scales smaller than 60 km. In contrast, the LES model resolves the scales of turbulence smaller than the model domain. Therefore, in order to compare the turbulent characteristics, the measurements should be filtered to eliminate the contribution of the scales larger than resolved by the model. In this analysis I used the high-pass version of the Lanczos filter (Duchon 1979) with the cut-off length 3.1 km as in DJZ95.

The predicted profiles of the root-mean-variance (RMS) of θ_l, q_T and q_L are in very good agreement with observations (Figs.4.7a-c). While the RMS of θ_l and q_T stay approximately constant throughout the STBL depth, the RMS of q_L monotonically increases upwards from the cloud base. At the cloud top, the magnitude of fluctuations increases sharply due to cloud top entrainment. Note that the contribution from the aircraft skimming through the inversion is dramatically decreased in the filtered data, since the horizontal scale of corresponding aircraft vertical oscillations was much larger than 3 km filter cut-off length.

The variances of the east-west $\overline{u'^2}$ (Fig. 4.7d) and the north-south $\overline{v'^2}$ (Fig. 4.7e) wind components have two distinct local maxima: one near the surface and the other at the cloud top. The latter is commonly explained by the increased horizontal velocity

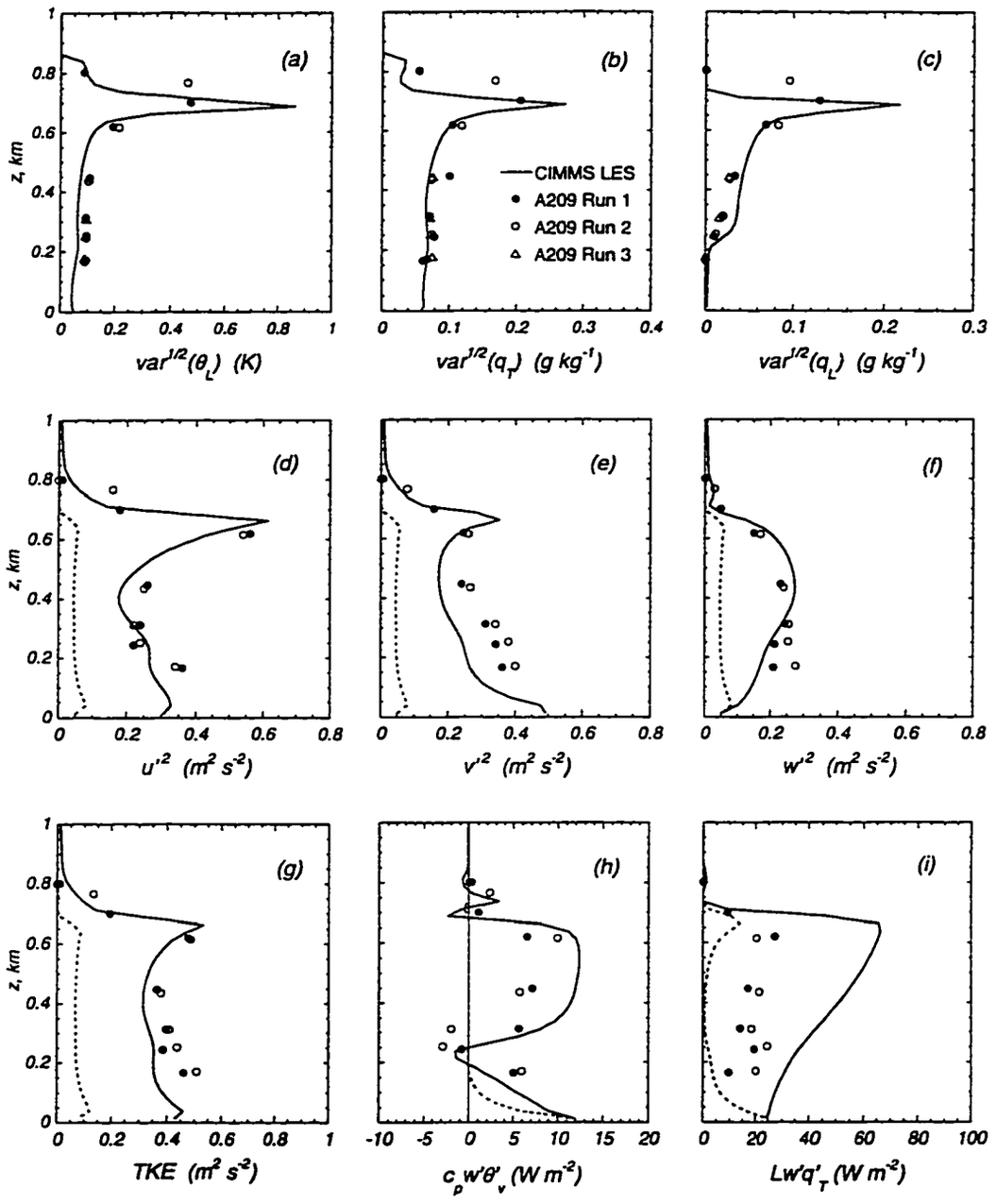

Figure 4.7 Simulated (solid lines) versus observed during the ASTEX flight A209 (symbols) profiles: RMS of (a) liquid water potential temperature, (b) total water mixing ratio, and (c) liquid water content; velocity variance of (d) east-west, (e) north-south, and (f) vertical wind components; profiles of (g) turbulent kinetic energy, (h) buoyancy and (i) total water fluxes. The measurements are obtained applying high-pass filter to the raw data with the cut-off length 3.1 km. Dashed lines show the SGS contribution to the model results. Data for plots (d)-(i) are taken from Duynkerke et al. (1995).

fluctuations caused by the outflow from the updrafts striking the inversion. It is interesting to note that the east-west velocity variance has a significantly larger maximum near the cloud top than the north-west component. The analysis of simulated three-dimensional flow suggests that the rather strong north-south wind shear near the surface led to the roll-like convection pattern with the preferred north-south orientation. As the result, the outflow from the updrafts at the cloud top is more likely to spread in the west-east direction, which explains the larger values of $\overline{u'^2}$ and smaller values for $\overline{v'^2}$. The local minima are predicted at about $0.6h$ and $0.7h$, respectively, where h is the height of the inversion layer. Despite a slight underestimation of $\overline{v'^2}$, the overall agreement between the model and observations is quite satisfactory.

The vertical velocity variance $\overline{w'^2}$ (Fig. 4.7e) is predicted to have a maximum at $0.6h$, which approximately corresponds to the height of the minimum in the horizontal velocity variance profiles. The magnitude of $\overline{w'^2}$ compares rather well with the measurements, although it is appears to be slightly underestimated below 300 m. The observed $\overline{w'^2}$ calculated for different runs agree very well with each other above 300 m, although they differ somewhat more for the two lowest legs. It is possible that higher values of turbulence at levels below the cloud base in observations were due to the rather strong wind shear near the surface; the underestimation of turbulence in the model was, most likely, due to the insufficient spatial resolution near the lower boundary.

The turbulent kinetic energy (TKE) (Fig. 4.7g) agrees well with observations, although it appears to be slightly underestimated mostly because of the smaller $\overline{v'^2}$ contribution than in observations. Consistent with observations, the TKE gradually decreases with height up to about $0.7h$ and then sharply increases to its maximum at the cloud top.

The mean buoyancy flux (Fig. 4.7a) qualitatively agrees well with the observations. It decreases gradually from its surface value becoming slightly negative near the cloud base, possibly as a result of weak stabilization due to the drizzle evaporation. Inside the cloud, $\overline{w'\theta_v'}$ becomes positive and stays approximately constant up to the cloud top. In general, the model predicts larger values of $\overline{w'\theta_v'}$ than the values calculated from the measurements. The largest discrepancy between the model output and the observed fluxes is found for the total water flux $\overline{w'q_T'}$ (Fig. 4.7b), which is exaggerated by a factor of 2.5. I do not have a solid explanation for this discrepancy.

d. Drop Size Spectra

Figure 4.8 shows the mean cloud drop size spectra at three different levels - the cloud top, middle, and bottom. In general, the simulated spectra are in a reasonably good agreement with the observations both for the small cloud drops, sampled by the FSSP, and for the drizzle drops, sampled by the 2-Dimensional Cloud probe (2DC). The apparent discrepancy for the drops larger than about 15 μm may be due to the systematic error in the upper drop size range of the FSSP, as noted in DJZ96. As in the previous simulation, the model seems to underestimate the concentration of the smallest drops near the cloud top, although the discrepancy is not as large. The explanation for this discrepancy has been offered in the section describing the results the UKMRF 526 flight simulation.

The drizzle part of the drop spectra is in excellent agreement with the observations for the droplets smaller than about 150 μm, which represent the bulk mass of the drizzle water. The model underestimates the number of larger drops, although still within the sharply increased data variance range.

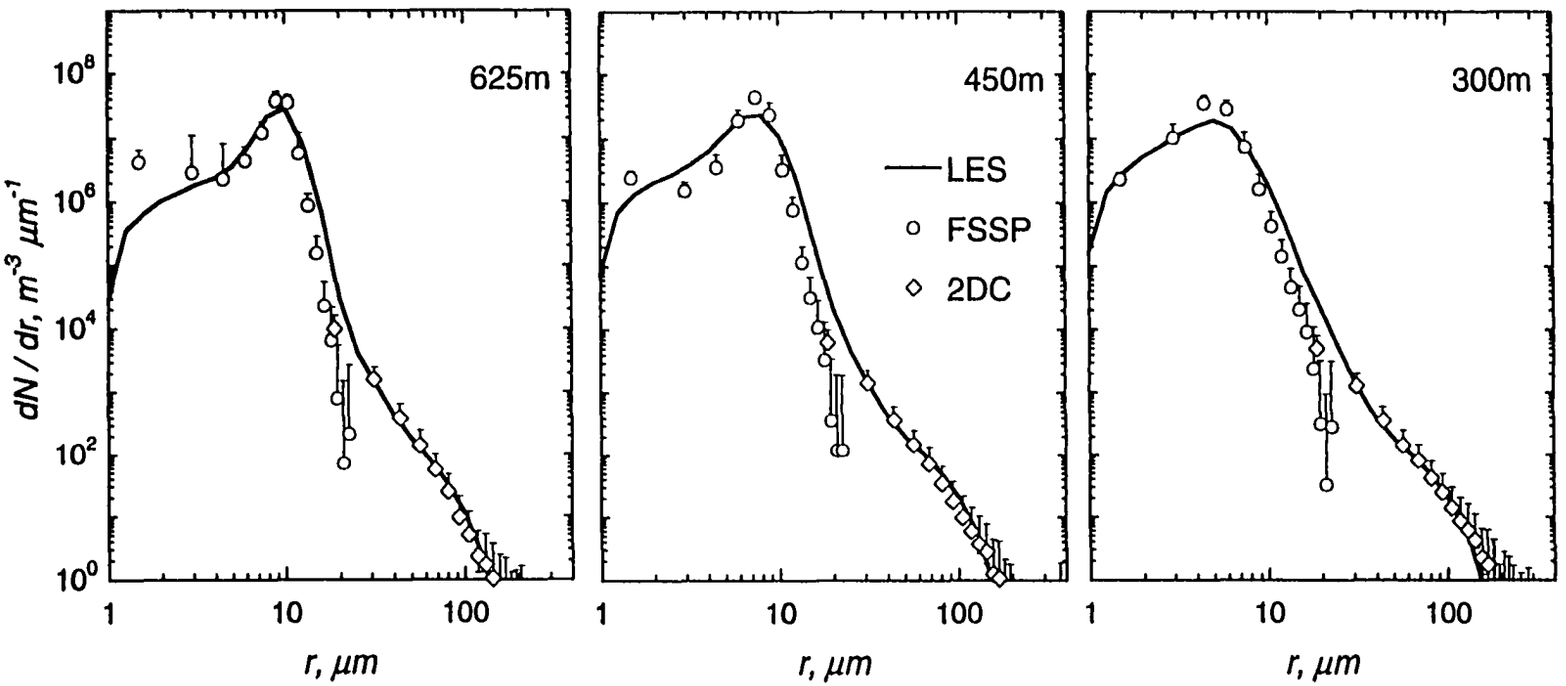

Figure 4.8 Simulated (solid lines) versus measured during the ASTEX Flight A209 (symbols) drop size spectra at three different levels in stratocumulus cloud layer. The standard deviation of the observed values is indicated by bars.

4.3 Summary and conclusion

Besides the opportunity to study the drizzle processes in the STBL in a comprehensive way, the main goal that we pursued employing the explicit microphysics in the CIMMS LES model is to design new bulk microphysical parameterizations for LES and other models applied to the STBL problems. This goal, however, is difficult to achieve without a confidence that the model results are relevant to reality, or, in other words, without thorough testing the model numerics and evaluating its output against the observational evidence. This study represents the first major step in this direction.

In order to evaluate the realism of the model, a direct comparison of the model predictions with the aircraft observations of the STBL was carried out. The first case was based on the UKMRF flight 526 measurements collected over the North Sea on 22 July 1982; the second case corresponds to the ASTEX flight A209 flown on 12-13 June 1992. Since the aircraft records in the first case was not available, the comparison was based on the analysis presented by Nicholls (1984) and Nicholls and Leighton (1986). In contrast, the second case provided us with an opportunity to assess the horizontal variability of the STBL, which allowed us to compliment the lag-average values of various quantities with their variance along the measurement legs. In addition, the analysis revealed a presence of a locally cleaner air-mass with significantly modified microphysics in all aircraft legs, which was carefully accounted for when comparing the model microphysical prediction with the observations.

The model was able to satisfactory reproduce most of the observed characteristics such as turbulent fluxes and variances of various fields, intensity and vertical distribution of the turbulent kinetic energy, upward and downward radiation fluxes. The main discrepancy here was a notable overestimation of the buoyancy flux and especially the total water turbulent flux in the A209 simulation. The latter

discrepancy was somewhat puzzling given the fact that the turbulent kinetic energy and the vertical velocity variance, as well as the variances of the total water and liquid water agreed very well with observations. I was not able to offer an explanation of this discrepancy and think that more studies are warranted to pinpoint its cause.

The model rather accurately reproduced the integral parameters of the mean drop size spectra at different height within and below the cloud, as well as the spectrum mode and shape. However, at the cloud top, the model systematically underestimates the concentration of the drops smaller than 3-6 μm. I think that this can be explained by the inherit inability of the LES models with the spatial resolution in the order of 25-50 m to accurately resolve the mixing of the entrained parcels with the cloudy environment. The drizzle part of the spectra was agreed reasonably well with the observations in both cases. The main discrepancy is that the model tends to underestimate the concentration of the drizzle droplets larger than 150 μm. Although their contribution to the total drizzle mass is relatively small in the considered cases, it is, nonetheless, interesting to know if it is an indication of the need to revise the collision efficiencies, or simply the need to improve the accuracy of the spectrum measurements near the large-drop end of the spectrum.

Chapter 5

Bulk Microphysics

5.1 General Approach

As was mentioned in Chapter 1, the cloud drop population can be characterized by the drop *size distribution function* (DSD) $f(x_i, r, t)$, which describes how many drops can be found in the size range from r to $r + dr$ in a given point with coordinates x_i at the time moment t. In general, the equation describing the evolution of the cloud drop population of the can be written as

$$\frac{\partial f}{\partial t} = -\frac{\partial}{\partial x_i}(u_i - \delta_{i3} v(r)) f - \frac{\partial}{\partial r}(\dot{r} f) + \left(\frac{\partial f}{\partial t}\right)_{proc} + \frac{\partial}{\partial x_i} \nu \frac{\partial f}{\partial x_i} \qquad (5.1)$$

The first term in the right-hand side represents the advective transport including the effect of the gravitational fall-out with terminal velocity $v(r)$. The second term describes the transformation of the DSD due to condensation/evaporation of droplets with the rate $\dot{r}$, which is a function of water vapor supersaturation, drop radius, temperature and other factors. The third term represents the transformation of the DSD due to the sinks/sources associated with the CCN activation, complete drop evaporation, drop collision, coalescence and break-up processes. The last term represents diffusion.

Since the numerical cloud models use a finite set of spatially separated grid points, the equations are formulated for the quantities that are effectively averaged over the grid interval. This represents a difficult problem for the explicit microphysical

approach, since the equation (5.1) should also be averaged. Analogous to the Reynolds averaging of the momentum-equation, a few new terms would then appear. The meaning behind these terms is that the drop concentration and supersaturation, and, therefore, the droplet growth by condensation, can randomly fluctuate within a sample volume from one point to another as a result of eddy break-up and mixing. The equation that takes into account this effect on the evolution of an averaged DSD is called the *equation of stochastic condensation* (e.g., see Stepanov 1976). The mathematics behind the stochastic approach is rather complicated, so that, to my knowledge, it was not yet applied in any cloud-resolving model.

In order to avoid complication associated with the non-deterministic behavior of the supersaturation on the sub-grid scales, it is usually assumed that the supersaturation field is uniform within a grid-mash volume. In order for this assumption to work, the size of eddies that are responsible for the new drop activation should be larger than the grid spacing. It may be the case for the LES of the convective STBL, where the individual rising thermals are typically well resolved. The assumption might not be generally true for the grid spacings larger than several hundred meters, as in some fine resolution meso-scale models. However, even in LES models, the supersaturation fluctuations within an individual grid mesh may be an important factor for the DSD broadening in cloud (e.g., Levin and Sedunov 1966, Stepanov 1976), which may affect the precipitation initialization processes. The rapid increase in computer power may provide opportunity for the direct test of this hypothesis in the future.

In many applications the knowledge of the quantities derived from the DSD such as liquid water content, drop concentration, drizzle amount, precipitation rates and some others may suffice to approximate the interaction among the dynamics, microphysics and radiation. In other words, the knowledge of a few moments of the DSD is sometimes more practically needed than the DSD itself. One may derive the general equation for the nth DSD moment defined as

$$M_n(x_i,t)=\int_{r_1}^{r_2} r^n f(x_i,r,t)dr \tag{5.2}$$

by multiplying the equation (5.1) by r^n and performing the integration, assuming a simplified formula for the rate of change of cloud drop radius due to condensation

$$\dot{r}=\frac{G(T,p)S}{r} \tag{5.3}$$

where $G(T,p)$ is a known function of the temperature and pressure only. Implying that f vanishes when $r = r_1$ and $r=r_2$ the equation is the following:

$$\frac{\partial M_n}{\partial t}=-\frac{\partial}{\partial x_i}(u_i-\delta_{i3}V_n)M_n+nGSM_{n-2}+\left(\frac{\partial M_n}{\partial t}\right)_{proc}+\frac{\partial}{\partial x_i}K\frac{\partial M_n}{\partial x_i} \tag{5.4}$$

where the weighted terminal velocity for the *n*th moment is defined as

$$V_n(x_i,t)=M_n^{-1}\int_{r_1}^{r_2} r^n v(r)f(x_i,r,t)dr \tag{5.5}$$

For the drizzle part of the drop spectrum in the range from 40 to 600 μm, the drop terminal velocities are well approximated by $v(r)=kr$, and therefore $V_n = k\ M_{n+1}/M_n$.

We can see that even in a greatly simplified case when the source/sink term in the right-hand side of (5.4) is ignored, the evolution of the *n*th moment may depend on several other moments. The equations for these moments would bring even more additional moments to play and so on. The problem is somewhat similar to the problem of turbulence closure. (Theoretically, if we are able to predict all moments of the DSD, the system might be as fully described as it is by the DSD, although I don't know if there is a proof of this statement).

The are many ways of designing the bulk microphysics based on a limited set of the DSD moments. In principle, there is probably no need to artificially divide the

liquid water into the cloud and drizzle water as it is done in the Kessler-type approach (Kogan, personal communication). Instead, the cloud water may be well characterized by the low moments of the DSD, say, smaller than the fourth moment, and the drizzle water can be characterized by the higher moments. This is because the higher the moment of DSD, the more significant the contribution of larger drops even though their concentration might be much smaller than the concentration of the smaller drops. The sink/source terms associated with such processes as coagulation and sedimentation could be obtained exploring the parameter space of the moments using the explicit microphysics and then storing the result as the look-up tables. Exploration of this approach to the bulk microphysics is left for the future.

5.2 Current Approach

In principle, in order to close the system of equations for the LES dynamical framework (2.1)-(2.8), one needs to know only the liquid water content to calculate the buoyancy terms in the right-hand sides of the vertical momentum and SGS TKE equations, and the precipitation flux. The radiation fluxes may also be calculated with sufficient accuracy, especially for the long-wave part of the spectrum, using the liquid water content and some mean size of the cloud drop population. Therefore, if a bulk model were able to reproduce these two key *macro*physical parameters similar to the explicit model, then the dynamical response of the system to the cloud microphysics would be similar.

The Kessler-type approach, based on partitioning the liquid water into cloud and precipitable water, was adopted as a base model for the proposed bulk microphysics scheme, because of its simplicity and transparency of the physical principles behind it. The legitimacy of the partitioning is illustrated by Fig. 5.1, where the mass gain by

drops of different sizes during one time step of coagulation procedure is shown. Each curve represents LES simulation of light or heavy drizzle. For each simulation, several thousand spectra with liquid water content larger than 0.1 g kg^{-1} were sampled from locations all over the simulated cloud. The coagulation procedure was run for each spectrum to calculate the mass gain/loss in each spectral bin. The results were averaged for each simulation and presented in Figure 5.1 as a function of drop radius. One can see that the drops with sizes less than approximately 15-20 μm are always being collected, while, in contrast, the larger drops are gaining their mass by collecting smaller drops. Therefore, in the case of stratocumulus clouds, the threshold drop radius separating the cloud water from the drizzle water can be estimated to be around 25 μm. Note that the drops smaller than about 6 μm are neither collecting nor collected because of negligibly small coagulation kernel in this size range.

Next step is to select the set of the parameters that would suffice to approximate the processes leading to the liquid water contents and drizzle rates simulated by the explicit microphysics. The cloud and drizzle liquid water contents are the first candidates. The drizzle initiation process is sensitive to the characteristic size of the droplet population, because of the local properties of the coagulation kernel in the 7-20 μm drop size range. For a given liquid water content, the characteristic size is determined by the drop concentration. The latter is generally a function of an ambient CCN count and intensity of the updrafts at the cloud base (e.g., see Pruppacher and Klett 1997). Thus, the proposed bulk scheme should be able to predict the cloud drop concentration based on the total CCN and supersaturation fields. In addition, it would be desirable to predict the total mean radius, defined as a product of the drop spectrum mean radius and the drop concentration. This parameter is optional and allows one to estimate the relative drop spectrum dispersion, which may be important in radiation calculations. The choice of three cloud water parameters is similar to one proposed by Clark (1974a,b).

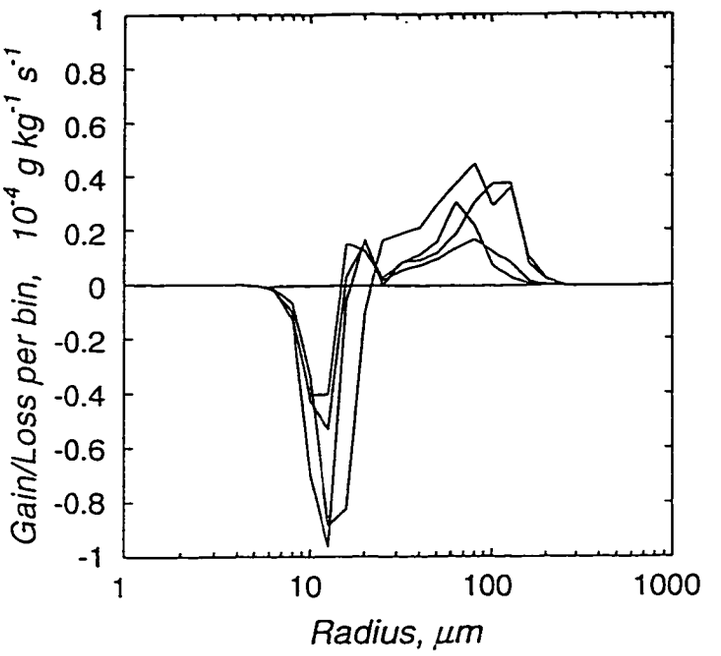

Figure 5.1 The mass gain/loss by different drop size bins due to coagulation from four different simulations (see text for explanation).

The drizzle precipitation rate is a product of the drizzle water content and the average fall velocity. For a given drizzle water content, the latter depends on the characteristic mean size of the drizzle drop population. The evaporation rates also depend on the drizzle drop sizes. Therefore, the drizzle drop concentration should also be predicted.

Thus, the predicted parameters include the total CCN count n, cloud water content q_c, cloud drop concentration N_c and total mean radius R_c, drizzle water content q_r and drizzle drop concentration N_r. The conservation equations for these parameters are as follows

$$\frac{\partial n}{\partial t} = -\frac{\partial u_i n}{\partial x_i} - \left(\frac{\partial N_c}{\partial t}\right)_{activ} + \left(\frac{\partial N_c}{\partial t}\right)_{evap} + \frac{\partial}{\partial x_i} K \frac{\partial n}{\partial x_i} \tag{5.6}$$

$$\frac{\partial q_c}{\partial t} = -\frac{\partial u_i q_c}{\partial x_i} + \frac{\partial V_{q_c} q_c}{\partial z} + \left(\frac{\partial q_c}{\partial t}\right)_{cond} - \left(\frac{\partial q_r}{\partial t}\right)_{auto} - \left(\frac{\partial q_r}{\partial t}\right)_{accr} + \frac{\partial}{\partial x_i} K \frac{\partial q_c}{\partial x_i} \tag{5.7}$$

$$\frac{\partial N_c}{\partial t} = -\frac{\partial u_i N_c}{\partial x_i} + \frac{\partial V_N N_c}{\partial z} + \left(\frac{\partial N_c}{\partial t}\right)_{activ} - \left(\frac{\partial N_c}{\partial t}\right)_{accr} - \left(\frac{\partial N_c}{\partial t}\right)_{auto} + \frac{\partial}{\partial x_i} K \frac{\partial N_c}{\partial x_i} \tag{5.8}$$

$$\frac{\partial R_c}{\partial t} = -\frac{\partial u_i R_c}{\partial x_i} + \frac{\partial V_R R_c}{\partial z} + \left(\frac{\partial R_c}{\partial t}\right)_{cond} + \frac{\partial}{\partial x_i} K \frac{\partial R_c}{\partial x_i} \tag{5.9}$$

$$\frac{\partial q_r}{\partial t} = -\frac{\partial u_i q_r}{\partial x_i} + \frac{\partial V_{q_r} q_r}{\partial z} + \left(\frac{\partial q_r}{\partial t}\right)_{cond} + \left(\frac{\partial q_r}{\partial t}\right)_{auto} + \left(\frac{\partial q_r}{\partial t}\right)_{accr} + \frac{\partial}{\partial x_i} K \frac{\partial q_r}{\partial x_i} \tag{5.10}$$

$$\frac{\partial N_r}{\partial t} = -\frac{\partial u_i N_r}{\partial x_i} + \frac{\partial V_{N_r} N_r}{\partial z} - \left(\frac{\partial N_r}{\partial t}\right)_{evap} + \left(\frac{\partial N_r}{\partial t}\right)_{auto} + \frac{\partial}{\partial x_i} K \frac{\partial N_r}{\partial x_i} \tag{5.11}$$

The subscripts *cond/evap* represent the rate of change of a quantity due to condensation/evaporation; *activ* refers to the effect of CCN activation; *auto/accr*

represent the cloud water conversion to drizzle and accretion of cloud water by drizzle, respectively. In order to close the system (5.6)-(5.11), the sink/source terms in the right-hand sides are parameterized in terms of the predicted variables themselves as described below.

5.3 Parameterization of Cloud water and CCN

a. CCN Activation/Regeneration

As it is known from the cloud physics, the drop concentration is mostly determined by the maximum supersaturation in a rising parcel at the cloud base, and on the CCN activation spectrum. This spectrum defines how many CCN particles become cloud drops for a given value of the supersaturation. In the explicit microphysical model, the CCN spectrum is initiated by prescribing particle concentration in each CCN size bin, for example, in accord with observations. A particular CCN bin is activated when the supersaturation reaches its critical value for this bin, which depends on dry CCN size and its chemistry.

In the proposed bulk microphysics, the CCN activation spectrum is prescribed by the power function of the supersaturation (e.g., Pruppacher and Klett 1997, p. 288)

$$n(\vec{x},t) = n_{1\%} S_{thr}^{k} \qquad (5.12)$$

where S_{thr} is the threshold supersaturation above which no more CCN are allowed to activate. Now, assuming that the parameter k is fixed, the following simple algorithm for CCN activation is proposed.

First, the total CCN count in a grid box is evaluated as if all drops evaporated: $n_{total} = n + N_c$. Then, a new value of $n_{1\%}$ is calculated as

$$n_{1\%} = \frac{(n + N_c)}{S_{thr}^k} \tag{5.13}$$

Then, the supersaturation needed for activation of the current drop concentration is expressed using (5.12) as

$$S_{activ} = (N_c / n_{1\%})^{1/k} \tag{5.14}$$

If the supersaturation on the current time step S exceeds S_{activ}, then the additional cloud drops should activate. Summarizing the algorithm, a number of cloud drops activated on the current time step is given by following expression:

$$\Delta N_c = -\Delta n = \max\left\{0, (n + N_c)\left(\frac{\max(0, S)}{S_{thr}}\right)^k - N_c\right\} \tag{5.15}$$

This number should be added to cloud drop concentration N_c and subtracted from CCN concentration n.

The drop concentration is not the only parameter that is modified during the CCN activation. The cloud water content and the total mean radius should be modified accordingly. In the explicit microphysics the process of CCN activation is implemented as following. The dynamical time step, which is usually several seconds in the LES model, is refined in the iteration loop with smaller time step (usually in the order of 0.1 s) to increase the overall accuracy of calculation of condensation for the CCN and the smallest drops. The CCN grow by condensation and when they reach or grow beyond the size of the smallest drop bin, they become drops and are remapped into the cloud drop spectrum. In the bulk model, we parameterize this process. A simple assumption will be made that all new activated drops have the same size. Even though we found that this size can depend on the magnitude of the local updraft, the discrepancy in prediction of drop concentration between the explicit and the bulk models is usually small (10-20%). Thus, the following simple expressions are adopted:

$$\Delta R_c = r_{act} \Delta N_c \tag{5.16}$$

$$\Delta q_c = \frac{4\pi\rho_w}{3\rho_a} r_{act}^3 \Delta N_c \qquad (5.17)$$

where r_{act} = 1 μm.

b. Condensation/Evaporation

The general form of the rate of change of cloud water parameters due to condensation/ evaporation can be derived as

$$\left(\frac{\partial q_c}{\partial t}\right)_{cond} = \frac{4\pi G(T,P)\rho_w}{\rho_a} S\int_0^\infty rf(r)dr = \frac{4\pi G(T,P)\rho_w}{\rho_a} SR_c \qquad (5.18)$$

$$\left(\frac{\partial R_c}{\partial t}\right)_{cond} = G(T,P)S\int_0^\infty \frac{f(r)}{r}dr = G(T,P)SN_c\overline{\left(\frac{1}{r}\right)} \qquad (5.19)$$

The drop concentration does not obviously change during condensation without activation of new CCN. It can change, however, during evaporation. For simplicity, the drop concentration is not allowed to change during the evaporation until the cloud water content reaches some minimum value (in current version of the bulk model it is set to 10^{-3} g/kg). Then, a grid volume is assumed cloud free. After the drop evaporation, the drop concentration is added to the CCN total count in a given grid point. Since the drop concentration can decrease as a result of accretion by the drizzle, the CCN count would gradually decrease (in the absence of source of the CCN) approximating the process of CCN washout by the drizzle.

In order to close the system (5.18)-(5.19), we have to parameterize the mean inverse drop radius in (5.19). We will express this parameter through the mean volume radius

$$r_{vc} = \overline{(r^3)}^{1/3} = \left(\frac{4\pi\rho_w}{\rho_a}\right)^{-1/3} q_c^{1/3} N_c^{-1/3} \tag{5.20}$$

assuming that the cloud drop spectrum can be approximated by the gamma-distribution (2.16) (Clark 1974a). Then, it can be shown that

$$\overline{\left(\frac{1}{r}\right)} = \frac{(\gamma+1)N_c}{\gamma R_c} \tag{5.21}$$

where

$$\gamma = \frac{5 - 2P + \sqrt{8P+1}}{2P-2}; \qquad P \equiv \frac{3\rho_a q_c N_c^2}{4\pi\rho_w R_c^3} \tag{5.22}$$

Note that the parameter γ is uniquely related to the drop spectrum relative dispersion:

$$\sigma_r = \sqrt{\frac{\overline{r^2}}{\overline{r}^2} - 1} = (\gamma+1)^{-1/2} \tag{5.23}$$

c. Sedimentation

In general the cloud water content, drop concentration and total mean volume radius have different mean terminal velocities, according to (5.5). However, since the terminal velocities of the cloud drops do not normally exceed a few centimeters per second, we will not differentiate between them and simply specify them as

$$V_{q_c} = V_{N_c} = V_{R_c} = 1.3\, k_1\, r_{vc}^2 \tag{5.24}$$

where k_1 is the Stokes constant 1.19 x 10^6 cm^{-1} s^{-1}.

5.4 Parameterization of drizzle

a. Method

The unknown sink/source terms associated with the drizzle part of the parameterization are expressed in terms of the predicted variables themselves assuming that the rate of change of some variable χ is given as a function of variables ϕ and in a general form

$$\left(\frac{\partial \chi}{\partial t}\right)_{proc} = c\phi^a \psi^b \tag{5.25}$$

Here a, b, and c are some free parameters of the parameterization determined using the drop spectra simulated by the explicit microphysical model. The database included the spectra from four three-dimensional simulations in a wide range of cloud water content and drop concentration (Fig. 5.2a). For comparison, Fig. 5.2b also shows the liquid water content and drop concentration for all flights during the 1995 Southern Hemisphere Marine Aerosol Characterization Experiment (ACE-1). The spectra were randomly selected from the database to evenly cover the range of the corresponding drop mean volume radius from 7 to 19 μm. The total number of spectra used in the analysis was about a hundred thousands.

Given the drop size spectra, the rate of change of χ and the variables ϕ and can directly calculated for each sample spectrum using the explicit microphysical model. Then the parameters a, b, and c in (5.25) are evaluated applying the least square method to minimize the cost function

$$S(a,b,c) = \sum_i \left[\left(\frac{\partial \chi}{\partial t}\right)_i - c\phi_i^a \psi_i^b\right]^2 \tag{5.26}$$

where the summation is done over the number of the sample spectra. Since the left-

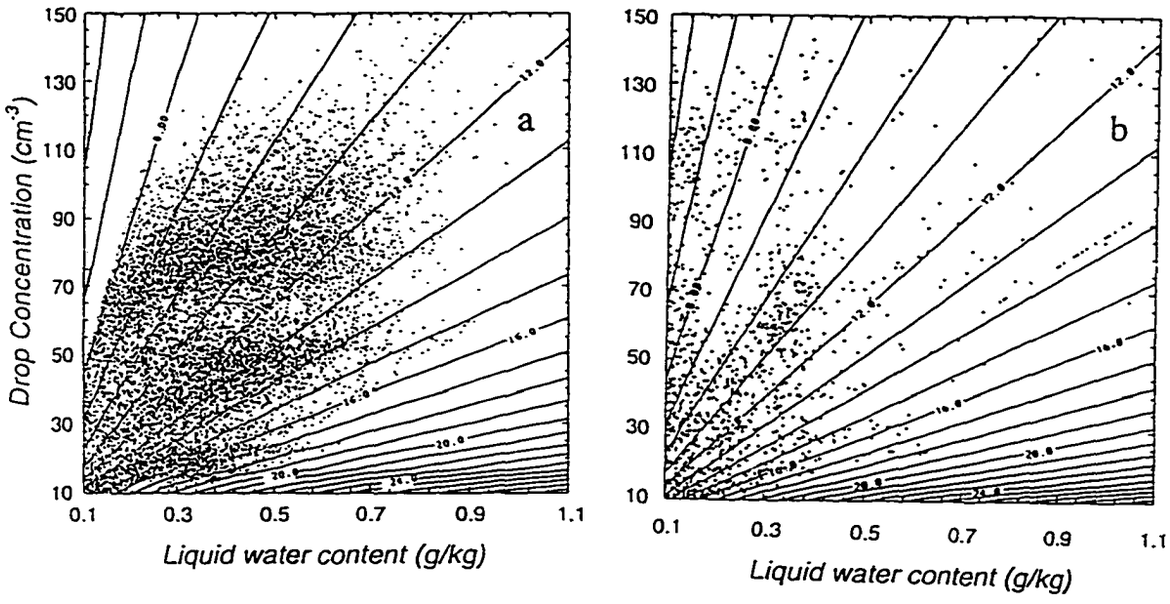

Fig. 5.2 (a) - A scatter-plot of the parameter space used to evaluate the coefficients for the bulk parameterization of drizzle. Each data point represents the liquid water content and drop concentration calculated from an individual drop-size spectrum simulated by the explicit microphysics version of the model; (b) - similar to (a), but each data point represents the liquid water content and drop concentration averaged over an individual flight lag in stratocumulus clouds for all aircraft flights during the first phase of the Aerosol Characterization Experiment (ACE-1) in November-December 1995.

hand side of (5.25) can change several orders of magnitude as, for example, in the case of the autoconversion rate, it is more appropriate to use the logarithm-based definition of the cost-function

$$S(a,b,c)=\sum_i\left[log\left(\frac{\partial\chi}{\partial t}\right)_i-log\left(c\phi_i^a\psi_i^b\right)\right]^2 \tag{5.27}$$

or, equivalently

$$S(a,b,c)=\sum_i\left[\ln c+a\log\phi_i+b\log\psi_i-log\left(\frac{\partial\chi}{\partial t}\right)_i\right]^2 \tag{5.28}$$

Then, the problem is reduced to a simple linear regression. The condition for the local minimum is given by

$$\frac{\partial S}{\partial a}=\frac{\partial S}{\partial b}=\frac{\partial S}{\partial c}=0 \tag{5.29}$$

yielding a system of three linear algebraic equations with three unknowns. In cases when some of the parameters *a*, *b*, and *c* can be chosen *a-priori*, the method is applied to the unknown parameter(s) only.

b. Condensation/Evaporation

The rate of change of drizzle water content due to condensation/evaporation can be derived similar to the cloud water as

$$\left(\frac{\partial q_r}{\partial t}\right)_{cond}=3C_{evap}G(T,P)\left(\frac{4\pi\rho_w}{\rho_a}\right)^{2/3}q_r^{1/3}N_r^{2/3}S \tag{5.30}$$

where C_{evap} is equal to the ratio of the mean volume radius to the mean geometric radius. For example, the theoretical value for the Marshall-Palmer spectrum is 0.55. From the analysis of condensation in the explicit model, we found that in most of the

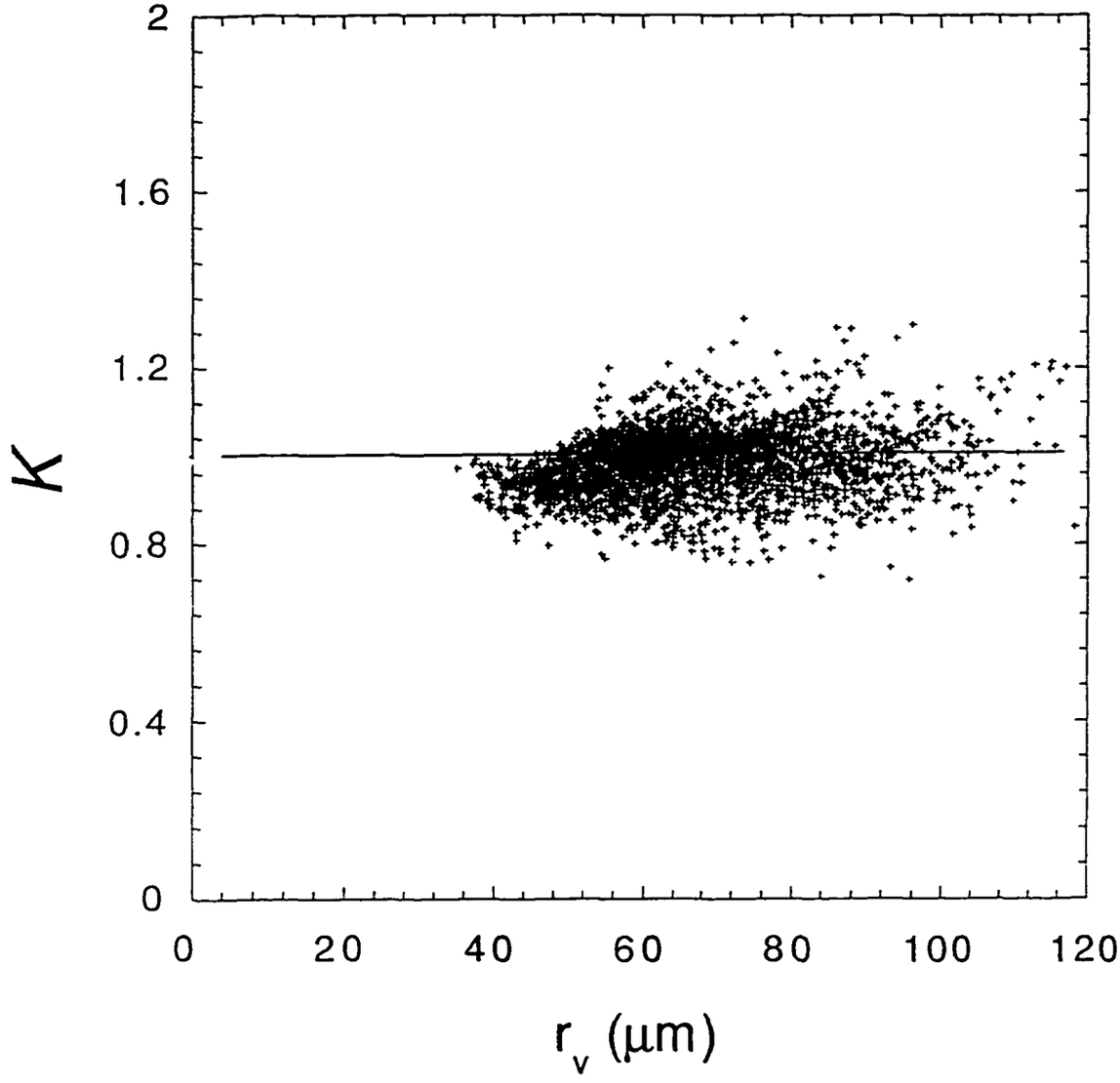

Fig. 5.3 A scatter plot of k in the expression for drizzle drop evaporation (4.32) versus the drizzle mean volume radius obtained from the explicit microphysical model.

cases C_{evap} = 0.86. The condensation, obviously, does not change the drizzle drop concentration. This is not true, however, for the drizzle evaporation. In this case, it is assumed that the change of the drizzle concentration is related to the correspondent change of the drizzle water content during one time step as

$$\left(\frac{\Delta N_r}{N_r}\right)_{evap} = \left(\frac{\Delta q_r}{q_r}\right)^K_{evap} \tag{5.31}$$

where k is some parameter. The corresponding scatter-plot obtained from the explicit microphysical model is shown in Fig. 5.3. One can assume that k can be set to 1.

c. Autoconversion

The autoconversion of cloud water into drizzle is the most challenging part of the parameterization. Some expressions for the autoconversion rate, which have been used so far in bulk microphysical models, are reviewed in Chapter 1. Since the autoconversion, by definition, is the process of drizzle initiation via coalescence between small cloud drops, it is assumed here that it only depends on cloud water variables such as the cloud water content and the cloud drop concentration. The autoconversion rate itself was calculated from the simulated drop spectra as the total mass change per unit time in the 25 μm threshold bin as a result of coalescence of small cloud drops. Following a method of linear regression, the general form for autoconversion rate is sought in the form (5.25) with variables χ, ϕ and corresponding to variables q_r, q_c and N_c, respectively. Applying the least square method, the autoconversion rate is approximated as

$$\left(\frac{\partial q_r}{\partial t}\right)_{auto} = 1350 q_c^{2.47} N_c^{-1.79} \tag{5.32}$$

with q_c given in gg^{-1} and N_c in cm^{-3}. It was found, however, that the autoconversion rate expresses also rather well as a function of the drop mean volume radius only

$$\left(\frac{\partial q_r}{\partial t}\right)_{auto} = 1.26x10^{-15} r_{vc}^{5.67} \tag{5.33}$$

with r_{vc} given in μm. The scatter-plot showing the correlation between the autoconversion rates given by (5.32)-(5.33) and the ones calculated from the explicit model are shown in Fig. 5.4a and 5.4b. One can see that the majority of points are within a factor of two from the perfect correlation line. Taking into account the fact that the autoconversion rates vary almost three orders of magnitude with the mean volume radius varying from 7 to 19 μm, the approximation is quite satisfactory. As an example of the fact that the expressions (5.32)-(5.33) do offer an improvement compared to the previously used expressions, I applied the regression analysis to find the best fit for the expression (1.8), proposed by Chen and Cotton (1987) and which can be rewritten in terms of q_c and N_c. The result is

$$\left(\frac{\partial q_r}{\partial t}\right)_{auto} = 2.2 q_c^{4/3} N_c^{-1/3} \tag{5.34}$$

The corresponding scatter-plot is shown in Fig. 5.4c, where, as one can see, the scatter is much bigger than one for the expressions (5.32)-(5.33). Besides, the coefficient 2.2 in front of the expression in (5.34) is more than order of magnitude smaller than the coefficient calculated from (1.8), which is about 30. This agrees well with independent estimate by Baker (1993) who pointed out that the expression (1.8) seems to overestimate the autoconversion rates by from one to two orders of magnitude in the case of spectra measured in the trade-wind cumuli.

The source of the drizzle drop concentration due to the autoconversion is defined by simply assuming that all the new drizzle drops have a size equal to the

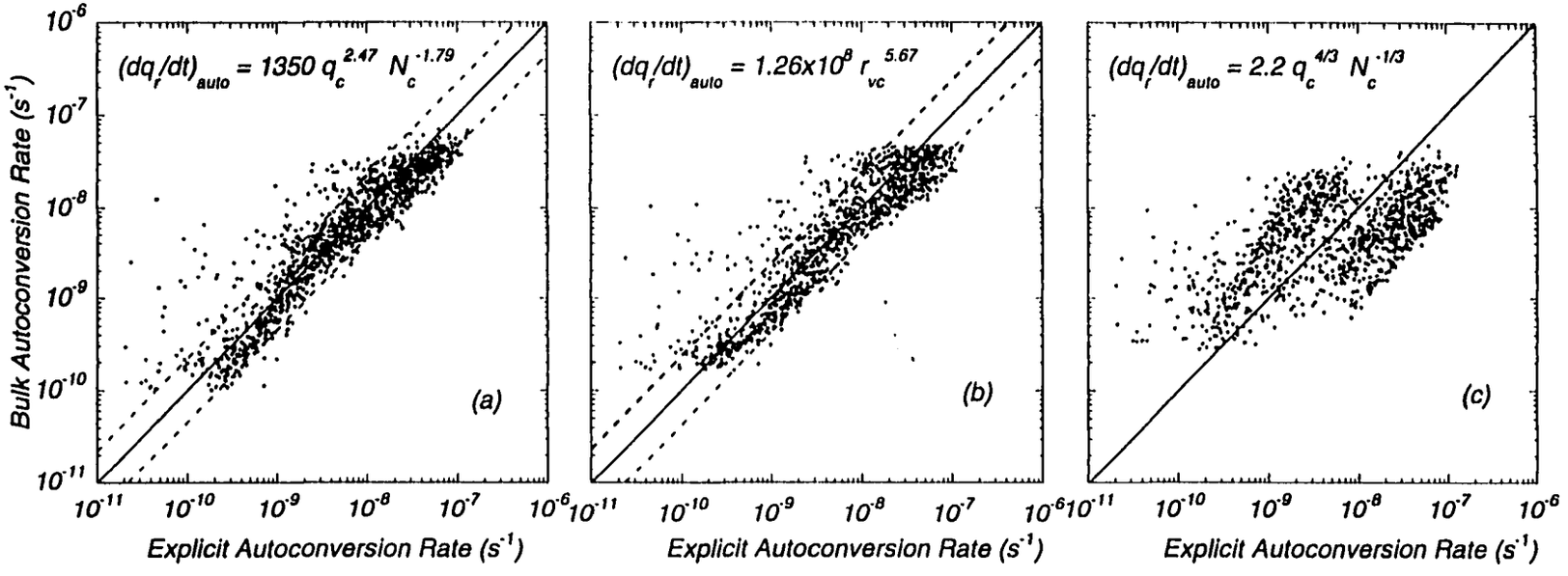

Figure 5.4 Correlation between the bulk autoconversion rates given by different expressions and the corresponding rate obtained from the explicit model. Note that only about 5% of data-points are shown.

threshold value r_0 =25 μm:

$$\left(\frac{\partial N_r}{\partial t}\right)_{auto} = \left(\frac{\partial q_r}{\partial t}\right)_{auto} / \left(\frac{4\pi\rho_w}{\rho_a} r_0^3\right) \tag{5.35}$$

d. Accretion

The accretion rate is defined as the total mass increase in the spectrum bins corresponding to the drop sizes larger than the threshold size used for the autoconversion (see previous section). It is assumed also that the accretion rate depends only on the cloud and drizzle water contents similar to Kessler-type approaches. The proposed expression obtained by using the least square method is given by

$$\left(\frac{\partial q_r}{\partial t}\right)_{accr} = 67(q_c q_r)^{1.15} \tag{5.36}$$

A good agreement between the accretion rate (5.36) and calculated by the explicit microphysics model is demonstrated by the scatter-plot in Fig. 5.5a. If we use (1.17) as the general form of the expression for the accretion rate, and find the coefficient from the regression analysis, we obtain that

$$\left(\frac{\partial q_r}{\partial t}\right)_{accr} = 3.7 q_c q_r \tag{5.37}$$

which tends, though, to underestimate the larger values of accretion (Fig. 5.5b). This can be explained by the fact that the theoretical limit of the coefficient in (5.37), as determined by the assumption of continues growth of drizzle drops with the unit collision efficiency, is about 6. Therefore, the larger accretion rates associated with larger drizzle drops gradually approach the theoretical limit.

The accretion reduces not only the cloud water content, but also the drop concentration. The correspondent sink term is approximated assuming that all collected

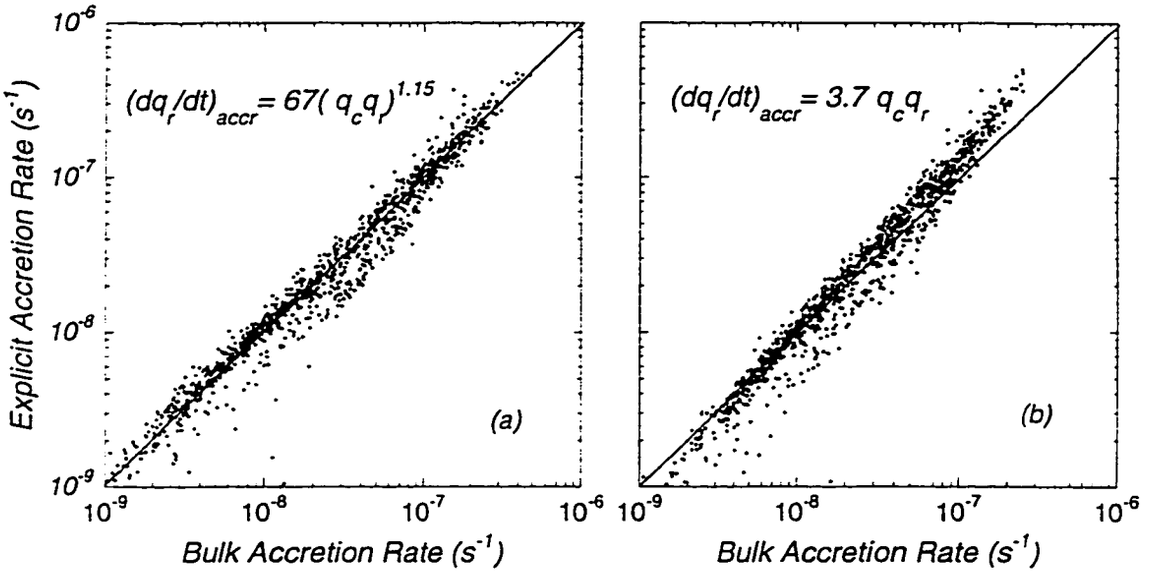

Figure 5.5 Correlation between the bulk accretion rates given by different expressions and the corresponding rate obtained from the explicit model. Note that only about 5% of data-points are shown.

cloud drops have the size of the mean volume radius:

$$\left(\frac{\partial N_c}{\partial t}\right)_{accr} = \left(\frac{\partial q_r}{\partial t}\right)_{accr} / \left(\frac{4\pi\rho_w}{\rho_a} r_{vc}^3\right) \tag{5.38}$$

e. Sedimentation

The mean terminal velocities for the drizzle liquid water and drop concentration were calculated for each sample spectrum as

$$V_{N_r} = \frac{\sum_{i,r_i>r_0} v(r_i) N_i}{\sum_{i,r_i>r_0} N_i} \qquad V_{q_r} = \frac{\sum_{i,r_i>r_0} v(r_i) r_i^3 N_i}{\sum_{i,r_i>r_0} r_i^3 N_i} \tag{5.39}$$

where N_i is the drop concentration in the ith spectrum bin, $v(r)$ terminal velocity of a drop of radius r, and r_0 is the drizzle threshold bin, which is 25 μm. Calculating the mean terminal velocities for each of the sample drop-size spectra and applying the least square method, the following approximations are offered:

$$V_{N_r} = 0.007 r_{vr} - 0.1 \qquad V_{q_r} = 0.012 r_{vr} - 0.2 \tag{5.40}$$

where r_{vr} is a mean volume radius of the drizzle drops and given in μm, while the terminal velocities in m s^{-1}. Corresponding scatter-plots are shown in Fig. 5.6. The r_{vr} should always be larger than 30 μm, which is assumed the lower threshold for the drizzle. Otherwise, if it becomes smaller than the threshold during the coarse of a simulation, the drizzle drop concentration in a given grid point should be corrected so that r_{vr}=30 μm.

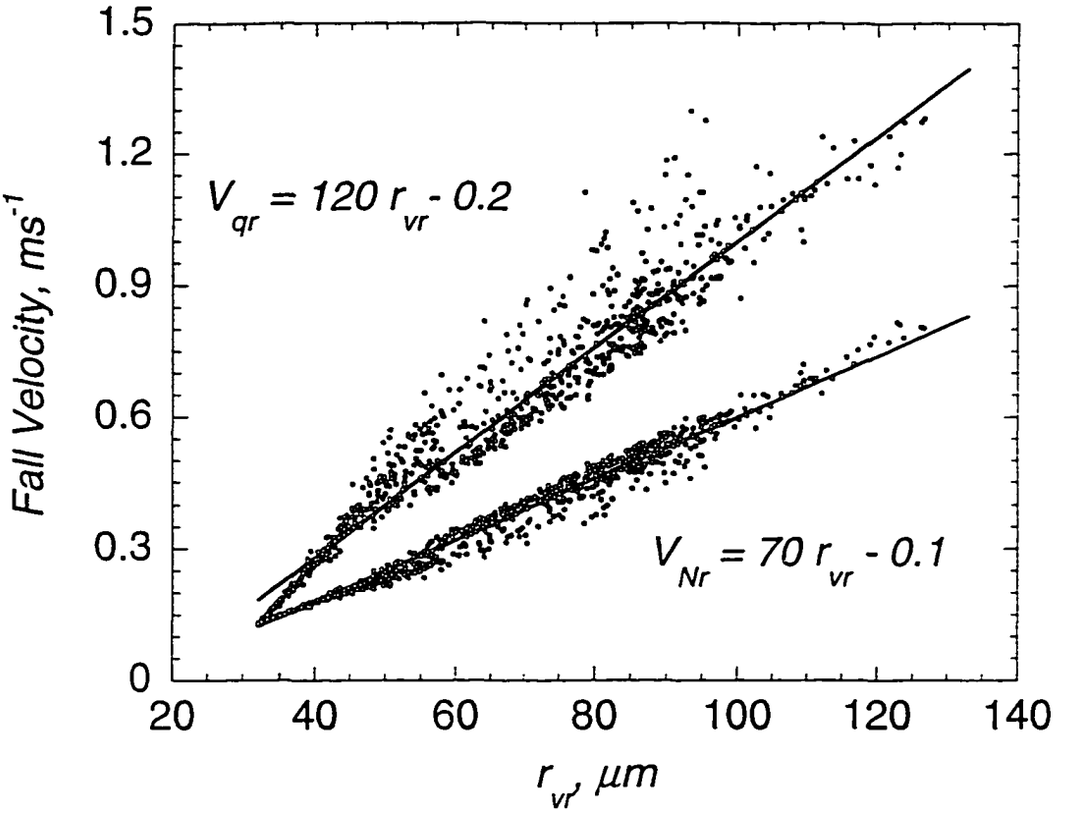

Figure 5.6 Scatter-plots for the mean fall velocities for drizzle water content and drizzle drop concentration. The curves correspond to the expressions used by the bulk microphysics. Note that only about 5% of data-points are shown.

5.5 Non-precipitating STBL

First, the proposed bulk microphysics was compared with the explicit microphysics for the case of non-precipitating stratocumulus. The purpose was to test the ability of the simplified approach to reproduce the drop concentrations and drop spectrum relative dispersion simulated by the explicit approach for different CCN counts. Here, the results of one of the tests are presented.

Two cases were considered. One case represents the "polluted" marine boundary layer with a relatively high CCN count, so that the drop concentration is about 175 cm^{-3}. The other case represents "clean" boundary layer with a relatively low CCN count, so that the average drop concentration is about 50 cm^{-3}. The initial thermodynamic sounding for each case was similar to the UKMRF flight 526, described in Chapter 4. To avoid precipitation, the coagulation calculations in the explicit model and the autoconversion in the bulk model were suppressed. Each simulation ran for 3 hours. The profiles shown in Fig. 5.7 represent the last 40-minute averages.

The agreement between the explicit and bulk models is quite good. Not only was the bulk microphysics able to reproduce such microphysical parameters as the liquid water content, drop concentration, and mean droplet radius, but it also reproduced the relative drop spectrum dispersion (Fig. 5.7d). It should be stressed here that in contrast to the drizzle part of the parameterization, which was calibrated using the spectra simulated by the explicit model, the cloud water parameterization was not calibrated (except the choice of the initial drop radius during the CCN activation (5.16)-(5.17)). The only closure that was used is for the mean inverse radius (see 5.21) based on the assumption that the drop spectra can be approximated by the gamma distribution. The result that both explicit and bulk models predict similar drop spectrum broadness profiles using completely different methods and numerical schemes is very

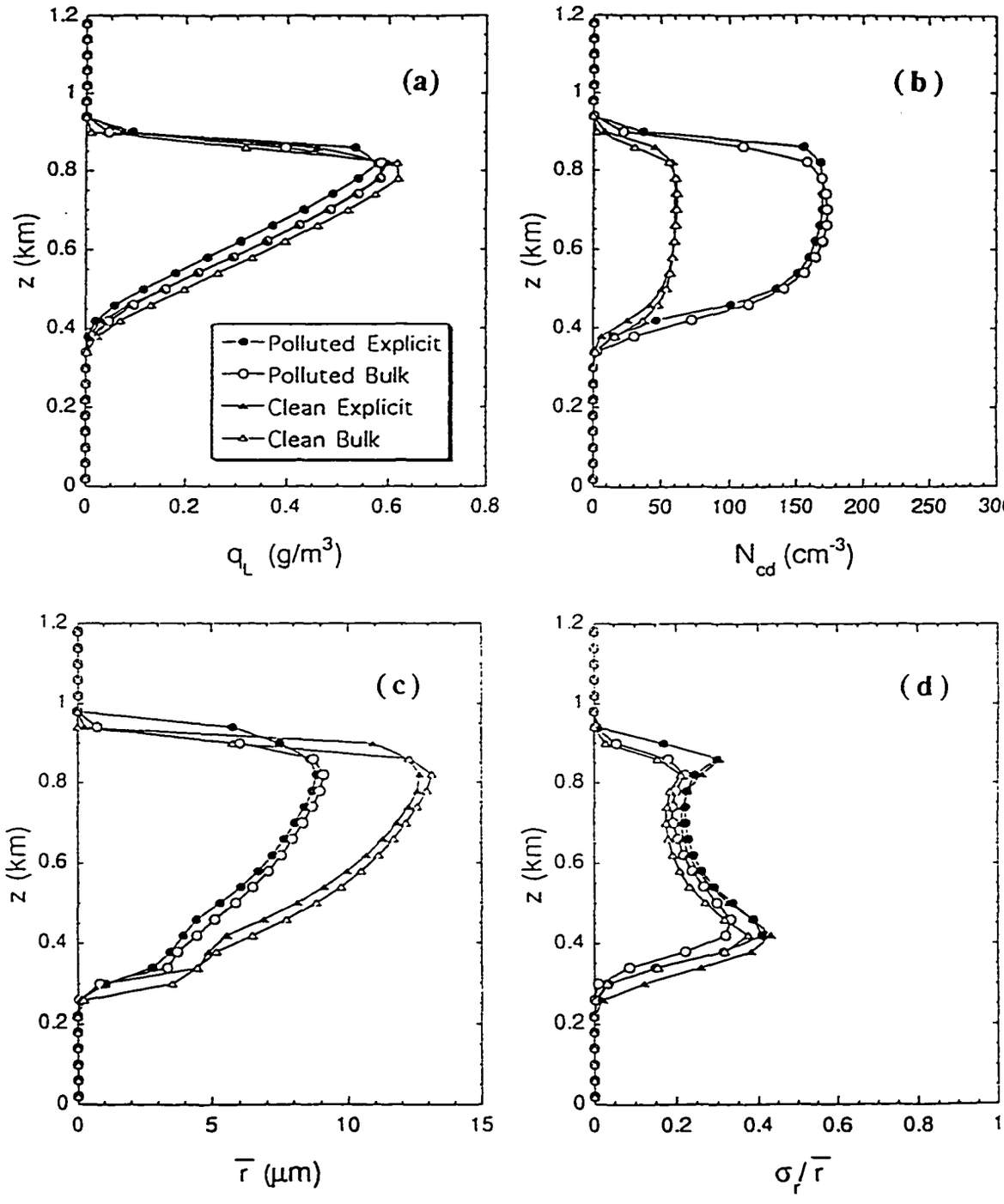

Fig. 5.7 · Vertical profiles of (a) liquid water content; (b) cloud drop concentration; (c) mean drop radius; and (c) drop spectrum relative dispersion for the explicit and bulk microphysical model for "polluted" and clean STBL with nonprecipitating stratocumulus.

encouraging. It suggests that this parameter in both models is controlled by such physical factors as turbulent mixing and CCN activation, and is not strongly affected by unavoidable small numerical diffusion of the drop spectrum in the explicit model.

5.6 Heavy-drizzling STBL

We will now compare the results of the explicit and bulk microphysics simulations of the STBL in the presence of heavy drizzle. The heavy drizzle was caused by a relatively low CCN count, and, consequently, low drop concentration and relatively large cloud drop sizes. This led to high drizzle production efficiency and further removal of CCN from the system, since the latter process is explicitly accounted for in both the explicit and bulk microphysics. The CCN depletion from the system caused even more drizzle, which, in its turn, caused even more CCN depletion and so on. Eventually, the stratocumulus cloud deck was not able to support its integrity and broke-up into cumuli. This case of the stratocumulus-to-cumulus transition caused by the CCN depletion by drizzle will be closely investigated in Chapter 6.

a. Initialization

The initial thermodynamic sounding were based on one used in the third GCSS (GEWEX Cloud Systems Studies) LES model intercomparison workshop held in Clermont-Ferrand in August 1996, and based on the ASTEX A209 flight measurements. It was specified in terms of the virtual liquid water potential temperature and total water-mixing ratio as the following:

$$(\theta_{vl}, q_T) = \begin{cases} (289.8,\ 10.2) & z < 662.5\text{m} \\ (289.8,\ 10.2) + (0.208,\ -0.044)\ (z - 662.5) & 662.5\text{m} < z < 687.5\text{m} \\ (295.0,\ 9.1) + (0.006,\ -0.0028)\ (z - 687.5) & 687.5\text{m} < z \end{cases}$$

The initial wind profile $(u,\ v) = (0.,\ -10)$ m s^{-1} at all levels. The surface pressure was set to 1030 mb. The values for the heat, moisture and momentum fluxes were fixed at 10 W m^{-2}, 25 W m^{-2}, and 0.09 m^2 s^{-2}, respectively. The downward longwave radiation flux at the top of the model domain was set at 302 W m^{-2}. The large-scale subsidence divergence was 5×10^{-6} s^{-1}.

The CCN spectrum in the explicit model was approximated by the log-normal distribution with the median radius 0.1 μm and standard deviation 1.5 μm and the total CCN count 45 cm^{-3} assuming ammonium bisulfate chemical composition. This single-modal distribution implies that most of the CCN particles are activated by 0.1% supersaturation. In the bulk model, we assumed the power-distribution (5.12) with the supersaturation threshold 0.1% and the total CCN count as in the explicit microphysical model. The numerical domain size was 3 x 3 x 1.25 km with the resolution $(\Delta x, \Delta y, \Delta z)$ = (75m, 75m, 25m).

The turbulence was initialized by adding the random noise to the temperature field with the amplitude 0.1 K. The first 40 min of simulations were run using a simple saturation adjustment method to diagnose the cloud water content and with no drizzle allowed. Then, the explicit and the new bulk schemes were initialized using the liquid water field and setting the drop concentration equal to the total CCN count. In the case of the explicit microphysics, the initial spectra were specified as log-normal distributions, although not allowing the drops larger than 20 μm. The coagulation of drops in the case of the explicit microphysics and autoconversion in the case of bulk microphysics was delayed for 20 minutes after initialization of microphysics. Thus, the first hour was actually used for the adjustment of the thermodynamical, dynamical and microphysics fields. Each simulation ran for 6 hours with the 3-sec time step.

For convenience, the simulation base on the explicit and bulk microphysics will be further referred as EXP and BUM, respectively.

b. Time series

First, we will compare the time evolution of the various quantities during the last 5-hour period of simulations. The drizzle is present at the surface after about 20 min past the activation of the drop coagulation routing (Fig. 5.8a). The average drizzle rate at the surface level gradually increases with time approaching values around 1 mm day^{-1} at the last hour of simulation. Note that this rate corresponds to 29 W m^{-2} in terms of latent heat flux, thus roughly compensating the surface turbulent latent heat flux (25 W m^{-2}). The drizzle rate from the BUM simulation appears to follow the trend from the EXP simulation, especially for the first 3.5 hours after drizzle production was allowed. Close to the end of simulation, the stratocumulus regime of the boundary layer was replaced by the cumulus convection, causing a sharp burst of precipitation in EXP simulation as described in Chapter 6.

Figure 5.8b shows the evolution of the maximum cloud covers throughout the boundary layer. A solid Sc layer in EXP broke at about 4th hour of simulation rapidly decreasing to about 90% by the end of the 5th hour, where it stayed unchanged for about half an hour and then fell during the final 1.5-hour down to about 55%. The BUM case shows qualitatively similar behavior with the exception that it appears to lag the EXP by about 1/2 hour. This may be caused by some underestimation of the drizzle rate by the BUM simulation compared to the EXP during the last two hours of simulation time.

The time-sequences of the vertical velocity variance and the turbulent kinetic energy averaged over the entire depth of the boundary layer are shown in Fig. 5.8c and

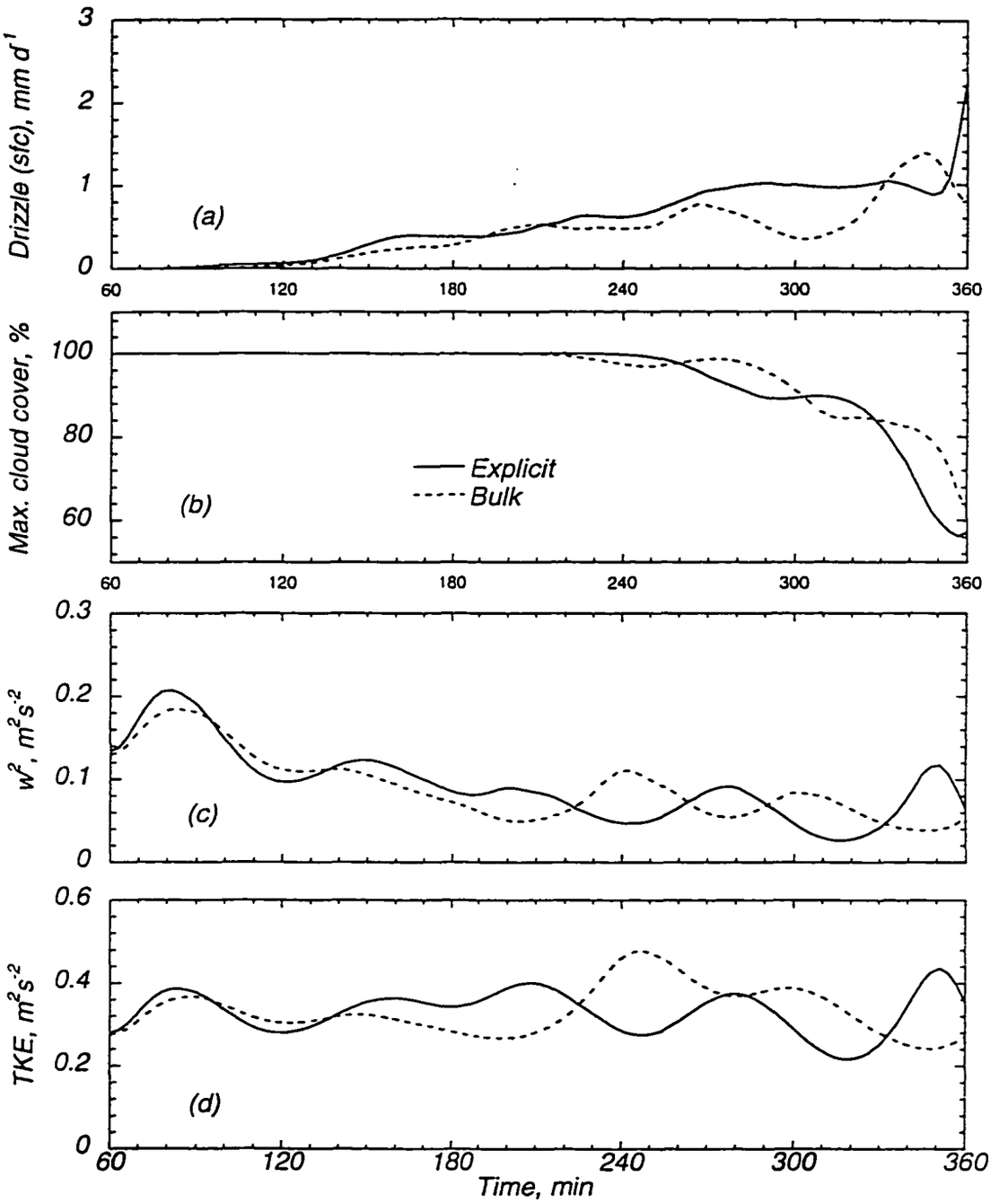

Figure 5.8 Evolution of (a) surface drizzle rate, (b) maximum cloud cover, (c) mean vertical velocity variance, and (d) mean turbulent kinetic energy.

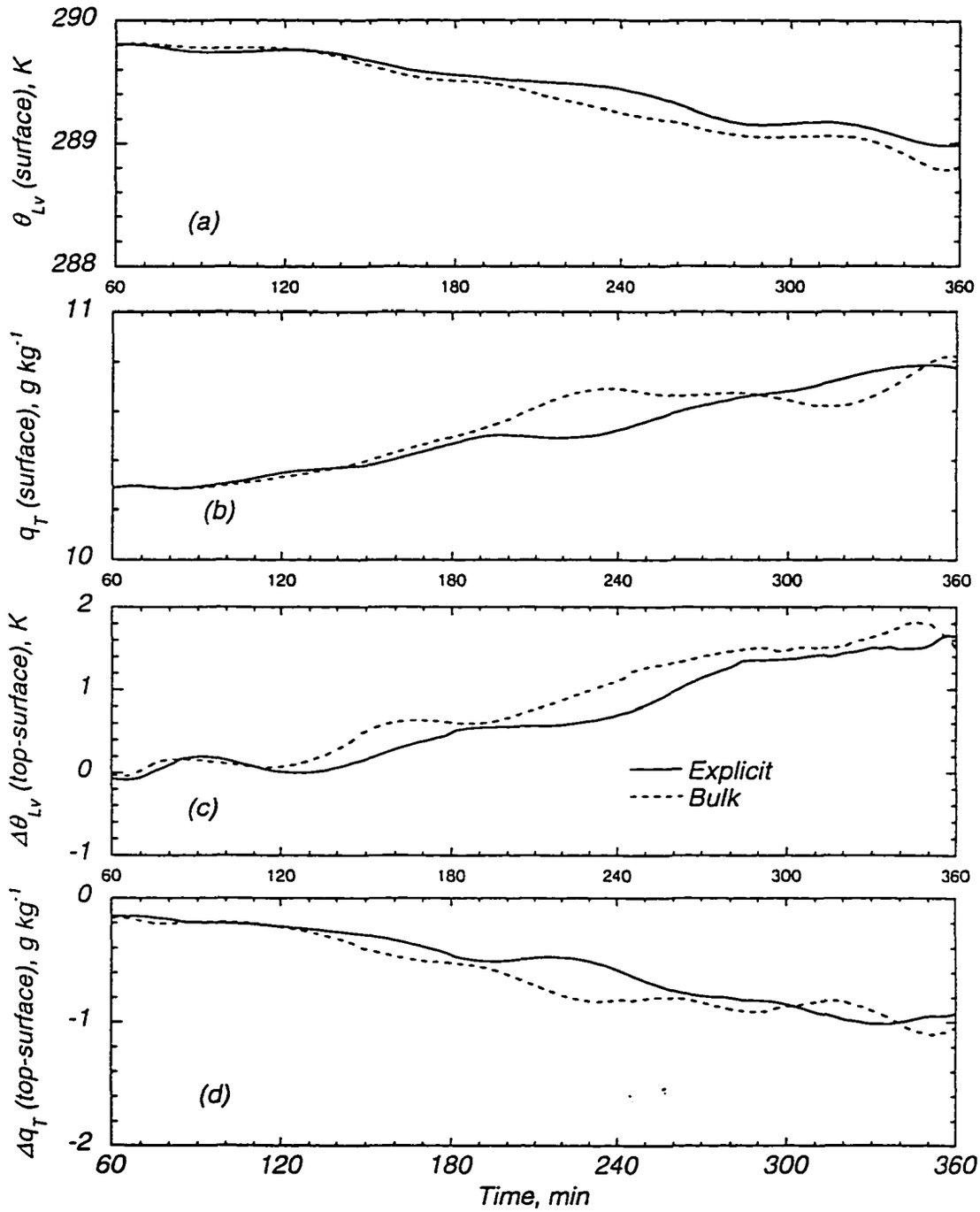

Figure 5.9 Evolution of the near-surface values of (a) virtual liquid water potential temperature and (b) total water with the corresponding top-to-surface differences (c) and (d).

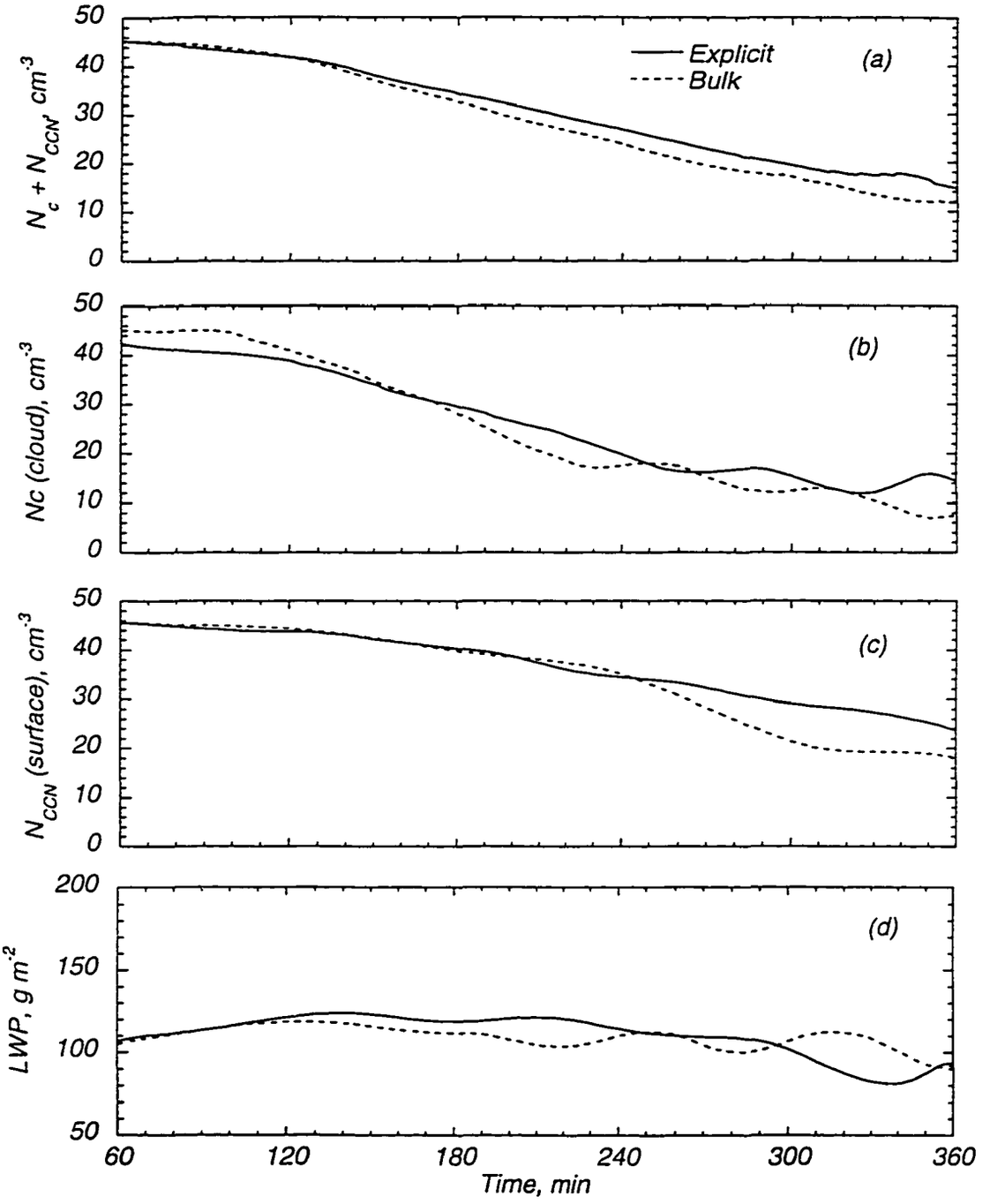

Figure 5.10 Evolution of (a) mean total particle concentration, (b) mean drop concentration, (c) CCN count near the surface, and (d) liquid water path.

Fig. 5.8d, respectively. As drizzle develops, the average intensity of the vertical velocity variance decreases with time as the drizzle evaporation stabilizes the subcloud region. The vertical velocity variance appears to stabilize after the moment of the Sc break-up. However, despite the heavy drizzle and rather dramatic changes in the internal boundary layer structure, the average TKE does not show any apparent trend toward either decreasing or increasing during the course of the simulations. The oscillations in both fields with a period roughly 1 hour must be an artifact of a rather limited spatial domain. Overall, we may conclude that the BUM simulation agrees very well with the EXP simulation in prediction of the average intensity of the turbulence.

The cooling of the surface layer due to drizzle evaporation is apparently stronger than warming due to the surface heating. This results in overall cooling effect and, thus, promotes creation of the stable layer below the Sc cloud (Fig. 5.9a). Drizzle evaporation also moistens the subcloud layer working in accord with the surface moisture flux toward the moisture build-up near the surface (Fig. 5.9b). The temperature contrast between the region near the cloud top and the surface layer monotonically increases with time from its near zero value before the drizzle initiation, indicating the well-mixed state, to almost 2K difference at the end of simulation, indicating development of a rather strong internal stratification (Fig. 5.9c). The same can be said about the total water tendencies except of the reverse sign of the effect (Fig. 5.9d). The overall agreement between the EXP and BUM simulations in predicting these trends is very good.

One of the distinct features of the simulations is the gradual depletion of the CCN pool due to drizzle. The latter removes a certain amount of the cloud water; therefore, the number of drops evaporated upon leaving the cloud layer is smaller than the number of activated drops. The trend is evidenced by the evolution of the total particle number (Fig. 5.10a). This quantity should be conserved in the absence of drizzle and the sources of CCN. The trend shows a rather dramatic decrease in CCN

count - from 45 cm^{-3} before the drizzle started to slightly over 10 cm^{-3} - in just 5-hour period. The mean drop concentration in cloud seems to closely follow the CCN trend (Fig. 5.10b). Stabilization of the subcloud layer decreases exchange of CCN between the surface and cloud. As a result, the CCN near the surface deplete with the rate which is about two times slower than the overall CCN depletion in the boundary layer (compare Fig. 5.10a and Fig, 5.10c).

In general, we see that the BUM simulation reproduces very well the CCN depletion. The largest discrepancy can be noted in the surface CCN count (Fig. 5.10c) after the 4th hour of simulation, where the BUM CCN count decreases faster than the EXP CCN count. Note that the total CCN +CD count does not show this discrepancy. The possible explanation of the discrepancy is that, just prior to the CCN decrease, the TKE trend shows a rather strong increase in turbulence activity, most likely due to a strong rising thermal, which, probably, provided conditions for "ventilation" of the surface layer and, consequently, in the CCN count there.

The last time-series in the sequence is the evolution of the liquid water path (Fig. 5.10d), which is defined as the total liquid water content per unit area. During the first hour after the drizzle initiation, the LWP tends to increase despite the entrainment, because of the small moisture jump in the inversion layer. As drizzle increases, it directly depletes the cloud water content and indirectly reduces moisture fluxes due to stabilization of the subcloud layer, thus, causing a gradual decrease in the LWP. However, the rate is very slow, because of the cumulus activity below the Sc layer, which, as will be shown in Chapter 6, is rather efficient in transporting moisture, and, therefore, to a large extend, compensates for the drying of the cloud layer by drizzle.

c. Vertical profiles

We will now compare the vertical profiles of various quantities. The profiles (Figs. 5.11 and 5.12) represent the 1-hour time averages after the 3rd hour of the simulations when the drizzle is already well developed and the Sc layer is still solid. The qualitative and quantitative agreement between the EXP and BUM simulations is, in general, very good, despite some quantitative discrepancies. One can hardly expect the perfect match in this case, characterized by a rather dramatic evolution of the STBL structure, as show in the time-series plots. The thermodynamic profiles, represented by the virtual liquid water potential temperature (Fig. 5.11a), total water content (Fig. 5.11b), and the liquid water content (Fig. 5.11c) profiles are well reproduced by the BUM simulation showing the well developed internal stratification of the STBL caused by the drizzle evaporation. The turbulent flux of the total water (Fig. 5.11d) as well as the buoyancy flux (Fig. 5.11e) are also well reproduced, especially within the main cloud layer above 400 m. The latter flux is negative in the transition layer below the cloud, indicating that the turbulence there has to do work against internal stable stratification.

The turbulent kinetic energy (Fig. 5.11f) and vertical velocity variance (Fig.5.11g) profiles are also well reproduced by the BUM simulation. The latter show a dual turbulence activity: in the cloud layer due to buoyancy generation by the cloud top radiative cooling, and in the surface layer due to surface heating. The plot of the vertical velocity skewness (Fig. 5.11h) supports the existence of the cumulus-like circulation that couples the surface layer with the cloud layer. It is positive throughout the boundary layer with a strong maximum just above the stable transition layer indicating the updrafts are stronger than downdrafts. Note that in the Sc layers driven solely by the cloud top radiative cooling, the skewness, in general, is negative.

The agreement in such microphysical characteristics as predicted moments for

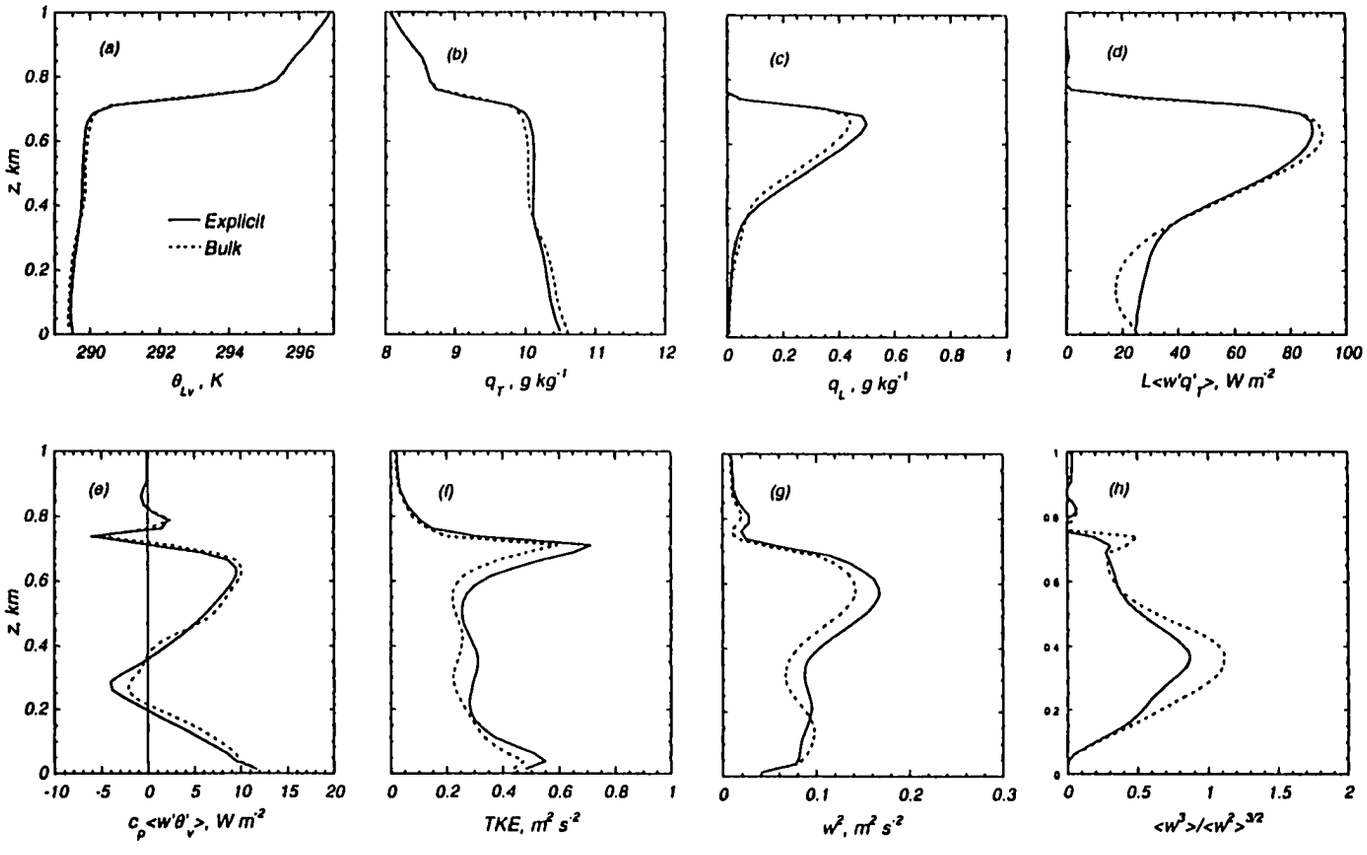

Figure 5.11 Vertical profiles of (a) virtual liquid water pot. temperature, (b) total water and (c) liquid water contents, (d) total water turb. flux, (e) buoyancy flux, (f) TKE, (g) vertical velocity variance and the vertical velocity skewness averaged over 3-4 h period of the explicit (solid lines) and bulk (dashed lines) simulations.

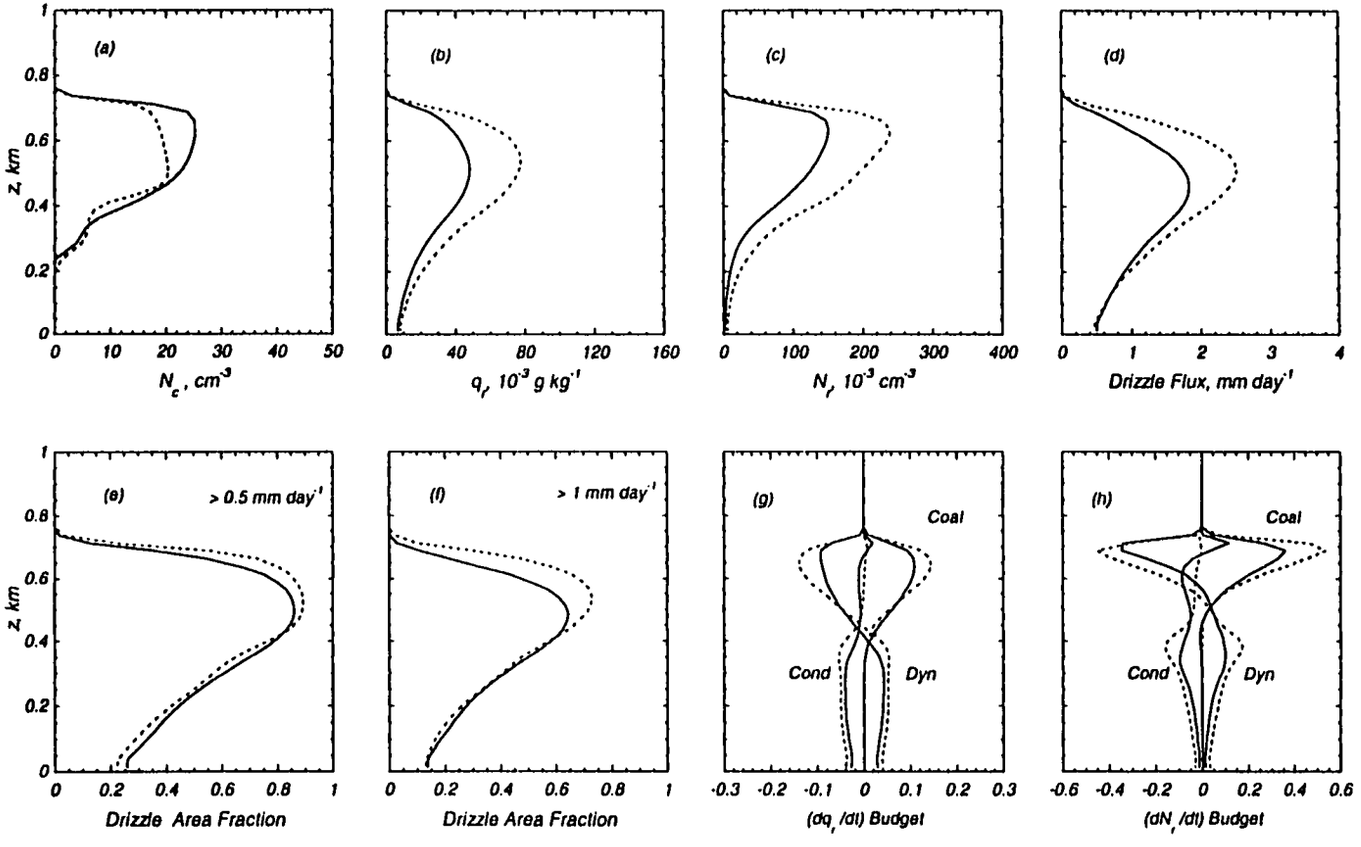

Figure 5.12 Vertical profiles of (a) cloud drop concentration, (b) drizzle water content and (c) drop concentration, (d) drizzle rate, area fruction of drizzle larger than (e) 0.5 and (f) 1.0 mm/day, the rate of change of (g) drizzle water and (h) drizzle drop concentration due to conndensation (Cond), coallescence (Coal) and dynamical transport (aind plus gravitational sedimentation) (Dyn).

the cloud and drizzle water between the EXP and BUM case is also quite satisfactory (Fig. 5.12). The drizzle rate (Fig. 5.12d) is well reproduced especially in the important (from dynamical point of view) subcloud region, where the divergence of the drizzle flux affects the stability of the layer. The fraction of the area, occupied by drizzle with the given rate (Figs. 5.12e and 5.12f) is also well reproduced, indicating that the physical mechanisms of the drizzle initiation in the cloud are satisfactory captured by the relatively simple bulk microphysics. The budgets of the drizzle water (Fig. 5.12g) and drizzle drop concentration (Fig. 5.12h) for the EXP and BUM simulations also agree well. In the cloud layer, the drizzle production almost totally compensates the dynamical removal by sedimentation and wind transport, since the condensation does not play any important role there. This is in accord with the general philosophy of division the liquid water into the cloud water and the drizzle when the latter grows predominantly by the accretion rather than by direct vapor diffusion.

5.7 Summary and conclusions

In this chapter, we have described the new bulk microphysical approach specifically designed for application to the boundary layer clouds. The approach generally follows the Kessler-type bulk microphysics separating the liquid water into cloud water and the drizzle/rain. One of the strongest features of the new approach is an addition of the CCN count as a separate prognostic field. This allows us to predict the cloud drop concentration in the same manner as it is done in the explicit microphysics - using the predicted supersaturation field. The latter is a strong function of the dynamical tendencies of the thermodynamical variables caused by the turbulence field. Thus, the proposed bulk microphysics couples the detailed representation of the turbulence in the LES model with the cloud microphysics. Prediction of the drop

concentration together with the cloud water field provides the opportunity to determine the characteristic cloud drop size in the model, which is important factor in the drizzle initiation mechanism.

The fundamental problem in all Kessler-type bulk microphysical parameterizations is how to describe the process of precipitable water initiation, which is often called autoconversion. While, strictly speaking, there is no need for this process in the explicit microphysics, the autoconversion is the only source of the drizzle drops in the bulk model. The previous attempts to explicitly express this source in terms of the cloud water bulk parameters were aimed mostly to parameterization of the rain initiation processes in cumulus clouds characterized by substantially higher liquid water content than the one observed in marine stratocumulus.

In the proposed bulk parameterization, two key drizzle parameters are predicted: drizzle water content and drizzle drop concentration. The latter is very important for accurate representation of the drizzle sedimentation process, because this process controls the drizzle dwelling-time in cloud, and, therefore, the efficiency of the cloud water accretion by drizzle. In addition, it determines how long the evaporating drizzle falls through the subcloud region determining the rates of cooling and moistening of the environment, which can strongly affect the STBL dynamics.

The predictions of the LES model using the new bulk microphysics were compared with the predictions using the explicit microphysics for two cases: non-drizzling and heavy-drizzling STBL. The first case was designed to test the part of parameterization dealing with the cloud water and CCN activation. The results were very encouraging. Not only was the bulk approach able to predict the cloud drop concentration profiles, but also it predicted the drop spectrum relative dispersion close to the prediction of far more sophisticated explicit microphysical model.

In the second case, we considered a rather challenging case of the heavy-drizzling STBL characterized by a relatively low initial CCN count. The bulk

simulation satisfactory reproduced the evolution of the explicit simulation in terms of such characteristics as the turbulence intensity, drizzle rates, CCN depletion rates, strength of the internal stratification caused by drizzle, and fractional cloud cover. The CCN depletion by drizzle created the condition for even stronger drizzle. Eventually, the stratocumulus layer could not sustain the drizzle and broke up into cumulus convection. This process will be considered in detail in Chapter 6.

The results of comparison allow us to conclude that the proposed bulk microphysical parameterization can be used in place of the explicit microphysics in the LES model of the STBL. This would allow one to use larger spatial domains and longer simulation times than it is currently possible with the explicit model without compromising the basic physics of the cloud processes.

Chapter 6

Effect of CCN on Stratocumulus-to-Cumulus Transition

6.1 Introduction

CCN can affect the stratocumulus clouds in two profound ways. First, the increased CCN count increases the cloud drop concentration, which, for a given liquid water content, reduces cloud drop sizes, and, consequently, increases the cloud albedo (Twomey, 1977). This effect has important climatic consequences, since, as mentioned in the Chapter 1, the stratocumulus cloud layers have a profound influence on the global radiation balance. Here, we will focus on the second important effect, namely, the role of CCN in determining the dynamics of precipitating STBL.

Albrecht (1989) proposed that the reduction in the drizzle rates caused by the increase in the CCN counts would increase the fractional cloud cover by reducing the warming and drying of the cloud layer, thus prolonging their life cycle. Pincus and Baker (1994) offered another hypothesis, which is actually a generalization of the suggestion made by Nicholls (1987) that drizzle may be a determining factor in limiting the cloud LWP. In its essence the hypothesis states that the equilibrium depth of the stratocumulus layers (and therefore their optical depth) is directly related to the CCN count through the drizzle efficiency. That is, the thicker stratocumulus clouds for a given CCN count, the stronger the drizzle. The latter can deplete the cloud water and promote stabilization of the subcloud layer due to drizzle evaporative cooling effect, thus, decreasing the moisture supply from the surface. As the result, the stratocumulus layer could thin reducing the drizzle efficiency, until some quasi-equilibrium cloud

depth is finally established.

Baker and Charlson (1990) proposed a hypothesis of the so-called bi-stability of the CCN-stratocumulus system. Using a simple model of CCN production from the gas-particle reactions and destruction by drizzle, they showed that there are two stable equilibrium conditions - one is for large CCN counts typical in continental environments, and the other is for very low CCN counts typical in clean maritime environments. Ackerman et al. (1993) (referred further as ATH93) argued that the maritime equilibrium condition is an artifact of very simplistic model for the drizzle removal used by Baker and Charlson. ATH93 proposed a hypothesis stating that "marine stratiform clouds may contain the seeds of their own destruction", which means that there is a close coupling between the life cycles of the stratocumulus clouds and CCN in marine layers. According to ATH93, CCN are first formed for a few days in the cloud free boundary layer by the direct gas-particle deposition or through a chain of chemical reactions involving SO_2 (see, e.g. Pruppacher and Klett, 1997). For example, typical production rates of CCN particles, which are mostly composed of the sulfate particles with ~ 0.05-0.1 μm radius, are less then 100 cm^{-3} day^{-1} in marine boundary layers (Baker and Charlson, 1990). This size range corresponds to about 0.1 - 0.2% nucleation supersaturation, which is a rather typical range of supersaturation in the convective STBL as our model shows. This implies that almost all the CCN can eventually become activated when the cloud layer forms.

When the cloud layer grow to the stage when the drop coagulation processes become important, CCN are gradually removed from the boundary layer by accretion of the small drops by drizzle. Then, "the reduction in CCN concentrations can lead to the dissipation of the clouds and the collapse of the boundary layer". ATH93 backed their hypothesis by the observation of the "ship track" phenomenon off the coast of California, where the ambient aerosol counts were observed as low as 5 cm^{-3} at 0.8% supersaturation, so that the clouds could barely form. The aerosol emission from ship's

exhaust system created a line of clouds very well observed from satellite.

ATH93 offered the following mechanism for this phenomenon based on results of their 1-D model. The processes of CCN depletion by drizzle can eventually lead to the optically thinner Sc cloud that would not absorb the longwave radiation as efficiently as the typical Sc cloud. Then, the peak of the radiative cooling would diminish, reducing the turbulence production, and move downward, stabilizing the cloud layer above. As the result, the large-scale subsidence could take over the entrainment, bringing the inversion downward, thus eliminating (collapsing) the boundary layer. In their simulation, CCN count reduced from about 100 to 4 cm^{-3} in about 2 days.

Stevens (1996) argued based on his 2-D eddy-resolving and LES results that one-dimensional PBL models lack the adequate representation of the fundamental processes driving the microphysics in convective STBL. He found that the development of the internal stratification enforced by strong drizzle does not necessarily decouple the cloud layer from the surface fluxes. In contrast, the cumulus-like response of the STBL can strongly couple the cloud and subcloud layers, so that the moisture fluxes may even increase compared to the well-mixed case. He also showed in one of his 2-D eddy-resolving simulations that a very low CCN count (20 cm^{-3}) and resultant heavy drizzle can lead to a trade-cumulus like structure. He could not, however, model a particular mechanism of Sc-to-Cu transition due to rapid CCN depletion by drizzle, since in his model it is assumed that the CCN production is always in balance with the destruction by drizzle, following the bi-stability hypothesis of Baker and Charlson (1990).

This chapter presents the results of LES simulation of the STBL evolution in environment characterized by low CCN count using CIMMS LES model with explicit microphysics. I will show that the response of STBL to the progressive increase in drizzle rates due to positive CCN-drizzle feedback may result in the transition from the stratocumulus layer to a field of isolated cumulus clouds.

6.2 Results

The simulation has already been used in the test of a new bulk microphysics scheme in Chapter 5, so the specifics of the initialization procedure can be found in section 5.6. The time evolution of several important quantities has also been discussed there (see. Figs. 5.8-5.10). During the last 5 hours of simulation, the mean CCN concentration in the boundary layer drops from initial 45 cm^{-3} to 15 cm^{-3}, thus corresponding to about 150 cm^{-3} day^{-1} rate of CCN destruction - higher than the typical CCN production rates mentioned above. The local CCN count, as will be further shown, becomes as low as 2 cm^{-3} by the end of the simulation. The stratocumulus layer breaks up after the 4th simulation hour. Below, we will discuss in more detail the evolution of the vertical profiles of several important quantities (Fig. 6.1 and Fig. 6.2). The profiles represent 1-hour averages for every simulation hour starting with hour two.

a. Mean profiles

The drizzle rate rapidly increases with time (Fig. 6.1d), modulated by significant decrease in cloud drop concentration (Fig. 6.1e) due to CCN depletion (Fig. 6.1f). After the 4th hour of simulation, which corresponds to the time when the stratocumulus layer starts to break-up (see Fig. 5.8b), the drizzle rate at the surface reaches the value of the surface moisture flux. After this moment, the average drizzle rate becomes quasi-stationary. Because of the continuing tendency for the drizzle to increase due to continuous CCN depletion, the stratocumulus cloud responds by reducing its area fraction in order to keep the drizzle profile quasi-stationary. The latent heating in the cloud and evaporative cooling below it become so strong that the turbulence generated by the cloud top radiative cooling and surface heating cannot

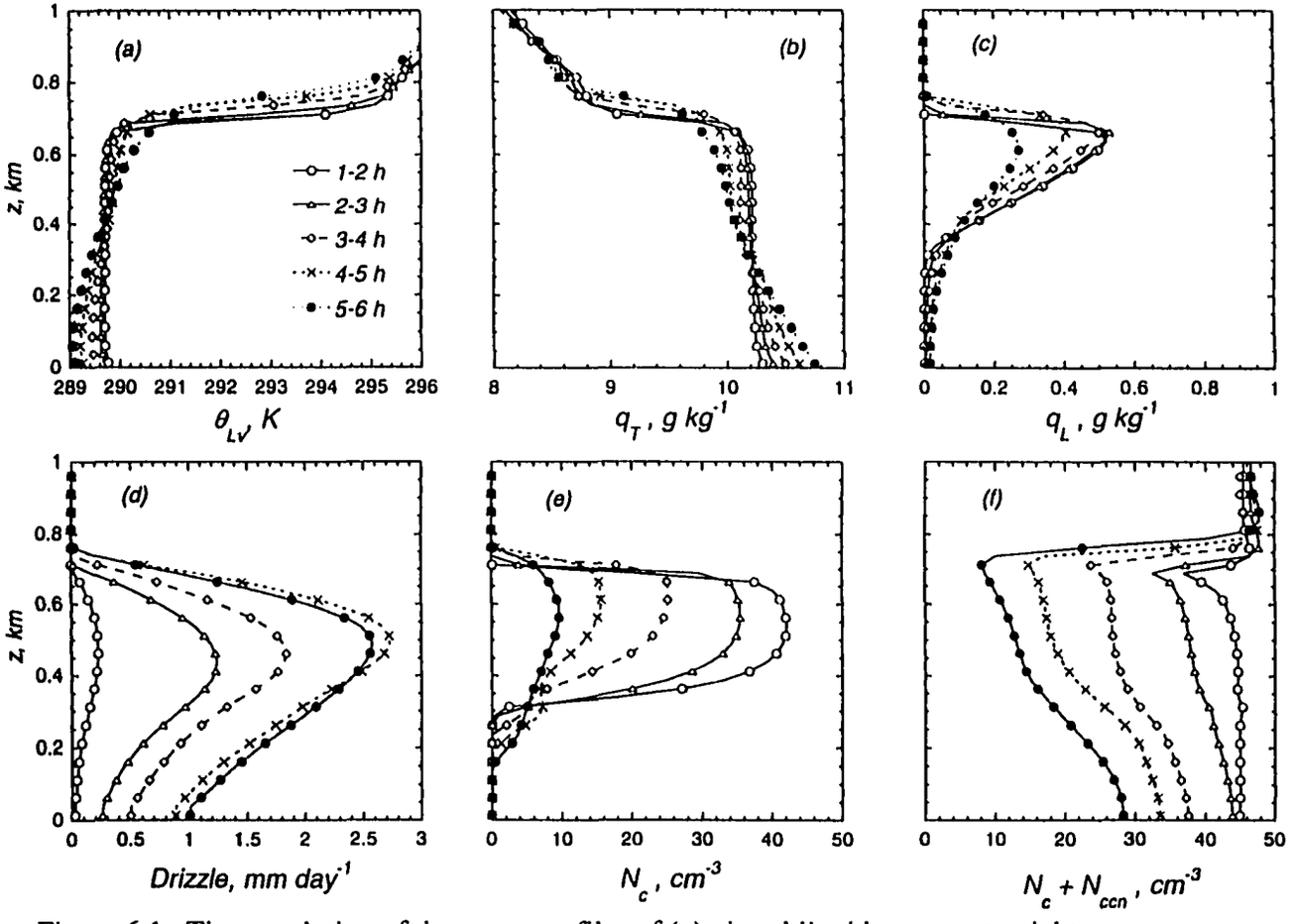

Figure 6.1 Time evolution of the mean profiles of (a) virtual liquid water potential temperature, (b) total water, (c) liquid water, (d) drizzle rate, (e) drop concentration, and (f) total particle concentration. Different symbols represent different time averaging intervals: 1-2 h (open circles), 2-3 h (triangles), 3-4 h (diamonds), 4-5 h (crosses), and 5-6 h (filled circles) of simulation time.

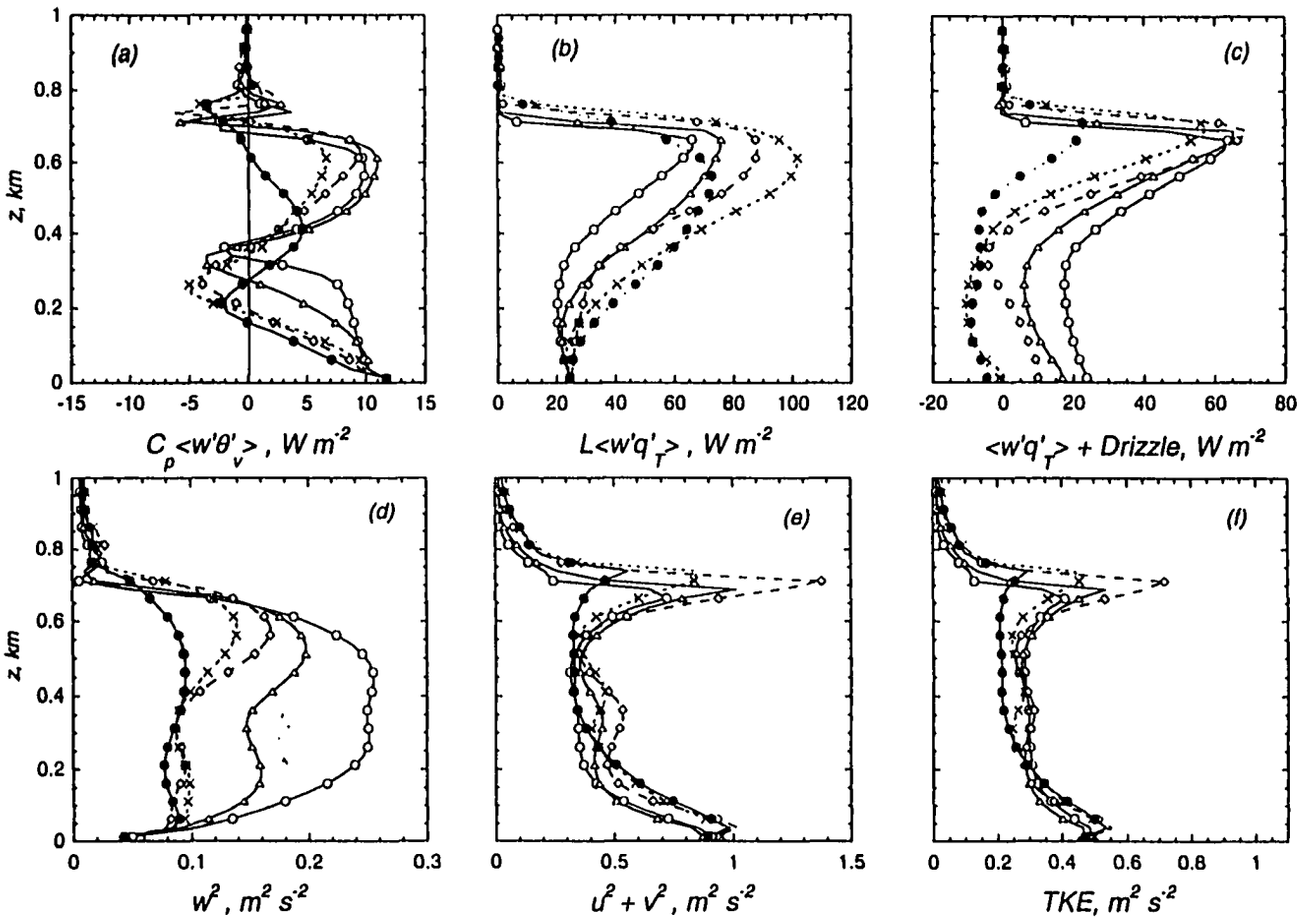

Figure 6.2 Time evolution of the mean profiles of (a) buoyancy flux (b) total water turb. flux, (c) total water flux (turb. + drizzle), (d) vertical and (e) horizonatal velocity variance, and (f) TKE. Different symbols represent different time averaging intervals: 1-2 h (open circles), 2-3 h (triangles), 3-4 h (diamonds), 4-5 h (crosses), and 5-6 h (filled circles) of simulation time.

maintain the well mixed thermodynamic profiles. As the result, by the 6th hour of simulation the boundary layer becomes stably stratified (Fig. 6.1a, and Fig. 6.1b), except for the thin surface layer, where the surface heating is still able to maintain a very shallow mixed layer.

It is interesting to note that the subcloud layer is not only the source of the moisture for the cloud layer, but also a source of the CCN. As one can see from Fig. 6.1f, before the final two hours of simulation, the CCN depletion in the cloud layer was larger than the CCN depletion below the cloud due to upward transport of CCN, until the rate of CCN depletion is the same throughout STBL. This creates a pool of relatively higher CCN counts near the surface. As we will see further, due to this effect, the CCN counts in Cu is significantly higher than in environment previously depleted by drizzle.

By the 6th hour, the stratocumulus layer transforms into a field of cumulus clouds with the maximum cloud fraction of about 50%. This transition is evidenced by a sharp change in the vertical distribution of the buoyancy flux (Fig. 6.2a). In the period preceding the cumulus stage, the buoyancy profiles closely resemble typical profiles in the weakly decoupled STBL dominated by the cloud top radiative cooling. In the cumulus stage, the profile is very different. In the surface layer, the profile behaves as expected in the well mixed cloud-free boundary layer topped by a stably stratified layer. The negative entrainment flux values are about 20% of the surface flux, as many LES studies of the dry boundary layer suggest (see Fig. 3.3). Some parcels in the surface layer become buoyant with respect to the conditionally unstable upper layer, producing the cumulus cloud, which generates the buoyancy due to the latent heat release. Close to the BL top, the environment becomes warmer than the core of the Cu cloud reversing the buoyancy flux. The minimum is also due to Cu "overshooting" the inversion layer.

As was mention above, the turbulent total water flux (Fig. 6.2b) does not decrease due to "decoupling" of the subcloud layer, as 1D PBL models often predict,

but rather increases compensating for the cloud water removal by drizzle. The effective coupling is done by the cumulus elements rising from the surface layer - the circulation that is very difficult to account for in 1D PBL models. The total flux of the total water, defined as a combination of the turbulent and drizzle fluxes (Fig. 6.2c), tends to decrease with time reaching equilibrium when drizzle equals the surface moisture flux. During the final two hours of simulation, the approximate equilibrium reached below the cloud layer, indicates a very efficient coupling of the surface layer with the cloud layer via cumulus convection. By the last hour, the moisture and the drizzle fluxes are close to each other over the entire depth of the STBL.

The vertical profile of the vertical velocity (Fig. 6.2d) at the early stage of the simulation shows a typical profile determined by the surface heating and the cloud top radiative cooling. As the drizzle efficiency increases, the formation of a weakly stabilized subcloud layer makes the turbulent eddies to do an increasing amount of work against the buoyancy forces as indicated by the increasing area of the negative buoyancy flux in the late stage of the stratocumulus regime. The characteristic signature of this process is the existence of the local minimum in the velocity variance profile. The upper portion of the STBL is still driven by the cloud top radiative cooling, while the lower portion is predominantly driven by the surface heating. (The same behavior we saw in the case of the day-time STBL, discussed in Chapter 4, although it was caused by solar heating of cloud rather than by drizzle.) As the result, eddies, impeded by the weakly stable interface, tend to spread horizontally, as evidenced by the development of the local maximum of the horizontal velocity variance in the middle of the STBL (Fig. 6.2e). It is interesting to note that, during the cumulus stage of the simulation, the variance profile seems to be a superposition of the free convection profile and the characteristic profile for the dry well mixed boundary layer as if it were 200-m high with the maximum at about 1/3 of its height (compare with Fig. 3.3). Another interesting feature is that the TKE profile (Fig. 6.2f) is very robust, despite the

large diversity in the drizzle rates, except for the very top, where TKE experiences some fluctuations. This fact questions the realism of the many previous findings made by 1D models that the stabilization of the subcloud layer due to drizzle leads to decrease in the turbulence intensity.

b. Drizzle budgets

The rate of change of the drizzle water can be written as

$$\frac{\partial \overline{q_r}}{\partial t} = -\frac{\partial}{\partial z}\overline{wq_r} + \frac{\partial}{\partial z}\overline{P} + \left(\frac{\partial \overline{q_r}}{\partial t}\right)_{cond} + \left(\frac{\partial \overline{q_r}}{\partial t}\right)_{auto} + \left(\frac{\partial \overline{q_r}}{\partial t}\right)_{accr} \qquad (6.1)$$

Transport Fall-out Condensation Autoconversion Accretion

Where P is the drizzle sedimentation flux defined as being always positive. The autoconversion and accretion terms are estimated similar to the approach used in the development of the bulk microphysics in Chapter 5. The corresponding budgets for the Sc and Cu stages of the simulation are shown in Fig. 6.3. As one might expect, the drizzle water production is dominated by the accretion of the cloud water. The maximum of the accretion rate is reached at about middle of the cloud, but not at the cloud top region where the maximum of the cloud water is located. This is explained by the fact that the accretion rate is not only the function of the cloud water content but also the function of the drizzle drop size. The drizzle drops are mostly formed at the cloud top as evidenced by the autoconversion profile. As they fall collecting cloud drops (and CCN with them), they become larger, so that the accretion rate increases. As the cloud water content decreases downward, the accretion rate also decreases after reaching the maximum somewhere in the middle of the cloud.

The divergence of the turbulent drizzle flux is negative in the middle of the boundary layer and positive near the cloud top and the surface indicating that some drizzle drops are transported upward by the updrafts to the cloud top and by the

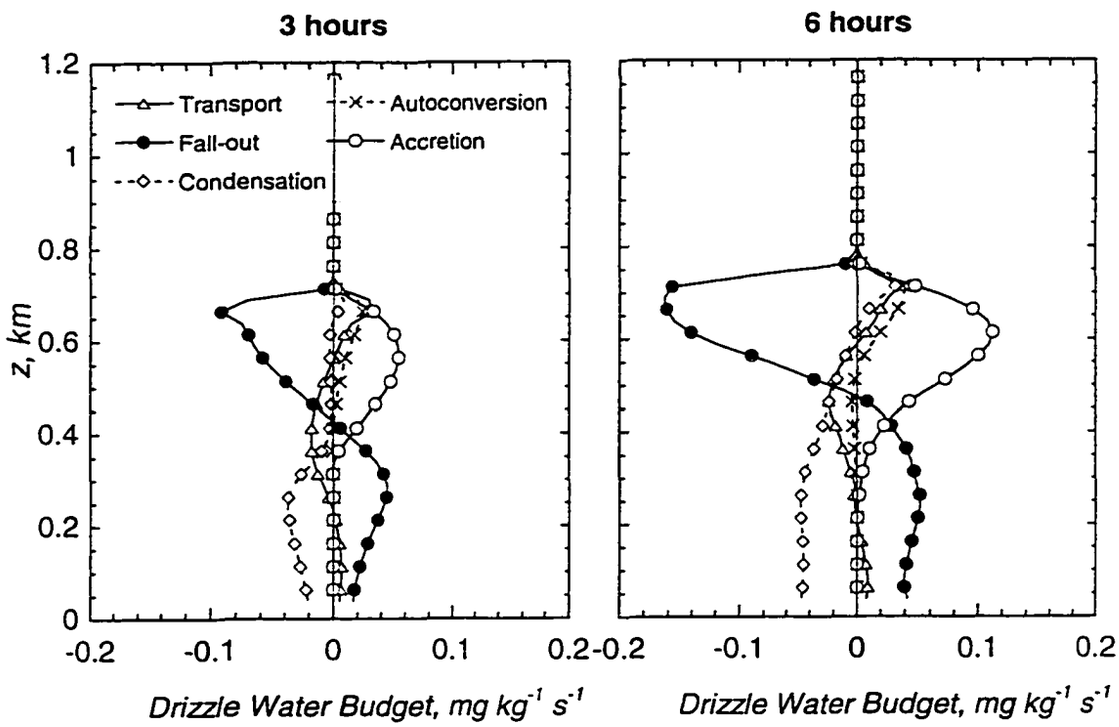

Figure 6.3 The drizzle water balance averaged over 2-3 h (left panel) and 5-6 h (right panel) of simulation time.

downdrafts to the surface. The upward flux of the drizzle might be important for determining the drizzle rates, since the associated term in the drizzle water balance near the cloud top appears to be of the same magnitude as the autoconversion rate.

Qualitatively, the drizzle water budgets for the Sc and Cu stages are similar. The main difference is in the drizzle evaporation profiles. While in the Sc budget the evaporation occurs only below the Sc cloud layer, in the Cu stage it occurs higher in the cloud where the accretion is still active. The latter is determined by the drizzle falling through the unsaturated air from the outflow region at the top of the cumulus outside its saturated core.

c. TKE Budgets

The equation for the resolved scale TKE e can be derived from the momentum (2.1) and continuity (2.2) equations as the following:

$$\frac{\partial \bar{e}}{\partial t} = -\frac{\partial}{\partial z}\overline{w'(e'+\pi')} + \frac{g}{\theta_0}\overline{w'\theta_v'} - \overline{w'u'}\frac{\partial \bar{u}}{\partial z} - \overline{w'v'}\frac{\partial \bar{v}}{\partial z} - \varepsilon \qquad (6.2)$$

Transport *Buoyancy* *Shear* *Dissipation*

The corresponding budgets as well as the corresponding horizontal wind and horizontal momentum flux profiles for the Sc and Cu stages of the simulation are shown in Fig. 6.4. During the Sc stage, the dominant source of the TKE is the buoyant production in the cloud layer as the result of the cloud top radiative cooling. In addition, the TKE is created near the surface as the result of the surface heating and relatively strong wind shear. The buoyancy forces destroy the TKE in the weakly stable subcloud layer, as mentioned above. The transport term redistributes the TKE vertically not creating it, because the vertical integral of this term is equal to zero. From considering the transport

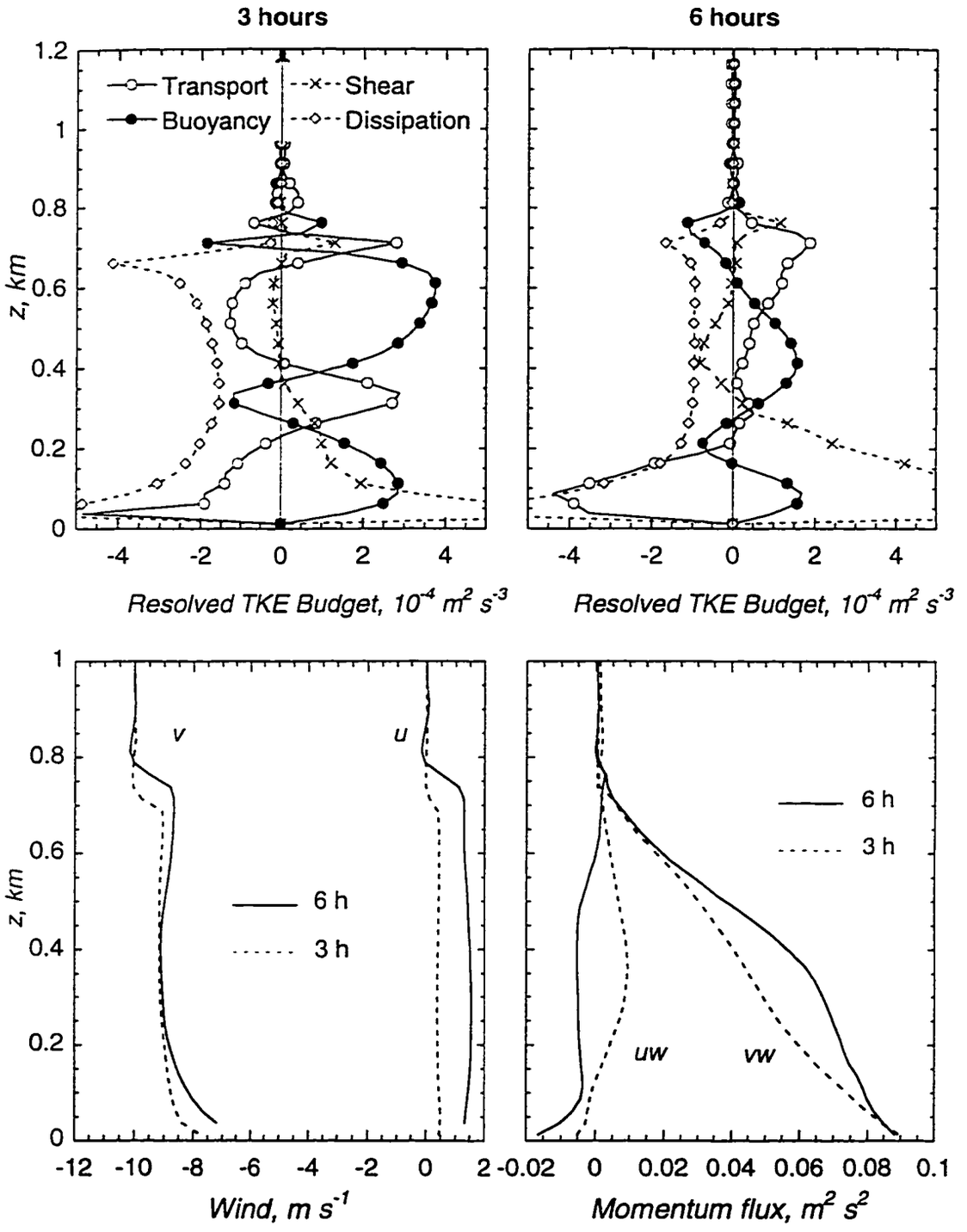

Figure 6.4 The TKE balance (top row), the wind and horizontal momentum fluxes (bottom row) averaged over 2-3 h and 5-6 h of simulation.

profile, one can see that a large portion of the TKE created in the surface layer is spent on counteracting the buoyancy destruction in the subcloud layer. Some of the TKE created in the cloud layer goes to compensate the destruction of the TKE caused by the entrainment of the warm air at the cloud top, as well as the destruction in the subcloud layer.

The TKE budget for the Cu stage of the BL evolution is rather different. The main source of the TKE near the surface becomes the increased wind shear. The momentum is still predominantly transported from the top where it is higher in its absolute value to the surface layer, where it is destroyed by friction. During the Sc stage of the BL evolution, the wind profile is well mixed above the surface layer, so the momentum flux is close to linear. However, during the Cu stage, the smaller momentum from the surface is effectively transported upward by the Cu updrafts, thus decreasing the absolute value of the momentum in the upper region of the BL and in the surface layer. Note that the momentum in the middle of the BL does not change, which creates a condition when the absolute momentum has a local maximum there. This lead to two consequences. First, the wind shear and, consequently, the TKE production in the surface layer increases. Second, since the momentum gradient changes sign at about 0.4 km height, the shear production in the middle of the BL becomes negative, thus destroying the TKE, because of the counter gradient transport of the momentum there.

The buoyancy is still a significant source of the TKE during the Cu stage, especially in the middle of the BL due to the latent heat release of condensation. In the upper portion of the BL, the buoyancy reversal due to warmer environment heated by the outflow from the Cu and due to inversion overshooting is compensated by the transport of the TKE generated near the surface, as evidenced by the transport term profile.

d. Snapshots

The horizontal and vertical cross-sections of various fields corresponding to 3, 4.5 and 6 hours of the simulation are presented in a serious of Figures 6.5-6.10. During the well developed Sc stage, corresponding to 3h plots (Figs. 6.5-6.6), the Sc layer already shows an apparent meso-scale organization with a significant contrast in horizontal distribution of the LWP, from the values as low as 20 g m^{-2} to as high as 200 g m^{-2}. The elevated values of the LWP are very well correlated with the areas of updrafts as well as with the high drizzle rates. The areas of diminished LWP correspond to the areas of the subsiding air. The horizontal x-z cross-section through the area of elevated LWP (Fig. 6.6) shows a solid Sc cloud deck with localized strong drizzle cores. We see that the drizzle tends to coincide with the local updrafts, which increases its mass due to drop suspension effect. The boundary layer is still fairly well mixed in terms of the thermodynamical variables. The total particle field (drops plus CCN) does not show yet a noticeable contrast.

One and half hour later (Figs. 6.7-6.8), the contrast in the LWP further increased. In fact, stratocumulus layer already broke-up in one area (upper left corner). The convective cells embedded into the Sc are now clearly seen. The updrafts became narrower as they strengthened. The worth-noting feature is a local strong maximum in the LWP, which is not apparently correlated with high drizzle rate (low left corner of the domain). The vertical cross-section though the updraft (Fig. 6.8) shows high values of the vertical velocity there - more than 5 m s^{-1}, so the newly created drizzle drops do not have a chance to fall through the updraft and carried away by the outflow at the cloud top. The total particle field already shows a rather significant contrast. In some areas near the cloud top, the concentration fell as low as to a few particles per cubic centimeter. The thermodynamic fields show an apparent formation of the internal stratification.

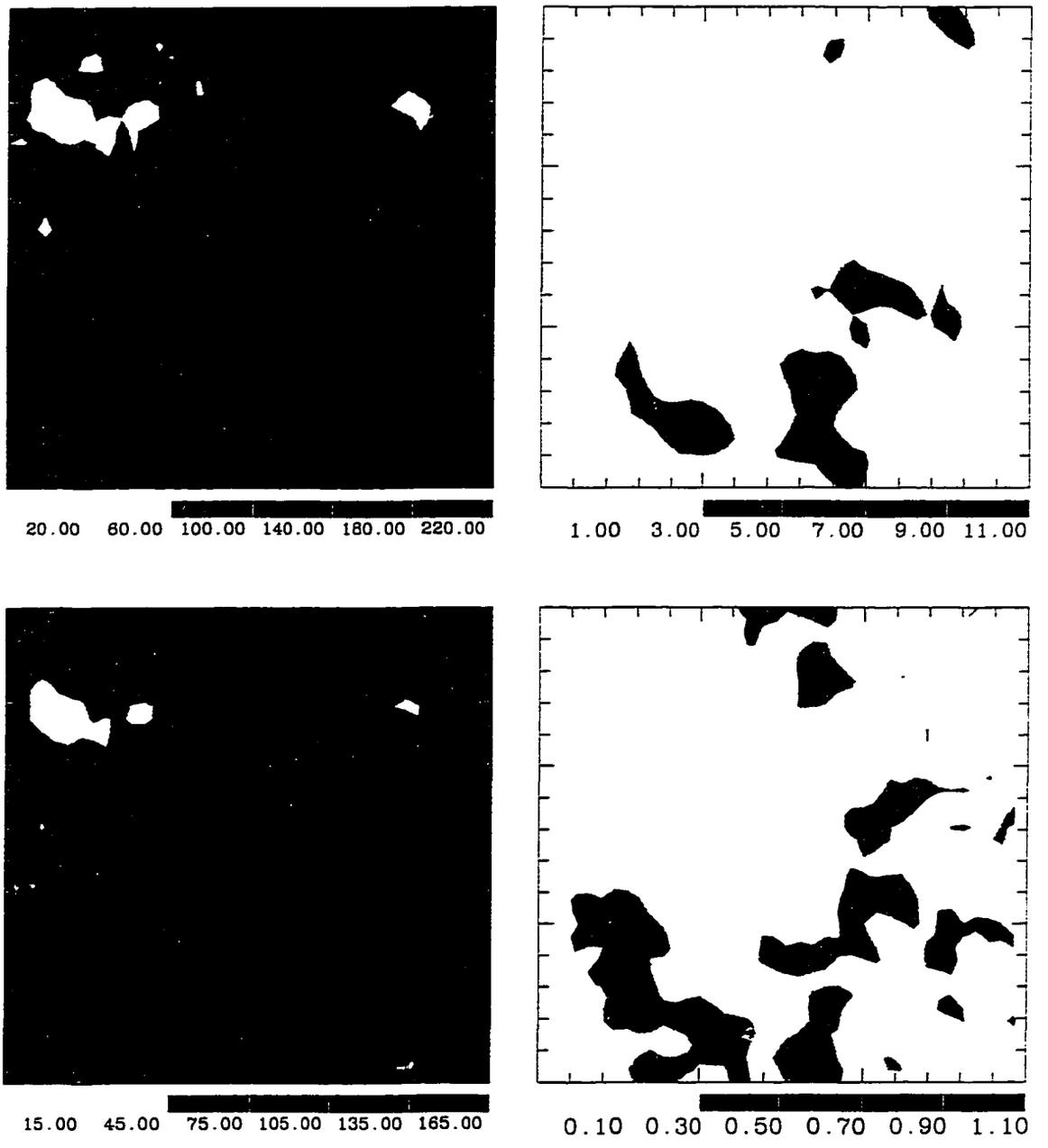

Figure 6.5 Horizontal distribution of the (*top row from left to right*) liquid water path (g/kg) and drizzle rate at 400 m (mm/day); (*bottom row*) drop concentration path (10^6 m^{-2}) and vertical velocity (m/s) at 500 m (updrafts only) after 3 hours of the simulation. The horizontal domain dimensions are 3x3 km^2, horizontal and vertical axes correspond to the x and y directions, respectively, with (0,0) point at the left low corner of each plot.

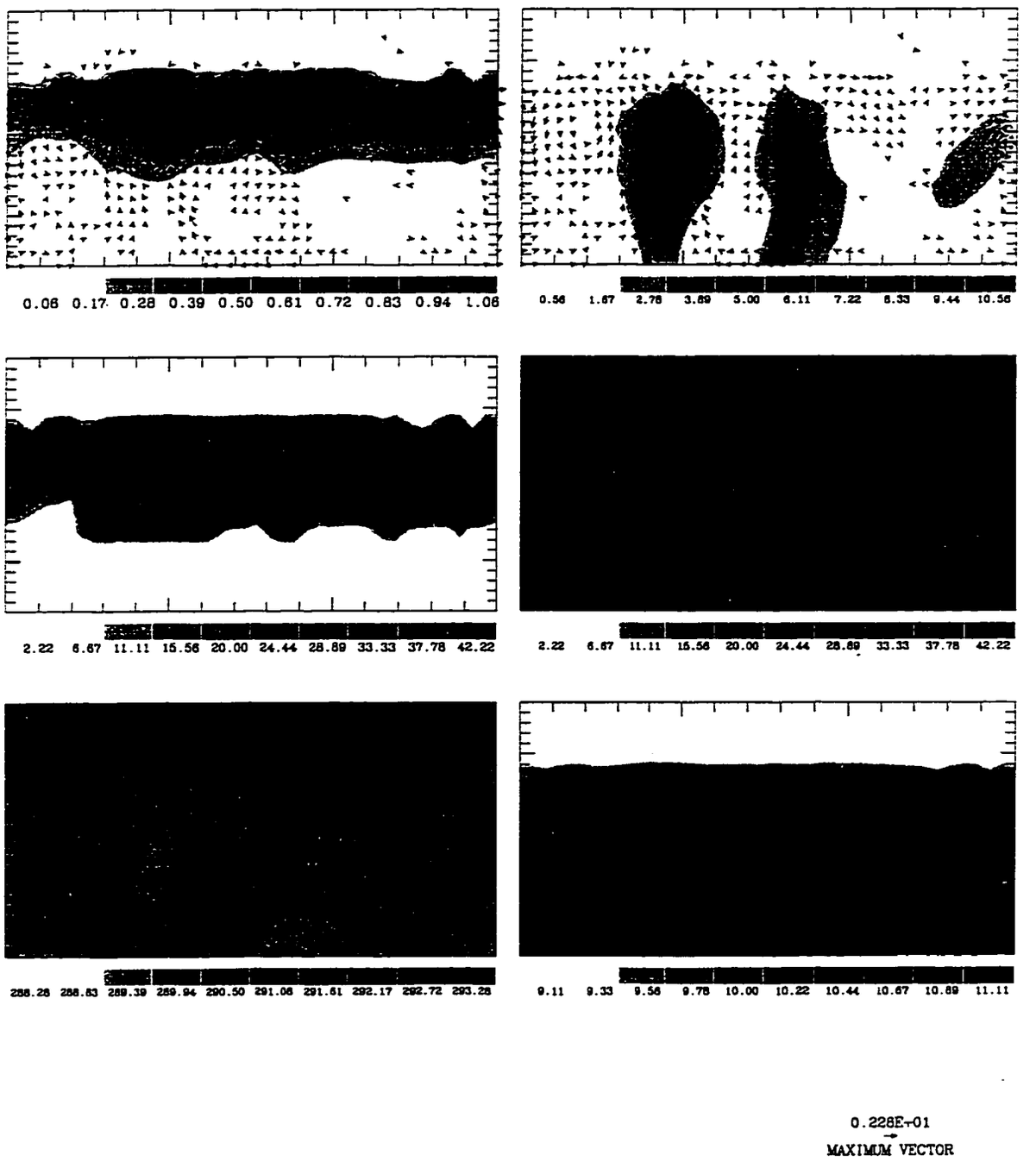

Figure 6.6 Vertical cross-section at y=0.4 km (see Fig. 6.5) of the (*top row from left to right*) liquid water content (g/kg) and drizzle rate (mm/day); (*middle row*) drop concentration (cm^{-3}) and total particle concentration (drops plus CCN) (cm^{-3}); (*bottom row*) virtual liquid water potential temperature (K) and total water mixing ratio (g/kg) after 3 hours of the simulation. The horizontal and vertical dimensions are 3 km and 1 km, respectively.

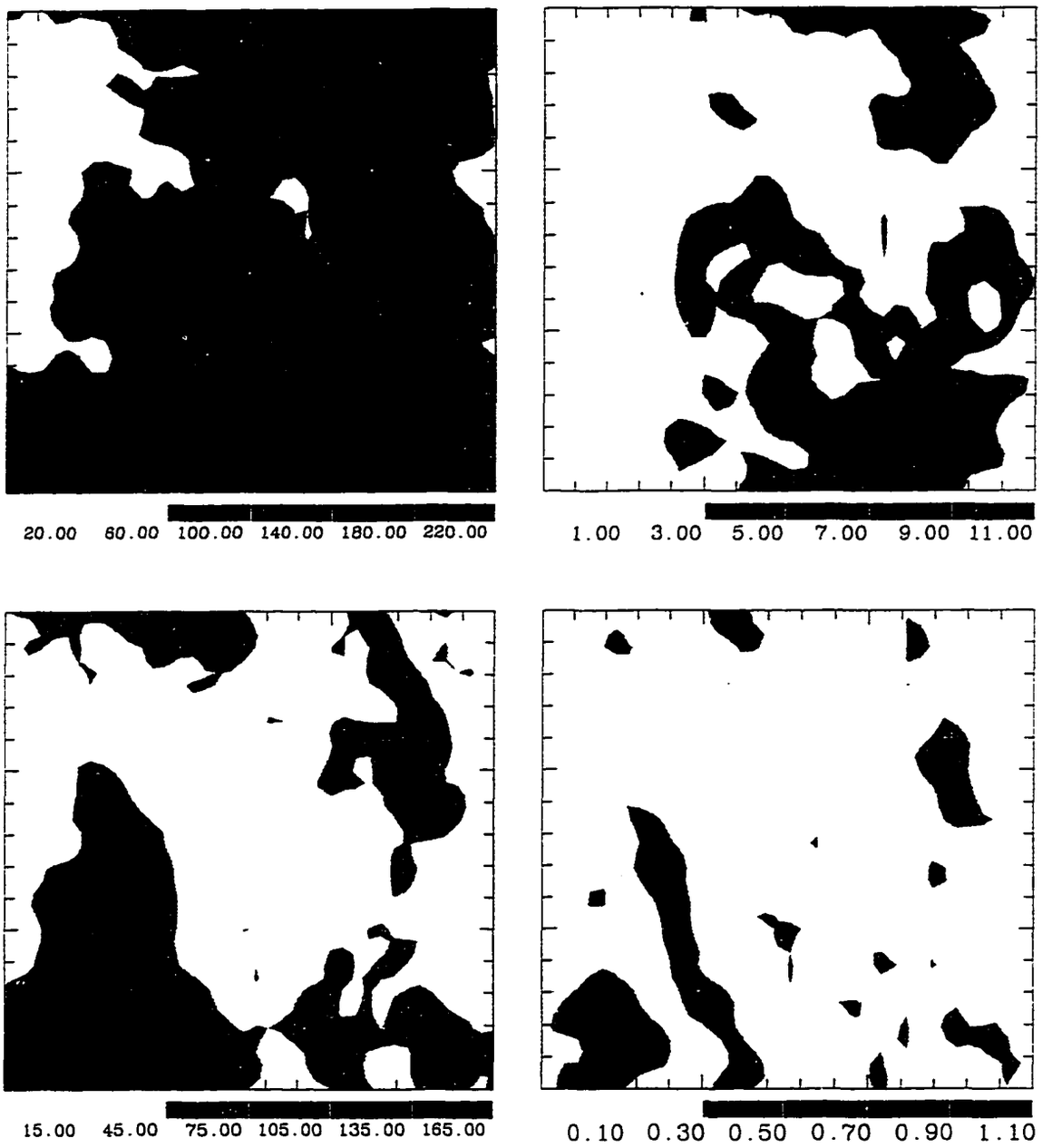

Figure 6.7 Similar to Fig. 6.5, but after 4.5 hours of the simulation.

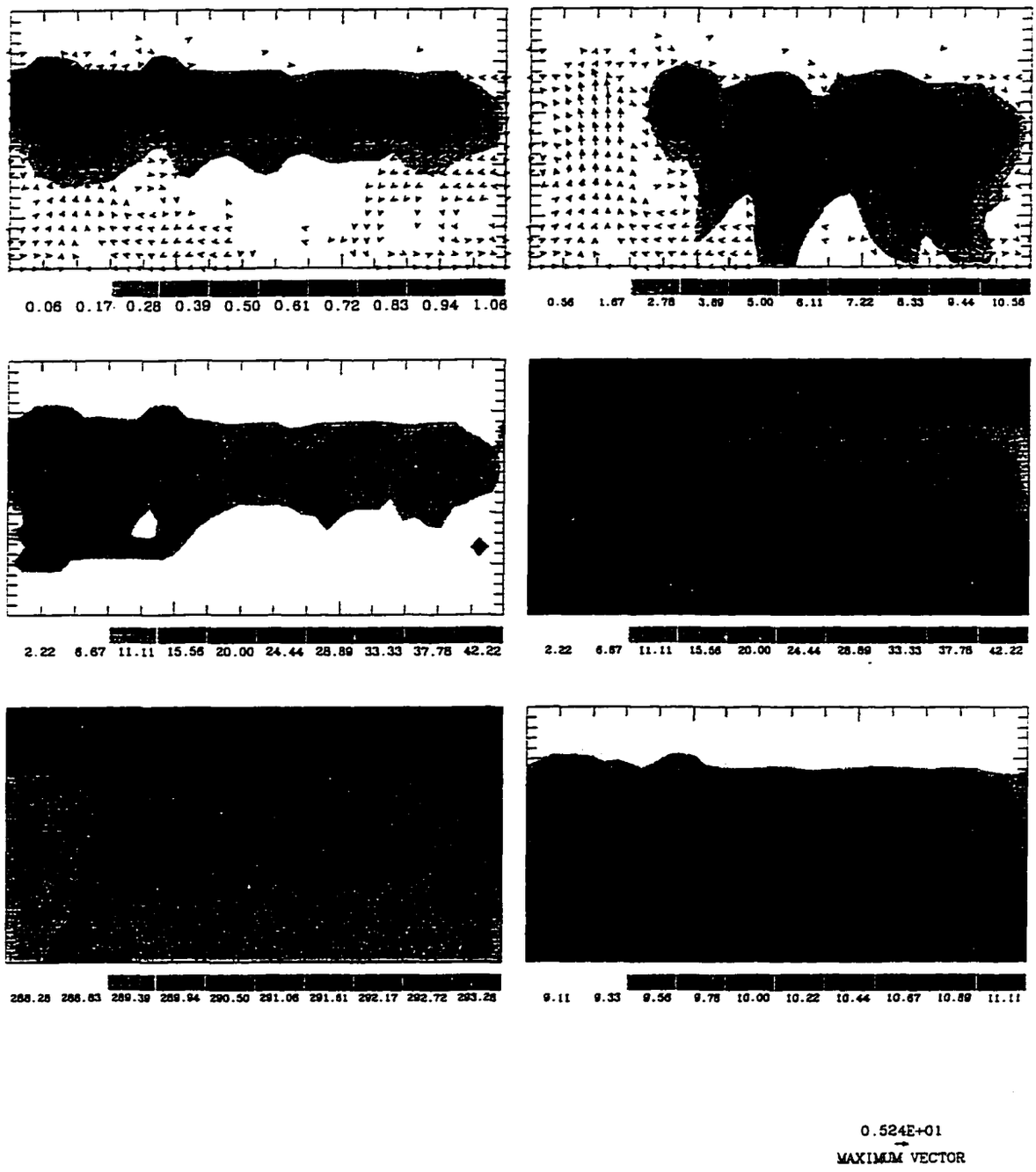

Figure 6.8 Similar to Fig. 6.6, but for y=0.5 km after 4.5 hours of the simulation.

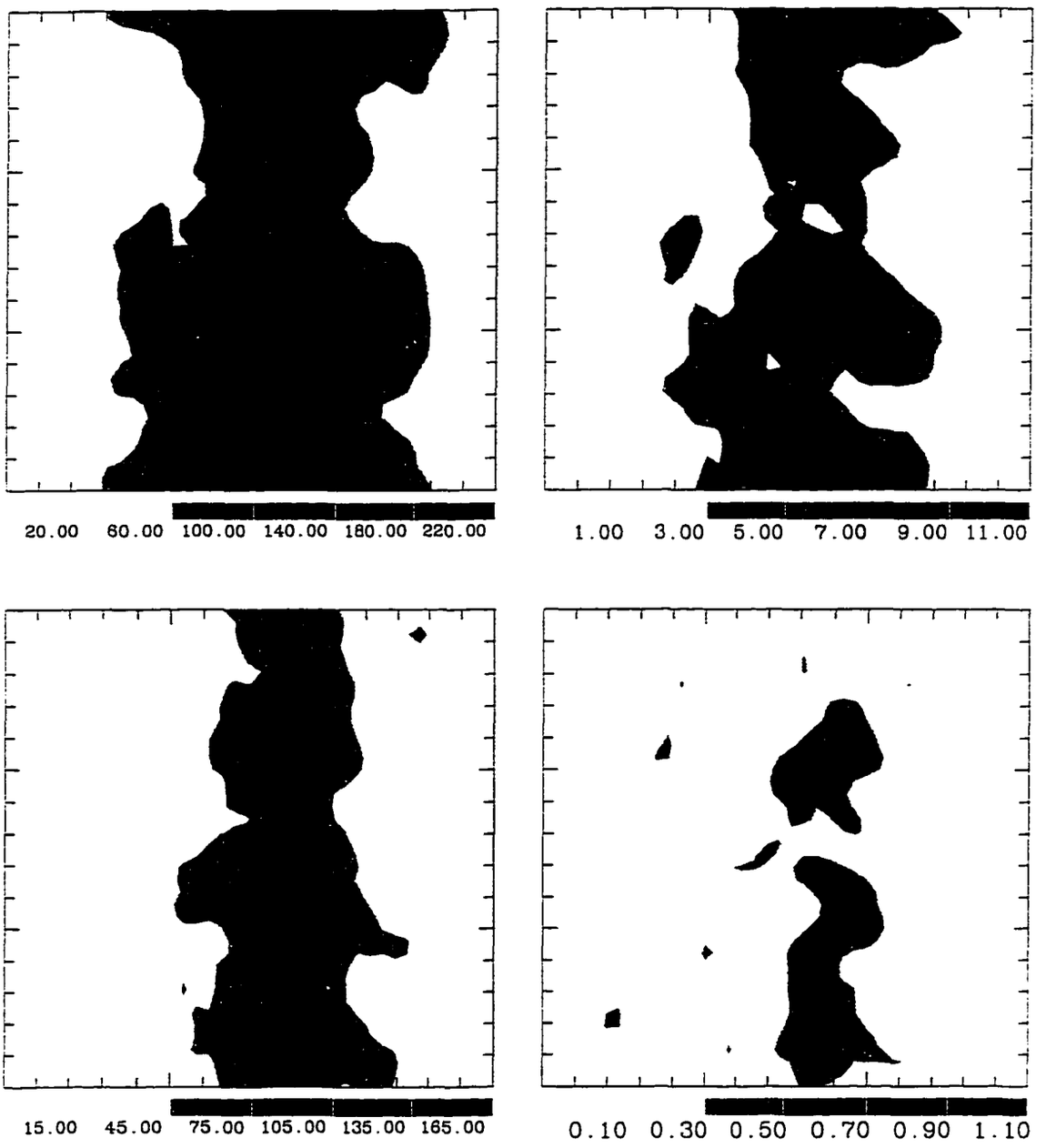

Figure 6.9 Similar to Fig. 6.5, but after 6.0 hours of the simulation.

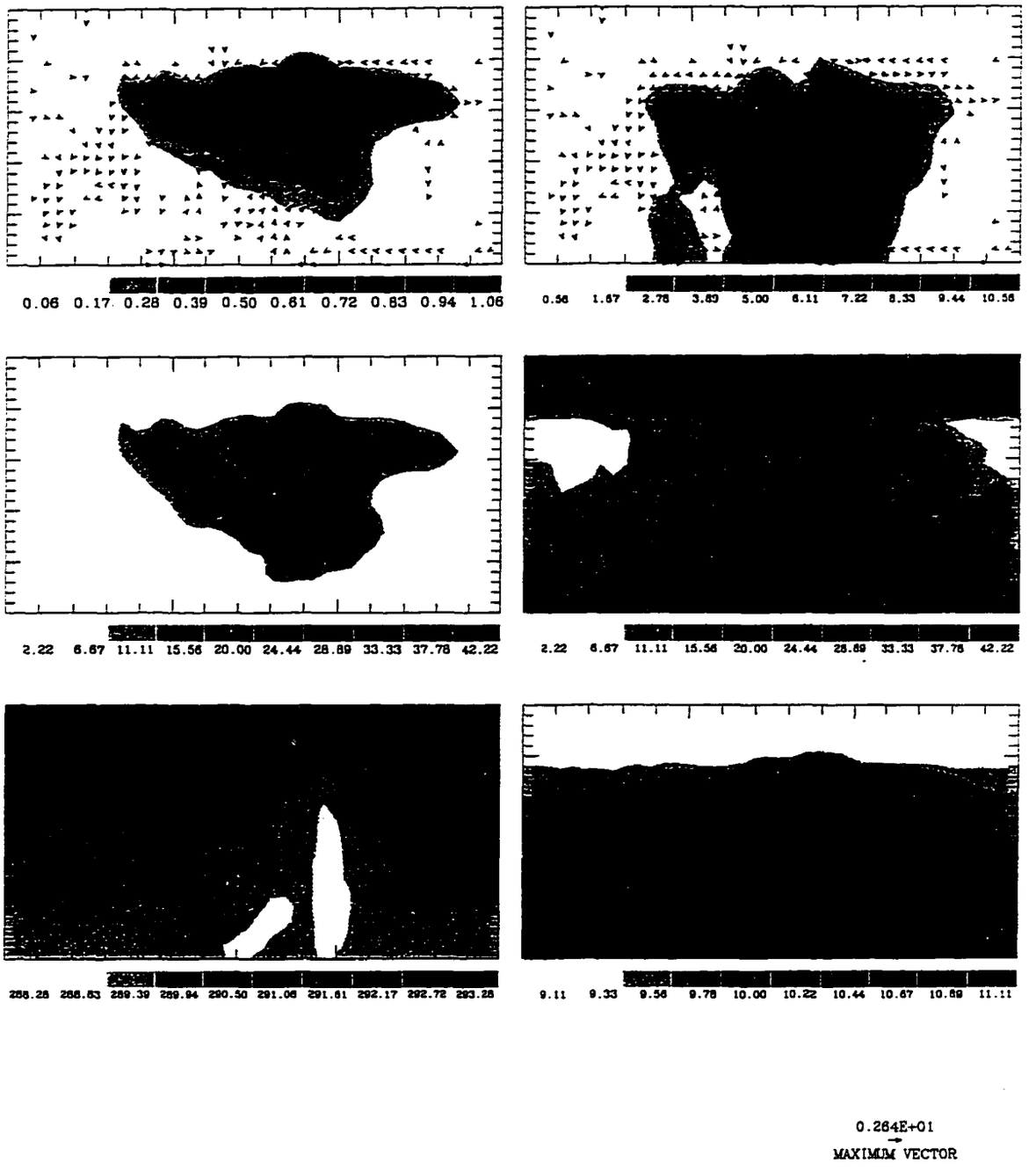

Figure 6.10 Similar to Fig. 6.6, but for y=1.2km after 6.0 hours of the simulation.

During the next 1.5 hour, the stratocumulus layer finally transformed into the line of Cu clouds (Figs. 6.8-6.9) with the preferred north-south orientation along the mean wind in the boundary layer. The maximum precipitation now well coincides with the position of the local updrafts. The vertical cross-sections show a characteristic cumulus-like circulation, with the strong precipitation in the convective core, and lighter precipitation from the "stratiform" outflow region. This outflow of the air warmed by the latent heating associated with the drizzle spreads perpendicular to the cloud line leading to a substantial stabilization and drying-out of the cloud free area. This area is also characterized by very low CCN counts as low as 2 cm^{-3}. There is still a substantial number of CCN near the surface cut off from the CCN above by a stable layer. Eventually, they go through the convective updraft, where they are efficiently removed by drizzle.

6.3 Summary and conclusion

I have simulated a case of the stratocumulus-to-cumulus transition triggered by depletion of CCN by drizzle using CIMMS LES model with explicit microphysics. Stevens (1996) did the closest study showing a trade-cumulus like response of the STBL to the heavy drizzle caused by low CCN count. In his 2-D simulation, however, the "CCN-drizzle" positive feedback could not be activated, since the CCN counts were not allowed to change in response to removal by drizzle.

This study was motivated by the study by Ackerman et al (1993), who offered the hypothesis that the depletion of CCN by the drizzle in the STBL can eventually collapse the boundary layer. They offered a physical mechanism for the collapse based on the results of 1D PBL model. In my simulation, I did not find a support for the offered mechanism and, similar to Stevens (1996), believe that it is an artifact caused by the inability of 1D PBL models to adequately simulate the convective response of

the STBL to the internal stratification of the STBL influenced by drizzle.

Most previous hypotheses, concerning the effect of drizzle on the STBL evolution, were based on the results of simplified 1D PBL models. The prevailed view on the STBL evolution in the presence of strong drizzle has been based on the concept of decoupling of the cloud layer from the surface supply of moisture due to latent heating in the cloud layer and evaporative cooling in the subcloud region. In this scenario, the cloud layer would thin until reaching the equilibrium with the entrainment rate, surface moisture flux, and the drizzle rate. This is in essence the mechanism behind the Pincus and Baker (1994) hypothesis. Stevens (1996) have shown, however, that a more likely response of the STBL is not the decoupled structure with reduced fluxes, but rather a strong coupling through the cumulus-like convection with even increased fluxes. This is in accord with my simulation.

The response of the STBL to the development of the internal stratification was indeed the cumulus-like convection. In the presence of drizzle, the moisture was very efficiently supplied to the cloud layer by the convective elements. In this condition, the stratocumulus cloud did not respond by simply reducing its mean depth, but rather by reducing the drizzle production area by reducing the cloud fractional cover, at the expense of the cloud regions located in the subsidence regions surrounding the regions of the strong updrafts.

In the simulation, the mean drizzle rate was gradually increasing, until its surface value reached the value of the surface moisture flux. Since the drizzle continues to remove the CCN, further increase would mean the depletion of the total water amount in the boundary layer, and thus, would thin the cloud, which would reduce the drizzle. However, the response of the system was different. Instead of preventing the drying of the STBL by thinning the cloud layer, the STBL prefers to reduce the average drizzle flux by reducing the cloud fractional cover. This is in agreement with the Albrecht's (1989) hypothesis, mentioned above, although the physical mechanism is

quite different.

As the area occupied by the cloud is reducing, the outflow from the convective elements warmed by the latent heat release in the convective core, spreads horizontally stabilizing and drying the air surrounding the convective elements. Eventually, the boundary layer separates into two layers: the well-mixed cloud free surface layer driven by surface heat fluxes and, in considered case, by shear, and the conditionally unstable upper layer capped by the inversion with the embedded cumulus clouds connected to their moisture and CCN supply in the surface layer. The structure very closely resembles the shallow cumulus convection over the surface heated well-mixed cloud free boundary layer with the conditionally unstable air aloft.

There are several limitations that, for simplicity reasons, have been imposed on the simulation. First, I ignored the production of the new CCN. However, I believe that this limitation was not serious for the purpose of this study, because of significantly higher CCN destruction rates compared to the typical CCN production rates for the clear sky conditions. Inclusion of the source of CCN would probably slow down the rate of the Sc-to-Cu transition without affecting the principle physical mechanism behind it. Another limitation concerns the fact that the surface moisture, heat and momentum fluxes were fixed. The moisture build-up and cooling of the surface layer caused by drizzle would decrease the moisture flux and increase the heat flux, thus further destabilizing the layer (Stevens 1996). This effect might be particularly significant for very small surface fluxes. However, in our case of relatively large moisture flux, increase in moisture amount in the surface layer by about 5% would not dramatically reduce the surface flux. Increase in the heat flux would make the convection even more vigorous, and, therefore, may amplify its effect.

Chapter 7.

Conclusions

A new LES dynamical framework coupled with the explicit microphysical module has been developed. One of the important features of the model is a consistent use of the Smolarkiewicz positive definite monotonic finite-difference scheme for calculation of the dynamical tendencies for both thermodynamical and microphysical variables. The new dynamical framework was tested against analytical solution for the case of the linear mountain waves. In addition, the new model results were in accord with predictions from the other LES models during a series of the LES model intercomparison workshops as a part of the Global Energy and Water Cycle Experiment Cloud System Study (GCSS) Program.

In addition to the tests designed to assess the accuracy of the new LES dynamical framework, I have tested the explicit microphysical module. The results convincingly show that the simulations are almost insensitive to the doubling of the drop size spectrum resolution in our model, implying that the employed drop size resolution is adequate for accurate prediction of cloud microphysics parameters. I also demonstrated that the results are very sensitive to the drop spectrum remapping technique used in semi-Lagrangian condensation calculations. The test of the drop coagulation procedure revealed that the method becomes inaccurate when the mass of the drizzle is dominated by the drops larger than about 250 μm. However, it was demonstrated that this limitation is rarely exceeded in typical simulations of the STBL even in the heavy drizzle cases.

In order to evaluate the realism of the model, I carried out a direct comparison of the model predictions with the aircraft observations of the STBL. The first case is

based on the UKMRF flight 526 measurements collected over the North Sea on 22 July 1982; the second case corresponds to the ASTEX flight A209 flown on 12-13 June 1992. The model was able to reproduce reasonably well most of the observed characteristics such as turbulent fluxes and variances of various fields, intensity and vertical distribution of the turbulent kinetic energy, upward and downward radiation fluxes, and the cloud drop spectra.

A new bulk microphysical parameterization was designed using the explicit model as a benchmark for comparison. The liquid water is divided into two categories - non-precipitable cloud water and drizzle, similar to traditional Kessler-type parameterizations. The model predicts the water content and drop concentration for each category. The source/sink terms such as autoconversion of cloud water into drizzle are deduced directly from the drop size spectra predicted by the explicit microphysical model.

The predictions of the LES model using the new bulk microphysics were compared with the predictions using the explicit microphysics for two cases: non-drizzling and heavy-drizzling STBL. The results show that the new bulk microphysical model satisfactory reproduces many characteristics of the STBL as simulated by the explicit microphysical model. It should be noted that the proposed new bulk microphysical parameterization was designed to be applied to the marine stratocumulus cloud layers, although the method may be seen as a more general approach to developing bulk parameterizations for the other types of clouds.

A case of the stratocumulus-to-cumulus transition triggered by the depletion of the CCN was simulated. It was shown that the response of the STBL to the increasing drizzle due to the CCN depletion is by reducing its fractional cloud cover and changing the character of the circulation toward the cumulus convection. The boundary layer after the Sc-to-Cu transition consists of two layers: the well-mixed cloud free surface layer driven by surface heat fluxes and shear, and the conditionally unstable upper layer

capped by the inversion with the embedded cumulus clouds connected to their moisture and CCN supply in the surface layer.

References

Ackerman, A. S., O. B. Toon, and P.V. Hobbs, 1993: Dissipation of Marine Stratiform Clouds and Collaps of the marine bounadry layer due to the depletion of cloud condensation nuclei by clouds.

Ackerman, A. S., O. B. Toon, and P.V. Hobbs, 1995: A model for particle microphysics, turbulent mixing, and radiative transfer in the stratocumulus-topped marine boundary layer and comparison with measurements. *J. Atmos. Sci.*, 52, 1204-1236.

Albrecht, B. A., D. A. Randall, and S. Nicholls, 1988: Observations of marine stratocumulus during FIRE. *Bull. Amer. Meteor. Soc.*, **69**, 618-626.

Albrecht, B. A., 1989: Aerosol, cloud microphysics, and fractional cloudiness. *Science*, **245**, 1227-1230.

Albrecht, B. A., 1993: effects of precipitation on the thermodynamic structure of the trade wind boundary layer. *J. Geophys. Res.*, **98**, 7327-7337.

Albrecht, B. A., C. S. Bretherton, D. Jonhson, W. H. Schubert, and A. S. Frisch, 1995: The Atlantic Stratocumulus Experiment - ASTEX. *Bull. Amer. Meteor. Soc.*, **76**, 889-904.

Arnasson, G., and. R. S. Greenfield, 1972: MIcro- and macro-stractures of numerically simulated convective clouds. *J. Atmos. Sci.*, **29**, 342-367.

Austin, P. H., Y. Wang, R. Pincus, and V. Kujala, 1995: Precipitation in stratocumulus clouds: observational and modeling results. *J. Atmos. Sci.*, **52**, 2329-2352.

Baker, M. B., 1993: Variability in concentrations of cloud condensation nuclei in the marine cloud-topped boundary layer. *Tellus*, **45B**, 458-472.

Baker, M. B., and R. J. Charson, 1989: Bistability of CCN concentrations and thermodynamics in the cloud-topped boundary layer. *Nature*, **345**, 142-144.

Beard, K. V., and R.L. Ochs, 1993: Warm rain initiation: An overview of microphysical mechanizms. *J. Appl. Meteor.*, **32**, 608-625.

Berry, E. X., 1968: Modification of the warm rain process. *Proc. First National Conf. on Wea. Modif.*, Albany, NY, April 28 - May 1, 1968, AMS, Boston, MS, 81-88.

Berry, E, X., and R. L. Reinhardt, 1974a: An analysis of cloud drop growth by collection: Part II. Single initial distributions. *J. Atmos. Sci.*, **31**, 1825-1831.

Berry, E, X., and R. L. Reinhardt, 1974b: An analysis of cloud drop growth by collection: Part III. Accretion and self-collection. *J. Atmos. Sci.*, **31**, 2118-2126.

Bretherton, C. S., 1992: A conceptual model of the stratocumulus-trade-cumulus transition in the subtropical oceans. *Proc., 11th Int. Conf. on Clouds and Precipitation*, Vol. 1, Monreal, Quebec, Canada, 374-377.

Bretherton, C. S., and R. Pincus, 1995: Cloudiness and marine boundary layer dynamics in the ASTEX Lagrangian experiments. Part I: Synoptic setting and vertical structure. *J. Atmos. Sci.*, **52**, 2707-2723.

Bretherton,C. S., M. K. MacVean, P. Bechtold, A. Chlond, W. R. Cotton, J. Cuxart, H. Cuijpers, M. Khairoutdinov, B. Kosovic, D. Lewellen, Chin-Hoh Moeng, P. Siebesma, B. Stevens, D. E. Stevens, I. Sykes, and M. C. Wyant, 1998: An intercomparison of radiatively-driven entrainment and turbulence in a smoke cloud, as simulated by different numerical models. *Quart. J. R. Meteor. Soc.* , in press.

Brost, R. A.,D. H. Lenschow, and J. C. Wyngaard, 1982: Marine stratocumulus layers. Part I: Mean conditions. *J. Atmos. Sci.*, **39**, 800-817.

Businger, J. A., J. C. Wyngaard, Y. Izumi, and E. F. Bradley, 1971: Flux-profile relationship in the atmospheric surface layer. *J. Atmos. Sci*, 28, 181-189.

Charlson, R. J., J. E. Lovelock, M. O. Andreae, and S. G. Warren, 1987: Ocean phytoplankton, atmospheric sulfer, cloud albedo and climate. *Nature*, **326**, 655-661.

Charnock, H., 1955: Wind stress on a water surface. *Q. J. R. Meteor. Soc.*, 81, 639-640.

Chen, C., and W. R. Cotton, 1987: The physics of the marine stratocumulus-capped mixed layer. *J. Atmos. Sci.*, **44**, 2951-2977.

Clark, T. L., 1973: Numerical modeling of the dynamics and microphysics of warm cumulus convection. *J. Atmos. Sci.*, **30**, 857-878.

Clark, T. L., 1974a: A study of cloud phase parameterization using the gamma distribution. *J. Atmos. Sci.*, **31**, 142-155.

Clark, T. L., 1974b: On modeling nucleation and condensation theory in Eulerian spatial domain. *J. Atmos. Sci.*, **31**, 2099-2117.

Clark, T. L., 1976: Use of log-normal distributions for numerical calculations of condensation and collection. *J. Atmos. Sci.*, **33**, 810-821.

Clark, T. L., and W. D. Hall, 1983: A cloud physical parameterization method using movable basic functions: Stochastic coalescence parcel calculations. *J. Atmos. Sci.*, **40**, 1709-1728.

Cotton, W. R., 1972: Numerical simulation of precipitation development in supercooled cumuli - Part I. *Mon. Wea. Rev.*, **100**, 757-763.

Cotton, W. R., and R. A. Anthes, 1989: Storm and Cloud Dynamics. Academic press Inc, Dan Diego, 883 pp.

Curry, J. A., 1986: Interaction among turbulence, radiation and microphysics in arctic stratus clouds. *J. Atmos. Sci.*, **43**, 90-106.

Deardorff, J. W., 1980: Stratocumulus-capped mixed layers derived from a three-dimensional model. *Bound. Layer Meteorol.*, **18**, 495-527.

Duchan, C.E., 1979: Lanczos filtering in one and two dimensions. *J. Appl. Meteor.*, **18**, 1016-1022.

Durran, D. R., and J. B. Klemp, 1983: A compressible model for the simulation of moist mountain waves. *Mon. Wea. Rev.*, **111**, 2341-2361.

Duynkerke, P. G., H. Zhang, and P. J. Jonker, 1995: Microphysics and turbulent structure of nocturnal stratocumulus as observed during ASTEX. *J. Atmos. Sci.*, **52**, 2763-2777.

Feingold, G., B. Stevens, W. R. Cotton, and R. L. Walko, 1994: An explicit cloud microphysical/LES model designed to simulate the Twomey effect. *Atmos. Res.*, **33**, 207-233.

Feingold, G., B. Stevens, W. R. Cotton, and A. S. Frisch, 1996: The relationship between drop residence time and drizzle production in numerically simulated stratocumulus clouds. *J. Atmos. Sci.*, **53**, 1108-1122.

Fiedler, B. H., 1993: Cell broadening in three-dimensional thermal convection between poorly conducting boundaries. *Beitr. Phys. Atmos.*, **66**, 173-181.

Fiedler, B.H., and M. Khairoutdinov, 1994: Cell broadening in three-dimensional thermal convection between poorly conducting boundaries: Large eddy simulations. *Beitr. Phys. Atmos.*, **67**, 235-241.

Fowler, L. D., D. A. Randall, and S. A. Rutledge, 1996: Liquid and the ice cloud microphysics in the CSU general circulation model. Part I: Model description and simulated cloud microphysics processes. *J. Climate*, **9**, 489-529.

Gerber H., 1996: Microphysics of marine stratocumulus clouds with two drizzle modes. *J. Atmos. Sci.*, **53**, 1649-1662.

Hudson, J.G., and S. S. Yum, 1996: Droplet spectral broadening in stratus. *Submitted to J. Atmos. Sci.*

Hall, W. D., 1980: A detailed microphysical model within a two-dimensional dynamical framework: Model description and preliminary results. *J. Atmos. Sci.*, **37**, 2486-2507.

Kazakov A. L., and G. L. Lazriev, 1978: Parameterization of atmospheric surface layer and the active soil layer. *Izvestiya of the Soviet Academy of Science, Atmospheric and Oceanic Physics*, 14, 186-191.

Kessler, E., 1969: *On the distribution and continuity of water substance in atmospheric circulations. Meteor. Monogr.*, 10, No. 32, Amer. Meteor. Soc., 84 pp.

Khairoutdinov M. F., and Y. L. Kogan, 1997: Case study of stratocumulus cloud layer dynamics, microphysics, and radiation in a large-eddy simulation model with explicit microphysics. Submitted to *J. Atmos. Sci.*

Kogan, Y. L., 1991: The simulation of a convective cloud in a 3-D model with explicit microphysics. Part I: Model description and sensitivity experiments. *J. Atmos. Sci.*, 48, 1160-1189.

Kogan, Y. L., D. K. Lilly, Z. N. Kogan, and V. V. Filyushkin, 1994: The effect of CCN regeneration on the evolution of stratocumulus cloud layers. *J. Atmos. Res.*, **33**, 137-150.

Kogan, Y. L., M. P. Khairoutdinov, D. K. Lilly, Z. N. Kogan, and Q. Liu, 1995: Modeling of stratocumulus cloud layers in a large eddy simulation model with explicit microphysics. *J. Atmos. Sci*, 52, 2923-2940.

Kovetz, A., and B. Olund, 1969: The effect of coallescence and condensation on rain formation in a cloud of finite vertical extent. *J. Atmos. Sci.*, **26**, 1060-1065.

Krueger, S. K., G. T. McLean, and Q. Fu, 1995: Numerical simulation of the stratus-to-cumulus Transition in the subtropical marine boundary layer. Part I: Boundary layer structure. *J. Atmos. Sci.*, **52**, 2839-2850.

Lenschow, D. H., and B. B. Stankov, 1986: Length scales in the convective boundary layer. *J. Atmos. Sci.*, **43**, 1198-1209.

Levin, L. M., and Sedunov, Y. S., 1966: *J. de.Rech.Atmos*. 2, 424

Lilly, D. K., 1967: The representation of small-scale turbulence in numerical simulation experiments. Proc. IBM Scientific Computing Symposium on Environmental Sciences, H. H. Goldstine Editor, IBM Form No. 320-1951, 195-210.

Lilly, D. K., 1968: MOdels of cloud-topped mixed layers under a strong inversion. *Quart. J. Roy. Meteor. Soc.*, **94**, 294-309.

Liou, K.-N., and S.-C. Ou, 1989: The role of cloud microphysics processes in climate: an assessment from a one-dimensional perspective. *J. Geophys. Res.*, **94**, D6, 8599-8607.

Liu, Q.-F., Y. L. Kogan, D. K. Lilly, and M. P. Khairoutdinov, 1997: Variational optimization method for calculation of cloud drop growth in an Eulerian drop-size framework *J. Atmos. Sci.*, **54**, 2493-2504.

Mann, J., and D. H. Lenschow, 1994: Errors in airborne flux measurements. *J. Geophys. Res.*, **99**(D7), 14519-14526.

Manton, M. J., and W. R. Cotton, 1977: Formulation of approximate ecuations for modeling moist deep convection on the mesoscale. Atmos. Sci. Paper No. 266, Dept. Of Atmos. Sci., Colorado State University.

Marshall, J. S., and W. McK. Palmer, 1948: The distribution of rain drops with size. *J. Meteor.*, **5**, 165.

Martin, G. M., D. W. Johnson, and A. Spice, 1994: The measurement and parameterization of effective radius of droples in warm stratocumulus clouds. *J. Atmos. Sci*, 51, 1823-1842.

Mason, B. J., 1952: Production of rain and drizzle by coalescence in stratiform clouds. Quart. J. Roy. Meteor. Soc., 78, 377-386.

Mason, P., 1994: Large eddy simulations: A critical review of the technique. *Q. J. R. Meteor. Soc.*,**120**, 1-26

Moeng, C.-H., 1984: A large-eddy simulation model for the study of planetary boundary layer turbulence., *J. Atmos. Sci.* , 41, 2052-2062.

Moeng, C.-H. and D. A. Randall, 1984: Problems in simulating the stratocumulus-topped boundary layer with a third-order closure model. *J. Atmos. Sci.* , 41, 1588-1600.

Moeng, C.-H., 1986: Large-eddy simulation of a stratus-topped boundary layer. Part I: Structure and budgets. *J. Atmos. Sci.* , 43, 2886-2900.

Moeng, C.-H., D. H. Lenschow, and D. A. Randall, 1995: Numerical investigations of the roles of radiative and evaporative feedbacks in stratocumulus entrainment and breakup. J. Atmos. Sci., 52, 2869-2883

Moeng, C.-H., W. R. Cotton, C. Bretherton, A. Chlond, M. Khairoutdinov, S. Krueger, W. S. Lewellen, M. K. MacVean, J. R. M. Pasquier, H. A. Rand, A. P. Siebesma, B. Stevens, and R. I. Sykes, 1996: Simulation of a stratocumulus-topped planetary layer: intercomparison among different numerical codes. *Bull. Amer. Meteor. Soc.*, 77, 261-278.

Montoya G., G. J., A. J. C. Sampaio, and F. C. Almeida, 1995: An analysis of the effect of decreasing the size resolution in two techniques to solve the stochastic collection equation for growing cloud drops. *Atmos. Res.*, 35, 173-188.

Nicholls, S., 1984: The dynamics of stratocumulus: Aircraft observations and comparisons with a mixed layer model. *Quart. J. Roy. Meteor. Soc.*, **110**, 783-820.

Nicholls, S., and J. Leighton, 1986: An observational study of the structure of stratiform cloud sheets: Part I. Structure. *Quart. J. Roy. Meteor. Soc.*, **112**, 431-460.

Nicholls, S., 1987: A model of drizzle growth in warm turbulent clouds. *Q. J. R. Meteor. Soc.*, 113, 1141-1170.

Nieuwstadt, F. T. M., P. J. Mason, C.-H. Moeng, and U. Schumann, 1991: Large-eddy simulation of the convective boundary layer. A comparison of four computer codes. *Turbulent Shear Flows* 8, 343-367.

Ochs, H. T., III, 1978: Moment-conserving techniques for warm-cloud microphysics computations. Part II: Model testing and results. *J. Atmos. Sci.*, **35**, 1959-1973.

Paluch, I. R., and D. H. Lenschow, 1991: Stratiform cloud formation in the marine boundary layer. *J. Atmos. Sci.*, **48**, 2141-2158.

Pincus, R., and M. B. Baker, 1994: Effect of precipitation on the albedo susceptibility of clouds in the marine boundary layer. *Nature*, **372**, 250-252.

Pruppacher, H. R., and J. D. Klett, 1997: Microphysics of clouds and precipitation. 2nd rev. and enl. ed. *Kluwer Academic Publishers*.

Ramanathan, V., R. D. Cess, E. F. Harrison, P. Minnis, B. R. Barkstorm, E. Ahmad, D. Hartman, 1989: Cloud-radiative forcing and climate: Results from the earth radiation budget experiment. *Science*, 243, 57-63.

Radke, L. F., J. H. Lyons, P. V. Hobbs, and J. E. Coakley, 1988: In situ measurements of "ship tracks" . *Preprints for 10-th Intern. Cloud Phisics Conf.*, Bad Homburg, FRG, August 15-20, 1988. pp. 121-123, (vol. 1).

Randall, D. A., 1980: Conditional instability of the first kind upside-down. *J. Atmos. Sci.*, **37**, 125-130.

Randall, D. A., J. A. Coakley, Jr., C. W. Fairall, R. A. Kropfli, and D. H. Lenschow, 1984: Outlook for research on subtropical marine stratiform clouds. *Bull. Amer. Meteor. Soc.*, **65**, 1290-1301.

Roach, W. T., 1976: On the effect of radiative exchange on the growth by condensation of a cloud or fog droplet. *Q. J. R. Meteor. Soc.*, 102, 361-372.

Roach, W. T., and A. Slingo, 1979: A high resolution infrared radiative transfer scheme to study the interaction of radiation with cloud. *Q. J. R. Meteor. Soc.*, 105, 603-614.

Rothermel, J., and E. M. Agee, 1980: Aircraft investigation of mesoscale cellular convection during AMTEX 75. *J. Atmos. Sci.*, **37**, 1027-1049.

Slingo, A., 1989: AGCM parameterization for the shortwave radiative properties of water clouds. *J. Atmos.Sci.*, **46**, 1419-1427.

Soong, S., 1974: Numerical simulation of warm rain development in an axisymmetric cloud model. *J. Atmos. Sci.*, **31**, 1262-1285.

Squires, P., 1958: The microstructure and colloidal stability of warm clouds. *Tellus*, **10**, 256-271.

Stepanov, A. S., 1976: Influence of turbulence on the size spectrum of cloud drops during condensation. *Izv. Acad. Sci. USSR, Atmos. Oceanic Phys.*, **12**, 281-292.

Stevens, B., 1996: On the dynamics of precipitating stratocumulus. Atmospheric Science Department Paper, No. 618, Colorado State University, Ft. Collins, CO, USA, pp.140.

Smolarkiewicz, P. K., and W.W. Grabowski, 1990: The multi-dimensional positive definite advection transport algorithm: Nonoscillatory option. *J. Comput. Phys.*, 86, 355-375.

Tremback, C. J., J. Powell, W. R. Cotton, and R. A. Pielke, 1987: The forward-in-time upstream advection scheme: Extension to heigher orders. *Mon. Wea. Rev.*, 115, 540-555.

Tripoli, G. J., and W. R. Cotton, 1980: A numerical investigation of several factors contributing to the observed variable intensity of deep convection over South Florida. *J. Appl. Meteor.*, **19**, 1037-1063.

Turton, J., and Nicholls, S, 1987: A study of the diurnal variation of stratocumulus using a multiple mixed-layer model. *Q. J. R. Meteor. Soc.*, 113, 969-1011.

Twomey, S., 1977: The influence of pollution on the short wave albedo of clouds. *J. Atmos. Sci.*, **34**, 1149-1152.

Wang, S., and B. A. Albrecht, 1992: Convective mixing in stratocumulus-topped boundary layers observed during FIRE. Preprints, *11th Int. Conf. on Clouds and Precipitation*, Monreal, ICCP and IAMAP.

Wyant, M. C., H. A. Rand, and D. E. Stevens, 1996: Numerical simulation and conceptual model of the stratocumulus to trade cumulus transition. *J. Atmos. Sci.*, **54**, *168-192.*